

DECAYS OF THE $\Upsilon(1S)$ INTO A PHOTON AND TWO CHARGED HADRONS

By

LUIS BREVA-NEWELL

A DISSERTATION PRESENTED TO THE GRADUATE SCHOOL
OF THE UNIVERSITY OF FLORIDA IN PARTIAL FULFILLMENT
OF THE REQUIREMENTS FOR THE DEGREE OF
DOCTOR OF PHILOSOPHY

UNIVERSITY OF FLORIDA

2004

To my Parents

ACKNOWLEDGMENTS

I owe my gratitude to many people without whom this work would not have been possible. First of all, I would like to thank my supervisor, Dr. Yelton. His office door was always open for me, and he spent long hours of his time listening to my ideas even though only a few of them ever worked. He gave me freedom to explore and branch off in different directions while steadily guiding me forward at the same time. After these years of working together I consider him more than a mentor, and I think of him as a close friend.

Many people from CLEO have put their own time and work into this analysis. I am grateful to all my committee members Tomas Ferguson, John Cummings, Thomas Coan, and especially Rich Galik for all their help and efforts to improve this work.

During my stay at the University of Florida I have met many people inside and outside the physics world. I would like to thank my first year graduate teachers Dr. Sikivie and Dr. Woodard who were a source of inspiration for me. My thanks also go to my fellow graduate students Vijay Potlia, Rukshana Patel, Necula Valentin, Jennifer Sippel, Suzette Atienza, G. Suhas, and many more for all our fun physics discussions and late homework sessions. I would also like to thank the good friends I made outside the physics building, James Power, Yaseen Afzal (Paki), Ramji Kamakoti (Ramjizzle), Dan DeKee (Double Down), and Fernando Zamit (Fernizzle) who always reminded me that there is more to life than Physics.

The most important person I have met during my graduate career is my wife, Jennifer. I thank her for enduring all those endless days when I would answer her

questions with only grunts and nods while my attention remained fixed on the computer screen. Her love and support are invaluable to me.

Finally, I would like to thank my parents Manuel and Charlene, my sister Teresa, and my brother Gaizka. They have always been there for me.

TABLE OF CONTENTS

	<u>page</u>
ACKNOWLEDGMENTS	iii
ABSTRACT	vii
CHAPTER	
1 THEORY	1
1.1 Particle Physics	1
1.1.1 The Standard Model	1
1.1.2 Quantum Chromodynamics	3
1.1.3 Introduction to the Radiative Decays of the $\Upsilon(1S)$	6
1.2 Radiative Decays of Quarkonia Overview	14
2 EXPERIMENTAL APPARATUS	17
2.1 The Cornell Electron Storage Ring	17
2.2 The CLEO III Detector	20
2.2.1 Superconducting Coil	21
2.2.2 Tracking System	21
2.2.3 Ring Imaging Cherenkov Detector	24
2.2.4 Crystal Calorimeter	26
2.2.5 Muon Detectors	28
3 ANALYSIS OF THE DATA	31
3.1 Data Sample	31
3.1.1 Continuum Subtracted Distributions	32
3.2 Event Selection	34
3.2.1 Skim Cuts	35
3.2.2 Analysis Cuts	37
3.2.3 Cut Summary, Efficiencies, and Fake Rates	43
4 EXCLUSIVE RADIATIVE DECAY $\Upsilon(1S) \rightarrow \gamma\pi^+\pi^-$	49
4.1 Robustness of The Mass Distribution	49
4.2 Statistical Fit of the Invariant Mass Distribution	50
4.3 Angular Distribution of The Signal	51
4.3.1 Optimum Mass Interval	52
4.3.2 Background Subtraction	56
4.3.3 Statistical Fit of the Helicity Angular Distributions	57

5	EXCLUSIVE RADIATIVE DECAY $\Upsilon(1S) \rightarrow \gamma K^+ K^-$	68
5.1	Statistical Fit of the Invariant Mass Distribution	68
5.2	Angular Distribution of The Signal	71
6	EXCLUSIVE RADIATIVE DECAY $\Upsilon(1S) \rightarrow \gamma p \bar{p}$	85
7	SYSTEMATIC UNCERTAINTIES	91
7.1	Cuts	91
7.1.1	Justification of the DPTHMU Cut	92
7.2	Angular Distribution of Signal	93
7.3	Different Hadronic Fake Rates Between 1S and 4S	102
7.4	Other Systematic Sources	102
7.5	Overall Systematic Uncertainties	104
8	RESULTS AND CONCLUSION	105
	APPENDIX HELICITY FORMALISM FOR TWO BODY DECAYS	108
	REFERENCES	123
	BIOGRAPHICAL SKETCH	125

Abstract of Dissertation Presented to the Graduate School
of the University of Florida in Partial Fulfillment of the
Requirements for the Degree of Doctor of Philosophy

DECAYS OF THE $\Upsilon(1S)$ INTO A PHOTON AND TWO CHARGED HADRONS

By

Luis Breva-Newell

December 2004

Chair: John Yelton

Major Department: Physics

Using the CLEO III detector we report on a new study of exclusive radiative $\Upsilon(1S)$ decays into the final states $\gamma\pi^+\pi^-$, γK^+K^- and $\gamma p\bar{p}$. We present branching ratios for the decay modes $\Upsilon(1S) \rightarrow \gamma f_2(1270)$, $\Upsilon(1S) \rightarrow \gamma f_2'(1525)$, $\Upsilon(1S) \rightarrow \gamma f_0(1710)$ with $f_0(1710) \rightarrow K^+K^-$ and $\Upsilon(1S) \rightarrow \gamma f_4(2050)$.

CHAPTER 1 THEORY

1.1 Particle Physics

Particle physics is the branch of physics dedicated to the study of matter and energy at the most fundamental level. This means that the job of a particle physicist is to identify the smallest constituents of matter and describe how they interact with each other.

Humankind has been interested in this subject since ancient times. Two of the first particle physicists in recorded history are the Greek thinkers Empedocles and Democritus from the fifth century BC. Empedocles stated that our complex world was made from combining four fundamental elements (earth, air, fire and water) in different proportions. Democritus on the other hand, believed that the apparently continuous objects in the natural world were not really continuous, but made from voids and indivisible particles called atoms.

Over the last half century Particle physics has advanced tremendously and we now have a beautiful, but incomplete, theory firmly grounded on experiment that describes the fundamental constituents of matter and how they interact with each other. This theory is called “The Standard Model.”

1.1.1 The Standard Model

According to the Standard Model, the fundamental building blocks of matter are point like particles which interact with each other in as many as three different ways. Each type of interaction, or force, is itself carried by point like particles

called force carriers. The particles which are force carriers are bosons ¹ and are collectively called gauge bosons because they are needed for the theory to be gauge invariant. The non-force carrying particles are fermions. ²

The three interactions described by the Standard Model are called the electromagnetic force, the weak force, and the strong force. The force of gravity is not included in the Standard Model, and this is one of the reasons the Standard Model is not yet complete. The electromagnetic force carriers are photons, the weak force carriers are the Z^0 , W^+ , and W^- particles, and finally, the strong force is carried by eight kinds of gluons. Table 1–1 summarizes the situation.

Table 1–1: Gauge bosons and the force they carry.

Symbol	Name	Force Carried
γ	Photon	Electromagnetic
Z^0	Z^0	Weak
W^+	W^+	Weak
W^-	W^-	Weak
g	gluon	Strong

Particles which interact through a particular force are said to couple to it and to carry an associated charge. The nomenclature is as follows, particles that interact through the electromagnetic force have an electromagnetic charge called electric charge, those which interact through the weak force have a weak charge called weak isospin, and those which interact strongly have a strong charge called color.

The rest of the particles in the Standard Model which are not force carriers, the fermions, are subdivided into different groups depending on their properties (See table 1–2) , reminiscent of the way chemists organized the elements into

¹ Bosons are defined as particles with integer spin in quantum mechanics.

² Fermions are defined as particles with half odd fractional spin.

the periodic table during the second half of the nineteenth century. Fermions are divided into quarks (generically represented by the symbol q) and leptons. The main difference between these two groups is that quarks interact through the strong force while leptons do not. There are six types of leptons and six types of quarks (also called the six quark flavors) which are grouped into three generations. Each generation consist of two quarks and two leptons. All three generations replicate the same set of force charges, the main difference between generations is the mass of the particles (for example, the ratio of the masses of $e : \mu : \tau$ is $1 : 200 : 3500$). For each fermion there is an anti-fermion with equal mass and spin and opposite charge.

Table 1–2: Fermion symbols classified into quarks, leptons, and the three generations along with the generational common charges.

	First Generation	Second Generation	Third Generation	Electric Charge	Weak Charge	Has Color
Quarks	u	c	t	$+2/3$	$+1/2$	Yes
	d	s	b	$-1/3$	$-1/2$	Yes
Leptons	ν_e	ν_μ	ν_τ	0	$+1/2$	No
	e	μ	τ	-1	$-1/2$	No

1.1.2 Quantum Chromodynamics

Quantum chromodynamics (QCD) is the part of the Standard Model that describes the strong force. QCD is based on local gauge invariance and color symmetry. There are three possible color charges for quarks called r (red), b (blue), and g (green). Anti-quarks have opposite colors called \bar{r} , \bar{b} , \bar{g} . The strong force between quarks only depends on their colors and is independent of their flavor.

A very important characteristic of the strong force is that gluons themselves carry a color charge and an anti-color charge so they can interact with other quarks through the strong force and change their color. Since there are three colors and three anti-colors one might think that there are nine different gluons. However, there is one linear combination of color anti-color states that has no net color and

leaves a quark unchanged. There are therefore $9 - 1 = 8$ gluons. The 8 individual gluon color states can be written as follows,

$$\begin{aligned}
|1\rangle &= \frac{1}{\sqrt{2}}(r\bar{b} + b\bar{r}) \\
|2\rangle &= \frac{-i}{\sqrt{2}}(r\bar{b} - b\bar{r}) \\
|3\rangle &= \frac{1}{\sqrt{2}}(r\bar{r} - b\bar{b}) \\
|4\rangle &= \frac{1}{\sqrt{2}}(r\bar{g} + g\bar{r}) \\
|5\rangle &= \frac{-i}{\sqrt{2}}(r\bar{g} - g\bar{r}) \\
|6\rangle &= \frac{1}{\sqrt{2}}(b\bar{g} + g\bar{b}) \\
|7\rangle &= \frac{-i}{\sqrt{2}}(b\bar{g} - g\bar{b}) \\
|8\rangle &= \frac{1}{\sqrt{6}}(r\bar{r} + g\bar{g} - 2b\bar{b})
\end{aligned} \tag{1.1}$$

and represent the eight different gluons that exist in nature. The single and unique color state left out is called a color singlet,

$$|9\rangle = \frac{1}{\sqrt{3}}(r\bar{r} + b\bar{b} + g\bar{g}) \tag{1.2}$$

which is invariant under a redefinition of the color (a rotation in color space). In group theory this decomposition of the color states into an octet and a singlet is denoted by $3 \otimes \bar{3} = 8 \oplus 1$. It is worth noting here that a colorless state, such as $|3\rangle$ or $|8\rangle$, is not necessarily a color singlet state.

This situation is analogous to the perhaps more familiar example of two spin $1/2$ particles. Each particle can have their spin up (\uparrow) or down (\downarrow) along the z axis corresponding to four possible combinations represented by each giving a total spin

$S = 0$ or 1 represented by $|S S_z\rangle$. The $S = 1$ states form a triplet,

$$\begin{aligned} |1 +1\rangle &= |\uparrow\uparrow\rangle \\ |1 0\rangle &= \frac{1}{\sqrt{2}}(|\uparrow\downarrow\rangle + |\downarrow\uparrow\rangle) \\ |1 -1\rangle &= |\downarrow\downarrow\rangle \end{aligned} \tag{1.3}$$

and there is a singlet state with $S = 0$,

$$|0 0\rangle = \frac{1}{\sqrt{2}}(|\uparrow\downarrow\rangle - |\downarrow\uparrow\rangle). \tag{1.4}$$

Since gluons themselves carry color they can interact with each other through the strong force. This interaction among the force carriers is unique to the strong force and, when included in perturbative QCD calculations, leads to two important properties observed in nature called “asymptotic freedom” and “color confinement.” Asymptotic freedom means that the interaction gets weaker at short distances. Color confinement is the requirement that observed states have neutral color, or in other words, they must be in a color singlet state.

Confinement explains why free quarks or free gluons, which have a net color charge, have never been observed. It also explains why no fractional charged particles made from a qq bound state have never been observed since it is not possible to construct a color singlet for such a state (in group theory terms $3 \otimes 3 = 6 \oplus 3$ where we have a sextet and a triplet, but no singlet). On the other hand, color singlets can be constructed for a $q\bar{q}$ or qqq system. The color singlet for $q\bar{q}$ is simply the state shown on the right side of Equation 1.2. The color singlet for qqq can be obtained from the decomposition $3 \otimes 3 \otimes 3 = 10 \oplus 8 \oplus 8 \oplus 1$ and is,

$$|qqq\rangle_{color\ singlet} = \frac{1}{\sqrt{6}}(rgb - grb + brg - bgr + gbr - rbg). \tag{1.5}$$

Particles that are bound states of $q\bar{q}$ are abundant in nature and are called mesons, those that are bound states of qqq are called baryons and also abound in

nature. Both groups are collectively called hadrons. There have been hundreds of different hadrons observed, confirming the validity of QCD and the quark flavors. Nevertheless, QCD leaves room for more possibilities. A bound state of two gluons gg (sometimes called a glueball) can be in a color singlet and in principle could be observed.

Although glueballs are allowed by QCD there is no convincing experimental observation of one. Another possibility are bound states that are a mixture of the previous states, such as $\alpha q\bar{q} + \beta gg$ with arbitrary α , β . These states are called “hybrid mesons” or simply “hybrids”. It is believed [1], [2], [3] that hybrids are necessary to explain the spectrum of light mesons between 1-2 GeV.

As with any quantum mechanical theory, the spectrum of bound states is a fundamental test.³ Glueballs are allowed by QCD, yet there is no conclusive experimental evidence of their observation, despite intense experimental searches [4], [5], [6] complemented by lattice QCD calculations [7], [8] and other theoretical contributions like bag models [9], flux-tube models [10], QCD sum rules [11], weakly bound bound-state models [12], and QCD factorization formalism models [13]. Physicists cannot be sure they understand QCD until such states are observed, or until they can explain why we cannot observe them.

1.1.3 Introduction to the Radiative Decays of the $\Upsilon(1S)$

The $\Upsilon(1S)$ is a meson composed of $b\bar{b}$ quarks. Mesons of this kind, composed of a quark and an anti-quark of the same flavor, are in general called quarkonia.

There is a convention behind the name of the $\Upsilon(1S)$. The Υ symbol is reserved for particles composed of $b\bar{b}$ where the combined spin of the quark and anti-quark is 1. The “1S” symbol is borrowed from atomic spectroscopy with the

³ A good example of this is the successful description of the hydrogen atom’s spectrum by quantum mechanics.

“1” meaning that the $b\bar{b}$ pair are in the lowest-energy bound-state, and the “S” meaning that the $b\bar{b}$ have a relative angular momentum $L = 0$. A description of particle naming conventions can be found in [14].

The $\Upsilon(1S)$ is unstable, existing for only about 10^{-24} seconds after which it decays into daughter particles (which in turn decay themselves if they are not stable). The term “radiative decay” is reserved to any $\Upsilon(1S)$ decay where one of the stable daughters is a photon.

The different ways the $\Upsilon(1S)$ can decay must obey the symmetries in nature. Examples of such symmetries are “parity” and “charge conjugation”, both of which will be described soon. Symmetries are very important in the standard model. The usefulness of symmetries can be seen in Noethers’ theorem, which states that for every symmetry there is an associated conserved quantity. Examples of Noethers’ theorem are the conservation of momentum connected to translational invariance and the conservation of angular momentum associated with rotational invariance.

In the next sections we will use the parity and charge conjugation symmetries to find $\Upsilon(1S)$ decays which conserve the associated symmetry constants and are allowed by nature. In particular, we will show that the radiative decay of the $\Upsilon(1S)$ through a photon and two gluons (see Figure 1–1) is allowed. The key observation is that the two gluons must be in a color singlet since both the $\Upsilon(1S)$ and the radiated photon have no color and color must be conserved. This means that the two gluons satisfy color confinement and could form a glueball, although more conventional meson states, or hadrons in no bound state at all, are also possible outcomes. Regardless of what the gluons do, their energy will eventually manifests itself as hadrons. Sometimes, two charged hadrons of opposite charge will emerge. This work examines those two hadrons from a radiative $\Upsilon(1S)$ decay to experimentally probe the gg spectrum.

Parity

The parity operator, \hat{P} , reverses the sign of an object's spatial coordinates. Consider a particle $|a\rangle$ with a wave function $\Psi_a(\vec{x}, t)$. By the definition of the parity operator,

$$\hat{P}\Psi(\vec{x}, t) = P_a\Psi_a(-\vec{x}, t) \quad (1.6)$$

where P_a is a constant phase factor. If we consider an eigenfunction of momentum

$$\Psi_{\vec{p}}(\vec{x}, t) = e^{i(\vec{p}\cdot\vec{x} - Et)} \quad (1.7)$$

then

$$\hat{P}\Psi_{\vec{p}}(\vec{x}, t) = P_a\Psi_{\vec{p}}(-\vec{x}, t) = P_a\Psi_{-\vec{p}}(\vec{x}, t), \quad (1.8)$$

so that any particle at rest, with $\vec{p} = 0$, remains unchanged up to a multiplicative number, P_a , under the parity operator. States with this property are called eigenstates with eigenvalue P_a . P_a is also called the intrinsic parity of particle a , or more usually just the parity of particle a , with the words at rest left implicit. Since two successive parity transformations leave the system unchanged, $P_a^2 = 1$, implying that the possible values for the parity eigenvalue are $P_a = \pm 1$.

In addition to a particle at rest, a particle with definite orbital angular momentum is also an eigenstate of parity. The wave function for such a particle in spherical coordinates is,

$$\Psi_{nlm}(\vec{x}, t) = R_{nl}(r)Y_l^m(\theta, \phi), \quad (1.9)$$

where (r, θ, ϕ) are spherical polar coordinates, $R_{nl}(r)$ is a function of the radial variable r only, and the $Y_l^m(\theta, \phi)$ is a spherical harmonic.

The spherical harmonics are well known functions which have the following property,

$$Y_l^m(\theta, \phi) = (-1)^l Y_l^m(\pi - \theta, \pi + \phi). \quad (1.10)$$

Hence

$$\hat{P}\Psi_{nlm}(\vec{x}, t) = P_a\Psi_{nlm}(-\vec{x}, t) = P_a(-1)^l\Psi_{nlm}(\vec{x}, t) \quad (1.11)$$

proving that a particle with a definite orbital angular momentum l is indeed an eigenstate of the parity operator with eigenvalue $P_a(-1)^l$.

The parities of the fundamental fermions cannot be measured or derived. All that nature requires is that the parity of a fermion be opposite to that of an anti-fermion. As a matter of convention fermions are assigned $P = +1$ and anti-fermions are assigned $P = -1$. In contrast, the parities of the photon and gluon can be derived by applying \hat{P} to the field equations resulting in $P_\gamma = -1$ and $P_g = -1$.

The $\Upsilon(1S)$ has $P = P_b P_{\bar{b}}(-1)^L = -1$ since $L = 0$.

Parity is a good quantum number because it is a symmetry of the strong and electromagnetic force. This means, that in any reaction involving these forces, parity must be conserved.

Charge Conjugation

Charge conjugation is simply the operation which replaces all particles by their anti-particles. In quantum mechanics the charge conjugation operator is represented by \hat{C} . For any particle $|a\rangle$ we can write,

$$\hat{C}|a\rangle = c_a|\bar{a}\rangle \quad (1.12)$$

where c_a is a phase factor. If we let the \hat{C} operator act twice to recover the original state $|a\rangle$,

$$|a\rangle = \hat{C}^2|a\rangle = \hat{C}(c_a|\bar{a}\rangle) = c_a\hat{C}|\bar{a}\rangle = c_a c_{\bar{a}}|a\rangle \quad (1.13)$$

which shows that $c_a c_{\bar{a}} = 1$. If (and only if) a is its own anti-particle, it is an eigenstate of \hat{C} . The possible eigenvalues are limited to $C = c_a = c_{\bar{a}} = \pm 1$.

All systems composed of a the same fermion and an anti-fermion pair are eigenstates of \hat{C} with eigenvalue $C = (-1)^{(L+S)}$. This factor can be understood because of the need to exchange both particles' position and spin to recover the

original state after the charge conjugation operator is applied. Exchanging the particles' position gives a factor of $(-1)^L$ as was shown in the previous section, exchanging the particles spin gives a factor of $(-1)^{S+1}$ as can be verified by inspecting Equations 1.3 and 1.4, and a factor of (-1) which arises in quantum field theory whenever fermions and anti-fermions are interchanged. With this result we can calculate the charge conjugation eigenvalue for the $\Upsilon(1S)$ and obtain $C = -1$ since $L + S = 1$.

The photon is an eigenstate of \hat{C} since it is its own anti-particle. The C eigenvalue for the photon can be derived by inserting \hat{C} into the field equations and is $C_\gamma = -1$.

Finally, we consider a system composed of two gluons that are in a color singlet. The two gluons are bosons and they must have a symmetric wave function, Ψ_G under a $g_1 \leftrightarrow g_2$ exchange. Under this exchange, the orbital angular momentum part of the wave function contributes with a factor $(-1)^L$, the spin part of the wave function for two spin 1 particles contributes with a factor of $(-1)^S$, and the color singlet part of the wave function contributes with a factor of $+1$ since it is symmetric. To ensure that Ψ_G is symmetric we need $L + S$ to be even. This implies that $C = (-1)^{L+S} = +1$. The $L = 0$ and $L = 1$ possible gg bound states are shown in Table 1-3. The $J^{PC} = 1^{-+}$ is peculiar because it is impossible for a $q\bar{q}$ system to have these quantum numbers. If this state is ever observed, it must be a glueball.

Experimental searches for such a state have been done, for example, in [15].

Table 1-3: Possible gg bound states with $L = 0$ or $L = 1$. The possible quantum numbers are limited by the condition that $J = L + S$ be even, which is needed to ensure a symmetric wave function for the two gauge bosons.

L	S	J^{PC}
0	0	0^{++}
0	2	2^{++}
1	1	$0^{-+}, 1^{-+}, 2^{-+}$

Charge conjugation is a symmetry of the strong and electromagnetic force. For those particles that are eigenstates of \hat{C} , C is a good quantum number because in any reaction involving these forces C must be conserved.

The P and C values of various particles used in this analysis are shown in Table 1–4 along with their quark composition, orbital angular momentum, and internal spin.

Table 1–4: Symbol, name, quark composition, angular momentum (L), internal spin (S), parity (P), and charge conjugation eigenvalues (C) for a few of the particles used in this analysis.

Symbol	Name	Quark Composition	L	S	P	C
$\Upsilon(1S)$	Upsilon(1S)	$b\bar{b}$	0	1	-1	-1
π^+	Pion	$u\bar{d}$	0	0	-1	x
π^-	Pion	$d\bar{u}$	0	0	-1	x
K^+	Kaon	$u\bar{s}$	0	0	-1	x
K^-	Kaon	$s\bar{u}$	0	0	-1	x
p	Proton	uud	0	1/2	+1	x
\bar{p}	Anti-proton	$\bar{u}\bar{u}\bar{d}$	0	1/2	-1	x
γ	Photon	x	x	1	-1	-1

Possible Decays of the $\Upsilon(1S)$

At this point we can understand the different possible ways the $\Upsilon(1S)$ can decay. The Possible decays are limited because the strong and electromagnetic force must conserve color, C and P .

The simplest possibility is for the $b\bar{b}$ pair to interact electro-magnetically and annihilate into one virtual photon ⁴. This is allowed by parity, charge conjugation symmetry and color conservation. The decay of the $\Upsilon(1S)$ to one gluon is not allowed by color conservation and is therefore forbidden. $\Upsilon(1S)$ decays to two photons are forbidden by charge conjugation. $\Upsilon(1S)$ decays to two gluons are

⁴ Such a photon is called virtual because it cannot conserve the 4-momentum of $b\bar{b}$ and is unstable, only existing for a brief period of time, as allowed by the uncertainty principle, after which it decays.

also forbidden by charge conjugation. $\Upsilon(1S)$ decays to 3 gluons are allowed (3 gluons can form a color singlet). $\Upsilon(1S)$ decays to 3 photons are also allowed, but are largely suppressed by decays to one photon since 3 successive electromagnetic interactions are much less likely to occur than a single one. Finally, $\Upsilon(1S)$ decays two one photon and two gluons are also allowed under the condition that the two gluons be in a color singlet state.

The three different possible $\Upsilon(1S)$ decays with least amount of interactions (also called lowest order decays) are shown in Figure 1–1.

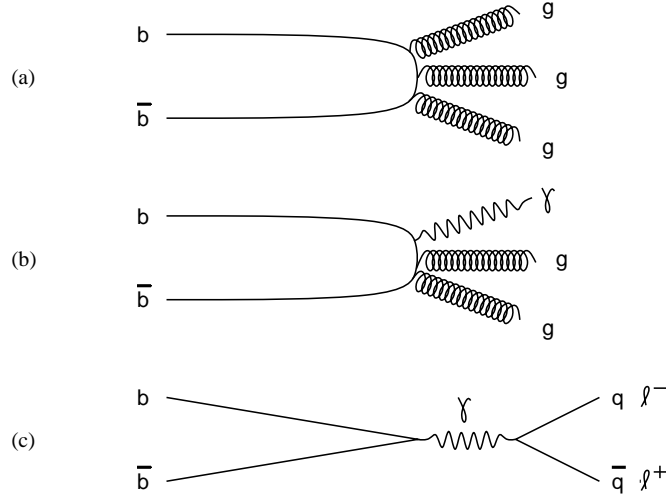


Figure 1–1: Lowest order decays of the $\Upsilon(1S)$ allowed by color conservation, charge conjugation symmetry, and parity. (a) Shows the decay into three gluons, (b) shows a radiative decay, and (c) shows the electromagnetic decay through a virtual photon that in turn decays electromagnetically into a pair of charged fundamental particles, such as quarks or charged leptons (the charged leptons are represented by the symbol l).

Observable Resonances

In this work we search for a resonance X produced in a radiative $\Upsilon(1S)$ decay,

$$\Upsilon(1S) \rightarrow \gamma X. \quad (1.14)$$

Using charge conjugation symmetry on both sides,

$$-1 = -1C_X. \quad (1.15)$$

Therefore, $C_X = +1$.

In order for us to observe X it must decay into two charged hadrons,

$$X \rightarrow h^+ h^-, \quad (1.16)$$

where $h = \pi, K, p$ are the hadrons whose momentum we are going to measure.

Applying charge conjugation to this last decay,

$$+1 = (-1)^{L+S}, \quad (1.17)$$

where L and S are respectively the angular momentum and spin of the $h^+ h^-$ system. This last equation implies that $L + S$ must be even. This has consequences for the possible X parities we can observe. By parity conservation in 1.16,

$$P_X = (-1)^L (-1) (-1) = (-1)^L. \quad (1.18)$$

For $h = \pi, K, S = 0$ and $L = J$ must be even, which implies that $P_X = +1$. For $h = p, S$ can be 0 or 1 and particles with both positive and negative parities can be detected.

Table 1-5: Possible S, L, J, P and C values for X from the radiative decay $\Upsilon(1S) \rightarrow \gamma X$ reconstructed in different decay modes.

Decay Mode	S	L	J	P	C
$X \rightarrow \pi^+ \pi^-$	0	even	even	+1	+1
$X \rightarrow K^+ K^-$	0	even	even	+1	+1
$X \rightarrow p \bar{p}$	0	even	even	+1	+1
$X \rightarrow p \bar{p}$	1	odd	even and odd	-1	+1

1.2 Radiative Decays of Quarkonia Overview

Theoretical models exist for glueball production in quarkonia decay [12] and for the glueball spectrum. For example, a quenched lattice calculation [7] predicts a $J^{PC} = 2^{++}$ glueball ⁵ in the 2.2 GeV/c² mass region (see Figure 1–2). According to Table 1–5, in the charged pion and kaon modes, we are limited to detect glueballs in the leftmost column where $P = C = +1$ of Figure 1–2, while in the proton mode we are restricted to the two left most columns.

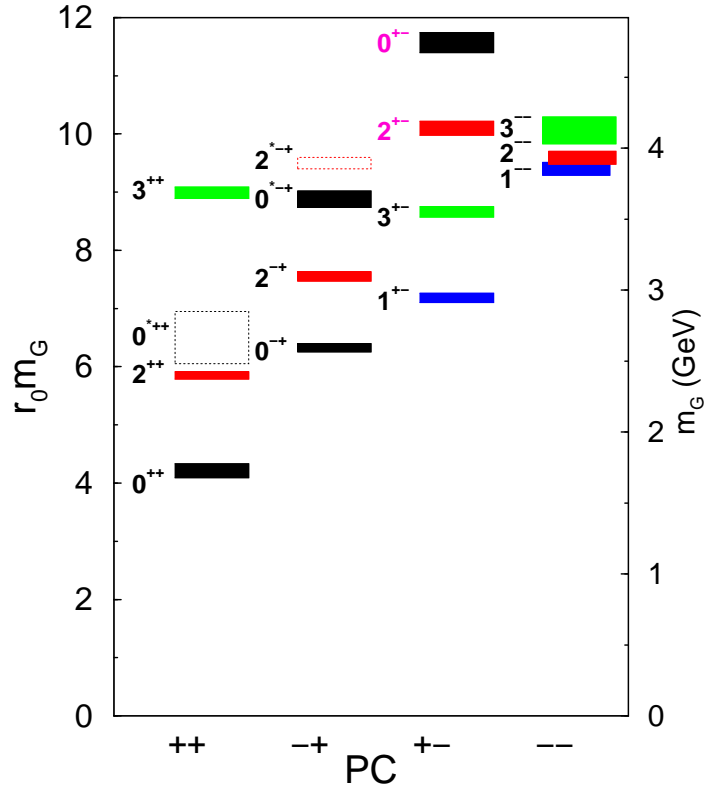


Figure 1–2: Quenched lattice calculation result for the glueball spectrum for different P and C values. The mass scale is shown in terms of a scaling parameter from the QCD lattice calculation named r_0 on the left and in absolute terms on the right by taking $r_0^{-1} = 410$ MeV.

⁵ Here J stands for the internal angular momentum (spin) of the glueball, $J = L + S$.

For some time bound states not considered to be pure glueballs, such as $f_2(1270)$, $f_4(2050)$, η , and η' have been observed in J/ψ radiative decays at the 10^{-3} production level [16] ⁶. In 1996, the BES collaboration claimed the observation of a resonance they called the $f_J(2220)$ particle in the radiative J/ψ system at the 10^{-5} level [17] (see Figure 1–3). A lot of excitement was generated at the time because it is possible to interpret the $f_J(2220)$ as a glueball. However, this result has not been confirmed.

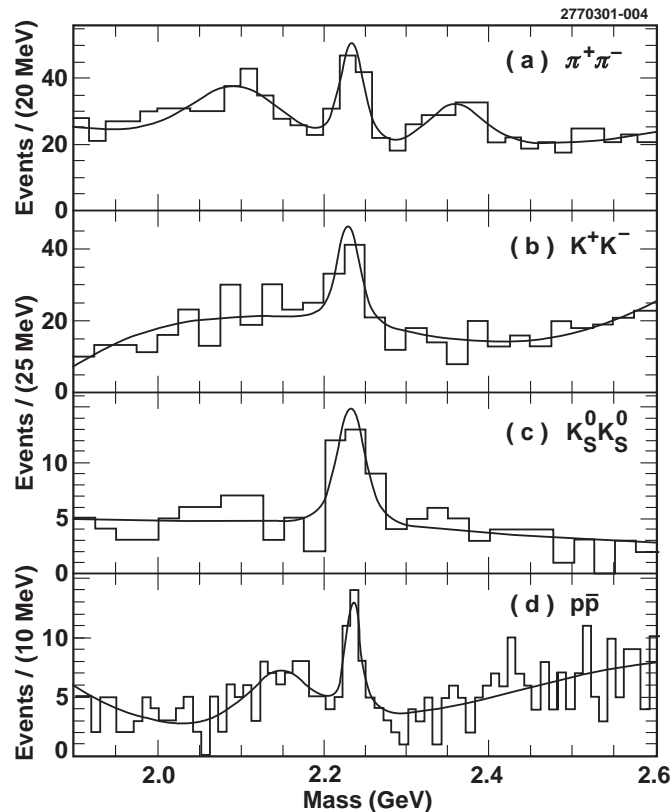


Figure 1–3: The mass spectrum obtained by the BES collaboration in radiative J/ψ decays into different hadronic modes.

Key to identifying a particle as a glueball are (a) suppressed production in two-photon collisions (unlike quarks, gluons don't carry electric charge and do not

⁶ The J/ψ particle is a $c\bar{c}$ bound state. Since the strong force is flavor blind the situation in J/ψ decays is in principle similar to that in $\Upsilon(1S)$ decays.

couple to photons), and (b) flavor symmetric decays, since a pure glueball has no valence quarks.

CLEO has already done several studies of radiative decays of the $\Upsilon(1S)$. Naively, one expects these types of decays to be suppressed by a factor

$$[(q_b/q_c)(m_c/m_b)]^2 \approx 0.025 \tag{1.19}$$

with respect to J/ψ radiative decays. This comes from noticing that the quark-photon coupling is proportional to the electric charge and the quark propagator is approximately $1/m$ for low momentum quarks. In 1999, CLEO made the first observation of a two-body $\Upsilon(1S)$ radiative decay [18]. The spin of the observed resonance could not be measured, but its mass and width were consistent with the $f_2(1270)$ particle. Under this assumption, comparing the measured branching ratio of $\Upsilon(1S) \rightarrow \gamma f_2(2220)$ to the measured branching fraction of the $J/\psi \rightarrow \gamma f_2(1270)$, a suppression factor of 0.06 ± 0.03 was obtained. After the BES result for the $f_J(2220)$ in radiative J/ψ decays, a corresponding search was performed by CLEO in the radiative $\Upsilon(1S)$ system [19]. This analysis put limits on the $f_J(2220)$ production in radiative $\Upsilon(1S)$ decays.

In this work we are privileged to have available the largest collection of radiative $\Upsilon(1S)$ decays in the world. With it, we can study the structure of color singlet gg hadronization, and shed more light on the $f_J(2220)$ result from BES.

CHAPTER 2

EXPERIMENTAL APPARATUS

To carry out our study of the di-hadron spectrum we need to first produce the $\Upsilon(1S)$ resonance and secondly observe its daughter particles flying away at relativistic speeds. These two tasks are respectively accomplished by the Cornell Electron Storage Ring and the CLEO III detector.

2.1 The Cornell Electron Storage Ring

The Cornell Electron Storage Ring (CESR), located at Cornell University, is a circular particle accelerator that produces e^+e^- collisions.

In order to produce such collisions electrons and positrons need to be created, accelerated and stored. CESR's different components, shown in Figure 2-1, have been carrying out this task since 1979.

A typical CESR run begins at the linear accelerator (LINAC) where electrons and positrons are produced. To create positrons, electrons are evaporated off a filament and linearly accelerated by electromagnetic fields towards a tungsten target. The collision creates a spray of electrons, positrons and photons. The electrons are cleared away with magnetic fields and the positrons are introduced into the synchrotron. The filling procedure is identical, except that the tungsten target is removed.

Once the electron and positron beams are introduced into the synchrotron, they are accelerated to the operating energy. In our case they are accelerated to the point where their combined energy is the $\Upsilon(1S)$ mass, 9.46 GeV.

Once the beams are at the desired energy they are transferred to the storage ring, where they will remain for about an hour. At one point in the storage ring the

beams are forced to cross paths. This is the point where e^+e^- collisions occur ¹ and where the center of the CLEO III detector is located. If the accelerator is

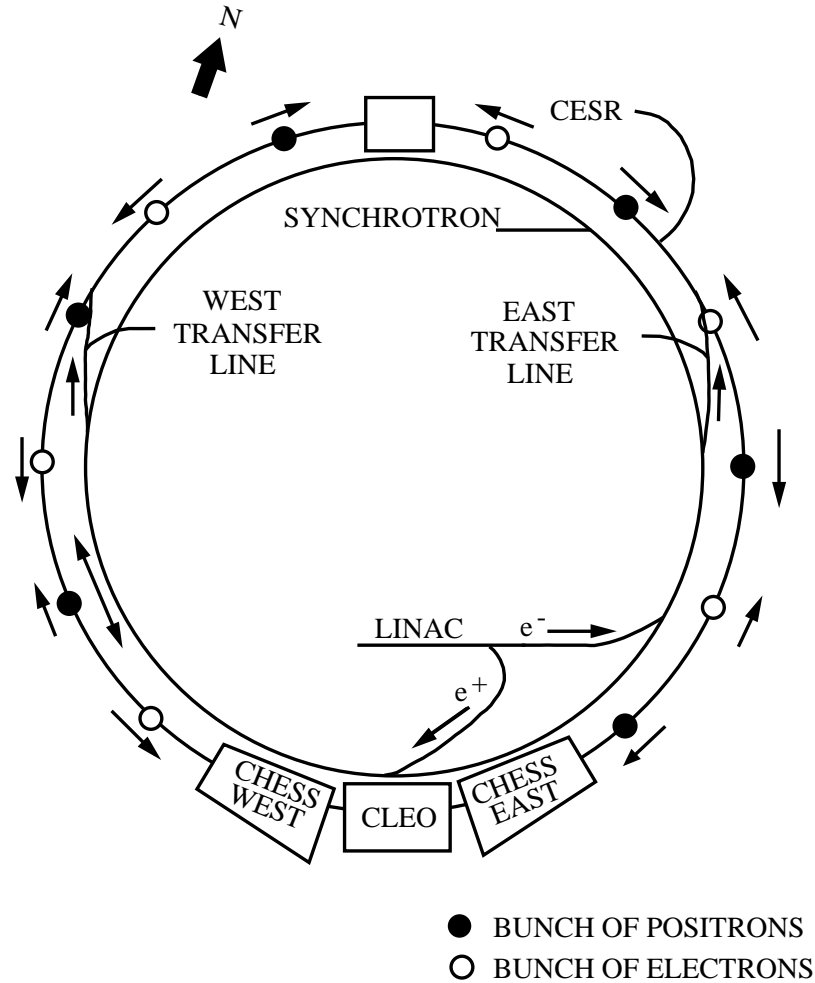


Figure 2-1: The Wilson Laboratory accelerator located about 40 feet beneath Cornell University's Alumni Fields.

performing well a high collision rate results. A high collision rate is crucial for the success of an accelerator and the experiments it serves. The important figure is the number of possible collisions per second per unit area; this is called the luminosity. In order to maximize the luminosity, the beams are focused as small as possible at

¹ This point is not fixed in space, but varies from event to event inside a small volume of space called the interaction region (IR).

the IR. During the CLEO III installation several magnetic quadrupoles were added to CESR to improve the beam focus. CESR has consistently outdone itself while collecting luminosity over the years (see Figure 2–2).

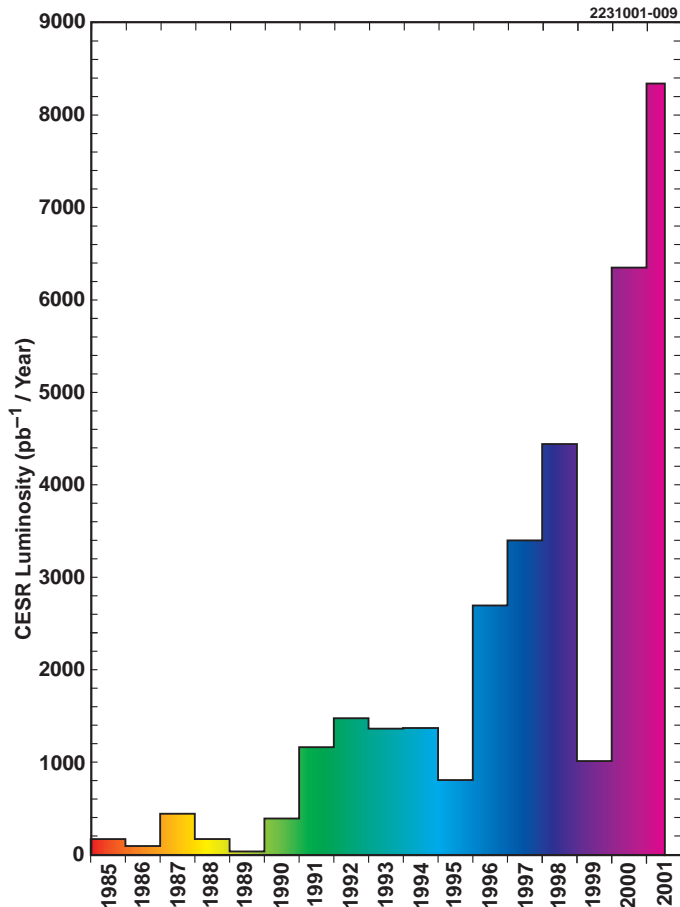


Figure 2–2: CESR yearly luminosity. The gaps in 1995 and 1999 correspond to down times when the CLEO II.V and CLEO III detectors were being installed.

The CLEO III detector measures the time integrated luminosity over a period of time by counting how many times a benchmark process occurs during a certain time interval at the IR. For redundancy, there are two benchmark processes that are used, one where the e^+e^- particles interact to produce a new e^+e^- pair, and the other one where the e^+e^- annihilate and produce two photons. Using the known cross-section for each process, the number of events is converted to a luminosity called the Bhabha integrated luminosity for the first process, and the $\gamma\gamma$

integrated luminosity for the second one. The term “integrated” is sometimes left out and the total luminosity is referred to as simply the Bhabha or $\gamma\gamma$ luminosity, with the time integration left implicit.

2.2 The CLEO III Detector

When the e^+e^- collision occurs, the two particles are annihilated we enter the world of particle physics. Nature decides what to do with the energy from the annihilation. We have no chance of directly observing what is happening at the annihilation point, but eventually long lived semi-stable particles are created that fly off at relativistic speeds. These particles carry information about what happened after the e^+e^- collision, and can tell us what nature did. The CLEO III detector has the important mission of detecting and measuring such particles.

As one can see in Figure 2-3, the CLEO III detector is a composite of many detector elements. These sub-detectors are typically arranged as concentric cylinders. The entire detector is approximately cube shaped, with one side measuring about 6 meters, and weighs over 500 thousand kilograms.

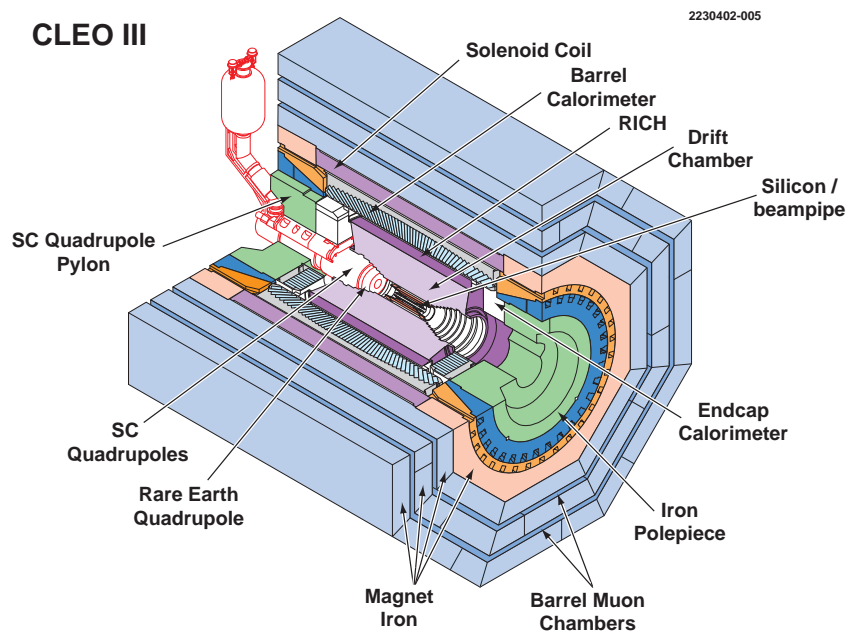


Figure 2-3: The CLEO III detector.

As implied by the name, CLEO III is not the only CLEO detector. CLEO III was preceded by CLEO II.V, CLEO II, CLEO I.V and the original CLEO detectors. The CLEO III detector was a major upgrade compared with the previous version of CLEO [20], [21], and has an improved particle identification system together with a new drift chamber and a new silicon vertex detector.

2.2.1 Superconducting Coil

All the detector subsystems except for the muon chambers are located inside a superconduction coil. The coil remains unchanged since CLEO II. It is kept in a superconducting state by liquid helium. The purpose of the coil is to provide a 1.5 Tesla magnetic field, which is uniform to 0.2%, to bend the paths of charged particles in the detector. By measuring how much a charged particle bends, experimenters can measure the momentum of the particle.

The coil inner radius is 1.45m and its outer radius is 1.55 m, with a radial thickness of 0.10 m. The total length of the coil in z is 3.50 m. It is wound from a 5mm x 16 mm superconducting cable (Al surrounding Cu-NbTi strands). It is wound in 2 layers, with 650 turns per layer, on an aluminum shell. When in operation a current of 3300 amps flows through the coil.

2.2.2 Tracking System

After particles from the interaction point pass through the beam pipe, they begin to encounter the active detector elements of the tracking system. There are two sub-detectors responsible for tracking the curving path of charged particles. The first one encountered by particles is the silicon vertex detector, and the second one is the central drift chamber. The CLEO III tracking system is responsible for tracking a charged particle's path and measuring its momentum. Typical momentum resolution is 0.3% (1%) for 1 GeV (5 GeV) tracks. The tracking system also measures ionization energy losses with an accuracy of about 6%.

Silicon Vertex Detector

The silicon vertex detector in CLEO III [22], also called SVD III, is a four-layer barrel-only structure with no endcaps that surrounds the beam pipe. This detector (see Figure 2-4) provides four ϕ and four z measurements covering over 93% of the solid angle. The average radius of inner surface of the four layers is 25 mm, 37.5 mm, 72 mm, 102 mm. The detector is constructed from 447 identical double-sided silicon wafers, each 27.0 mm in ϕ , 52.6 mm in z and 0.3 mm thick. The wafers are instrumented and read out on both sides. The instrumentation on each side consists of an array of aluminum strips on the wafer surface. These strips are connected to preamplifiers at the end of the detector. The inner side has 512 strips in the z direction and the outer side has 512 in the ϕ direction. Therefore each wafer contains 512+512 sensors. The 447 wafers are arranged in the 4 layers, as follows: 7 sections in ϕ , each with 3 wafers in z , total = 21 wafers in the first layer; 10 sections in ϕ , each with 4 wafers in z , total = 40 wafers in the second layer; 18 sections in ϕ , each with 7 wafers in z , total = 126 wafers in the third layer; 26 sections in ϕ , each with 10 in z , total = 260 wafers in the fourth layer.

Charged particles traversing the wafer lose energy and create electron hole pairs. Approximately 3.6 eV is required to create a single electron-hole pair. The electrons and holes then travel in opposite directions in the electric field applied to the surfaces of the wafers until they end up on the aluminum strips, and the detector registers a “hit”. When combined together, the hit on the inner side of a wafer and the hit on the outer side give a measurement of the (z, ϕ) . The wafer position itself determines r .

The Central Drift Chamber

The CLEO III central drift chamber (DR III) is full of a gas mixture with 60% Helium and 40% propane held at about 270 K and at a pressure slightly above one atmosphere. The drift chamber is strung with array of anode wires of gold-plated

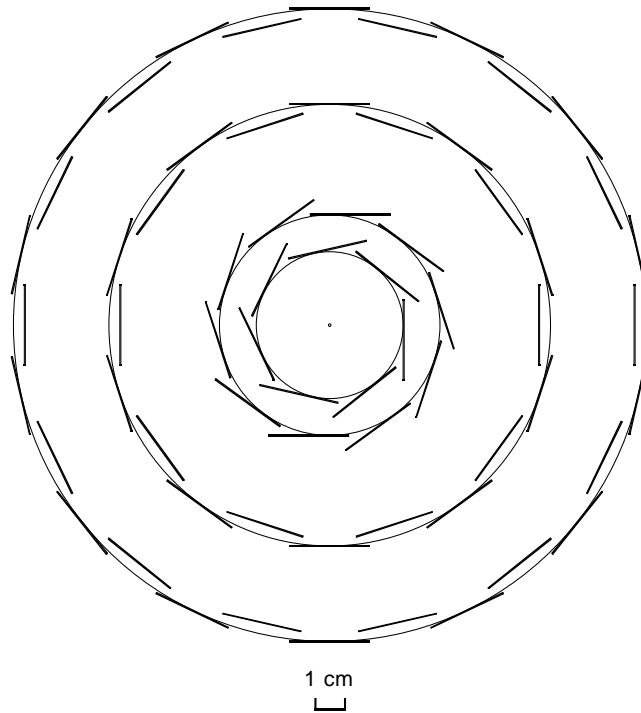


Figure 2-4: View of the SVD III along the beampipe.

tungsten of $20\ \mu\text{m}$ in diameter and cathode wires of gold-plated aluminum tubes of $130\ \mu\text{m}$ in diameter. The anodes are kept at a positive voltage (about 2000 V), and the cathodes are kept grounded, which provides an electric field between the anode and the cathode wires. Anode and cathode wires are often called “sense” and “field” wires respectively.

As a charged particle passes through the DR III, it interacts electromagnetically with the gas molecules giving energy to the outer electrons which become free in a process called ionization. The free electrons from the ionized gas molecules drift in the electric field toward the nearest anode wire. As the electrons get close to the anode, the electric field becomes very strong which causes an avalanche as further ionization is induced. The result of the avalanche is a large number of electrons collapsing upon the sense wire in a very short amount of time (less than one nanosecond). When this happens to a sense wire, we say that there is a “hit”.

The current on the anode wire from the avalanche is amplified and collected at the end of the anode wire. Both the amount of charge and the time it takes it to move to the end of the detector are measured. A calibration of the drift chamber is used to convert the amount of charge to a specific ionization measurement of the incident particle. A calibrated drift chamber can also convert the time to roughly measure the position along the sense wire where the charge was deposited.

The wires are strung along the z direction. About 2/3 of the outer part of the drift chamber (the farthest part from the interaction point) is strung in with a slight angle (about 25 miliradians) with respect to the z direction to help with the z measurement. Wires strung in the z direction are called “axial” wires, while those that are strung at a slight angle are called “stereo” wires.

The DR III consists of an inner stepped section with 16 axial layers, and an outer part with conical endplates and 31 small angle stereo layers. There are 3 field wires per sense wire and they approximately form a 1.4 cm side square. The drift resolution is around $150\ \mu\text{m}$ in $r - \phi$ and about 6 mm in z . All wires are held at sufficient tension to have only a $50\ \mu\text{m}$ gravitational sag at the center ($z = 0$). There are 1696 axial sense wires and 8100 stereo sense wires, a 9796 total.

2.2.3 Ring Imaging Cherenkov Detector

The Ring Imaging Cherenkov (RICH) detector [23] is a new detector subsystem for CLEO III. It replaces the CLEO II.V time of flight system designed to measure particles’ velocities.

Cherenkov radiation occurs when a particle travels faster than the speed of light in a certain medium,

$$v > c/n. \tag{2.1}$$

Where v is the velocity of the particle, c is the speed of light in vacuum, and n is the index of refraction of the medium the particle is traveling in. The charged particle polarizes the molecules of the medium, which then turn back rapidly

to their ground state, emitting radiation. The emitted light forms a coherent wavefront if $v > c/n$ and Cherenkov light is emitted under a constant Cherenkov angle, δ , with the particle trajectory forming a cone of light. The cone half-angle is given by the Cherenkov angle which is,

$$\cos \delta = \frac{c}{vn} = \frac{1}{\beta n}. \quad (2.2)$$

If the radiation angle, δ , is measured, the speed of the incident particle is known. This measurement, combined with the momentum measurement from the tracking system, gives a measurement of the particles mass, and can be used in particle identification.

The threshold velocity at which Cherenkov radiation is emitted is $v_{min} = \frac{c}{n}$. When a particle traveling at the threshold velocity transverses the medium a very small cone with $\delta \approx 0$ is produced. The maximum emission angle occurs when $v_{max} = c$ and is given by

$$\cos \delta_{max} = \frac{1}{n}. \quad (2.3)$$

The RICH (see Figure 2-5) consists of 30 modules in phi, 0.192 m wide and 2.5 m long. The detector starts at a radius of 0.80 m and extends to 0.90 m. Each module has 14 panes of solid crystal LiF radiator at approximately 0.82 m radius, 0.192 m wide, 0.17 m long, 1 cm thick. Inner separation between radiators is typically $50\mu\text{m}$. The LiF index of refraction is $n = 1.5$. The radiators closest to $z = 0$ in each module have a 45 degree sawtooth outer face, to reduce total internal reflection of the Cherenkov light for normal incident particles (see Figure 2-6). The radiators are followed by a 15.7 cm (radial) drift space filled with pure N₂. The drift space is followed by the photodetector, a thin-gap multiwire photosensitive proportional chamber.

With this index, particles in the LiF radiator with $\beta = 1$ produce Cherenkov cones of half-angle $\cos^{-1}(1/n) = 0.84$ radians. With a 16 cm drift

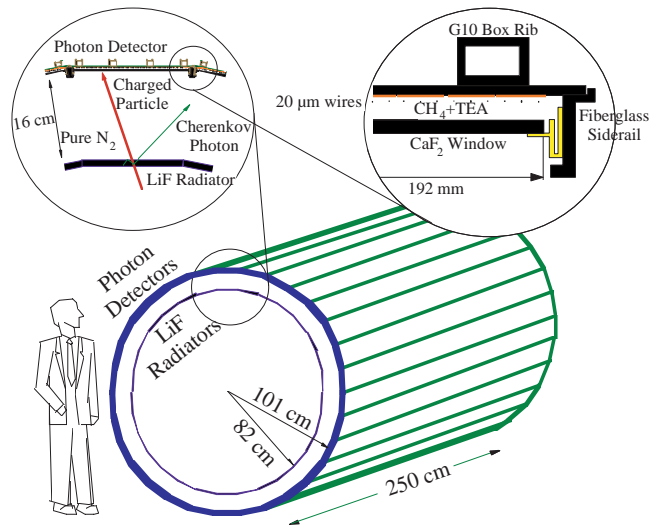


Figure 2-5: The RICH detector subsystem.

space, this produces a circle of radius 13 cm. The RICH is capable of measuring the Cherenkov angle with a resolution of a few milliradians (see Figure 2-7). This great resolution allows for good separation between pions and kaons up to about 3 GeV as Figure 2-8 shows.

2.2.4 Crystal Calorimeter

The CLEO Crystal Calorimeter (CC) is composed of 7784 thallium-doped CsI crystals. Each crystal is 30 cm long (16.2 radiation lengths) with 5cm x 5cm square front face. The crystals absorb any incoming electron or photon which cascades into a series of electromagnetic showers. The electronic system composed of 4 photo-diodes present at the back of each crystal are calibrated to measure the energy deposited by the incoming particle. Other incoming particles other than photons and electrons are partially, and sometimes fully, absorbed by the crystal giving an energy reading.

The CC is arranged into a barrel section and two endcaps, together covering 95% of the solid angle. The CC barrel section is unchanged since CLEO II; the endcaps have been rebuilt for CLEO III to accommodate the new CESR interaction

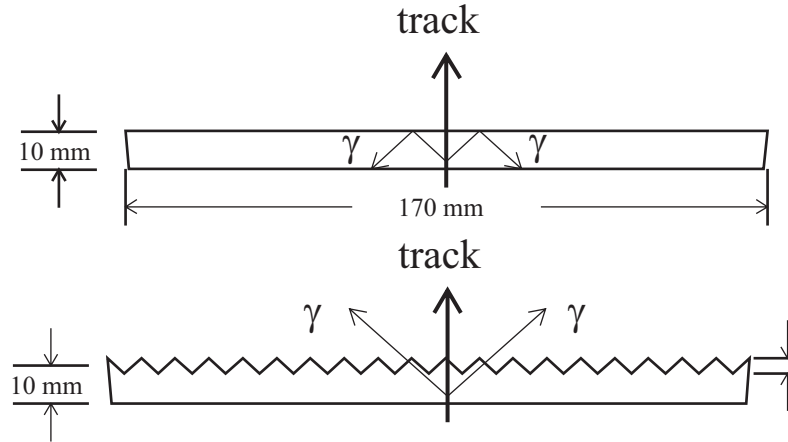


Figure 2-6: The two kinds of RICH LiF radiators. For normal incidence particles ($z \approx 0$) a sawtooth radiator is necessary to avoid internal reflection.

region quadrupoles. The barrel detector consists of an array of 6144 crystals, 128 in ϕ and 48 in z , arranged in an almost-projective barrel geometry. That is, the crystals are tilted in z to point to a few cm away from the interaction point, and there is also a small tilt in ϕ . The CC barrel inner radius is 1.02 m, outer radius is 1.32 m, and the length in z at the inner radius is 3.26 m. It covers the polar angle range from 32 to 148 degrees. The barrel crystals are tapered towards the front face (there are 24 slightly different tapered shapes), the endcap crystals are rectangular, but shaved near the outer radius to fit in the container. The CC endcaps consist of two identical end plugs, each containing 820 crystals of square cross-section, aligned parallel to the beam line (not projective). There are 60 crystals in the "fixed" portion of the "keystone" piece of the endcap. 760 in the part that slides. The keystone is made up of two parts, one on top that has 12 crystals that for mechanical removal reasons is separate from a container holding 48 crystals. The endcap extends from 0.434 m to 0.958 m in r . The front faces are $z = \pm 1.308$ m from the interaction point. It covers the polar angle region from 18 to 34 degrees in $+z$, and 146 to 162 in $-z$.

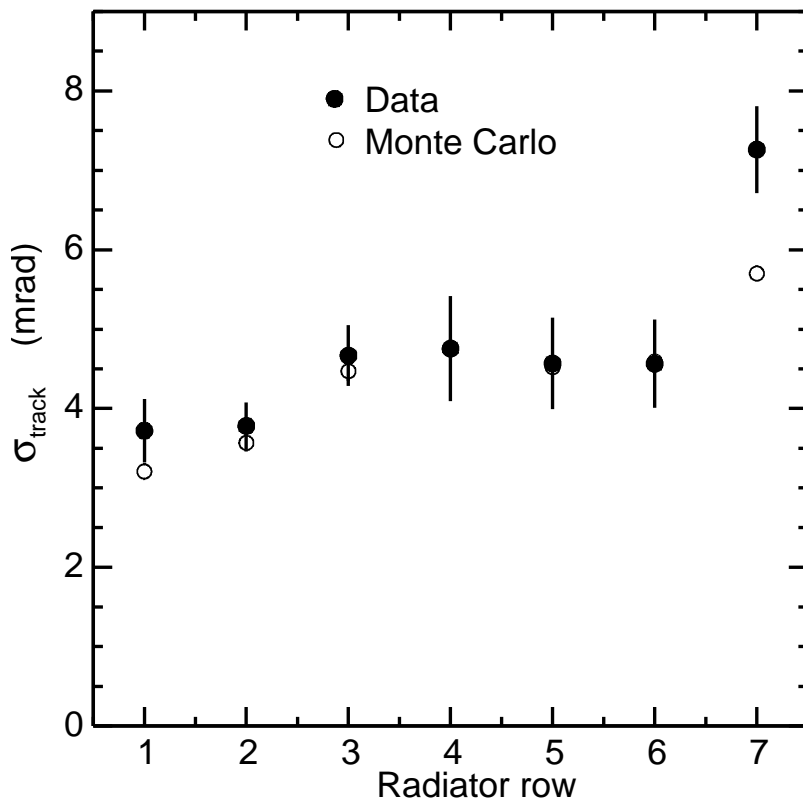


Figure 2-7: Cherenkov angle resolutions per track as a function of radiator row for Bhabha events. Row 1 corresponds to the two rows closest to $z = 0$, etc.

The photon energy resolution in the barrel (endcap) is 1.5% (2.5%) for 5 GeV photons, and goes down to 3.8% (5.0%) for 0.1 GeV photons.

2.2.5 Muon Detectors

The muon detectors (MU) are the most external subsystem of the CLEO III detector. They remain unchanged from CLEO II, and are composed of plastic proportional tubes embedded in the magnet iron return yoke. They cover 85% of the 4π solid angle (roughly 30-150 degrees in polar angle). If a series of hits is detected in the muon chamber layers they most likely correspond to muons because other particles are blocked by the iron. Besides detecting muons, the heavy iron of the return yoke protects the inner subsystems of the CLEO III detector from cosmic ray background (except for cosmic ray muons of course).

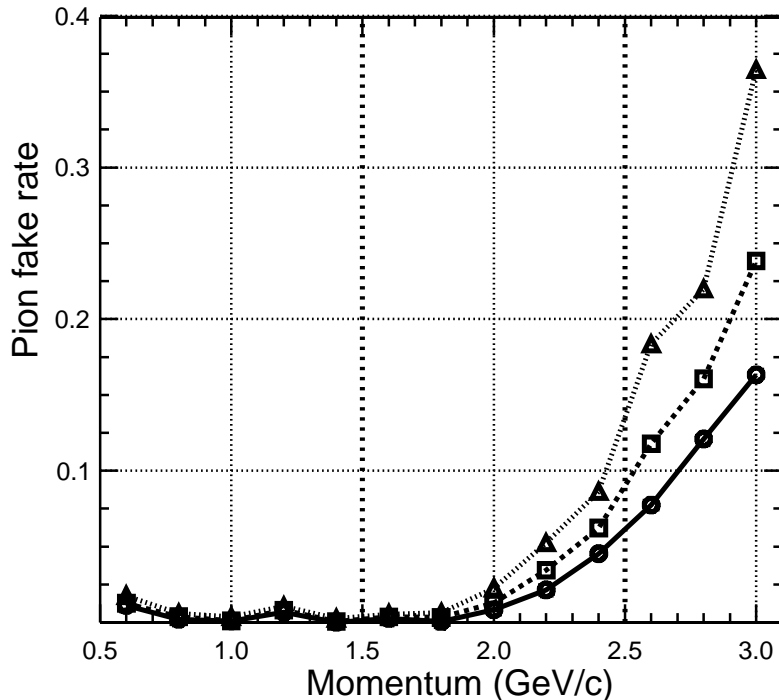


Figure 2-8: Pion fake rate as a function of particle momentum for kaon efficiency of 80% (circles), 85% (squares) and 90% (triangles).

There are three planes of chambers in the barrel section, arranged in 8 octants in ϕ . The plastic barrel planes lie at depths of 36, 72, and 108 cm of iron (at normal incidence), corresponding to roughly 3, 5, and 7 hadronic interaction lengths (16.8 cm in iron) referred to as DPTHMU. There is one plane of chambers in each of the two endcap regions, arranged in 4 rough quadrants in ϕ . They lie at $z = \pm 2.7$ m, roughly covering the region $0.80 < |\cos(\theta)| < 0.85$. The planar tracking chambers use plastic proportional counters at about 2500 V with drift gas of 60% He, 40% propane, identical to (and supplied by the same system as) the drift chamber gas. Individual counters are 5 m long and 8.3 m wide, with a space resolution (along the wire, using charge division) of 2.4 cm. The tracking chambers are made of extruded plastic, 8cm wide by 1 cm thick by 5 m long, containing eight

tubes, coated on 3 sides with graphite to form a cathode, with 50 μm silver-plated Cu-Be anode wires held at 2500 V. The orthogonal coordinate is provided by 8cm copper strips running perpendicular to the tubes on the side not covered by graphite.

CHAPTER 3

ANALYSIS OF THE DATA

This work builds on the techniques developed by previous CLEO radiative $\Upsilon(1S)$ analyses [18], [19], modified to be used with CLEO III data. A new technique based on kinematic fitting is developed to, together with the new RICH detector, improve efficiency and particle identification.

We search for radiative $\Upsilon(1S)$ decays in the modes $\Upsilon(1S) \rightarrow \gamma\pi^+\pi^-, \gamma K^+K^-,$ and $\gamma p\bar{p}$. The e^+e^- collision data has both resonant events, where the e^+e^- annihilate to give a $\Upsilon(1S)$, and continuum events, where the e^+e^- collision does not give a $\Upsilon(1S)$. To be sure we are observing $\Upsilon(1S)$ and not a continuum process, the continuum must be subtracted by using a pure source of correctly scaled continuum events. Pure continuum data can be obtained by operating CESR at an energy different from the $\Upsilon(1S)$ mass. After subtracting the underlying continuum, we examine the di-hadron invariant mass spectrum in search of resonances. We determine the spin and production helicity (the projection of the spin on the momentum vector at production time) of any found resonances by examining the photon and hadron angular distributions.

3.1 Data Sample

The analysis presented here is based on CLEO III data. Throughout this document, and unless otherwise stated we use $\gamma\gamma$ luminosity (the luminosity types used by CLEO are defined at the end of Section 2.1). We prefer to use the $\gamma\gamma$ over the Bhabha luminosity because the resonant process $\Upsilon(1S) \rightarrow e^+e^-$ artificially increases the reported Bhabha luminosity by about 3% in $\Upsilon(1S)$ data. This extra contribution would need to be accounted for when doing a continuum subtraction. Choosing the $\gamma\gamma$ luminosity avoids this complication.

The CLEO III data is divided into numbered sets. Sets 18 and 19 have a luminosity of $1.13 \pm 0.02 fb^{-1}$ in the beam energy range 4.727-4.734 GeV. This data, which we call the $\Upsilon(1S)$ data (or simply the 1S data), has both resonance $e^+e^- \rightarrow \Upsilon(1S)$ and continuum events. We take the number of resonant events from [24], $N_{\Upsilon(1S)} = (2.1 \pm 0.1) \times 10^7$. This number contrasts with the previous generation measurement of CLEO II, where $N_{\Upsilon(1S)} \approx 0.15 \times 10^7$ were available.

In datasets and 18 and 19 there are also $0.192 \pm 0.004 fb^{-1}$ taken below the $\Upsilon(1S)$ beam energy (4.714-4.724 GeV). This data, which we call the $\Upsilon(1S)$ -off data (or simply the 1S-off data), has relatively low statistics and corresponds to purely continuum events.

To improve our continuum statistics we use $3.49 \pm 0.07 fb^{-1}$ from datasets 9, 10, 12, 13, and 14 of data taken near the center-of-mass energy of the $\Upsilon(4S)$, which for our purposes is defined as data with beam energy in the 5.270-5.300 GeV range. This set of data, which we call the $\Upsilon(4S)$ data (or simply the 4S data), is a source of pure continuum because no $\Upsilon(4S) \rightarrow B\bar{B}$ resonant event can survive our “cuts”¹ (the cuts are presented in Section 3.3).

3.1.1 Continuum Subtracted Distributions

We use the continuum data taken at the $\Upsilon(4S)$ energy to subtract the underlying continuum present in the $\Upsilon(1S)$ data. This is important because continuum background processes like $e^+e^- \rightarrow \gamma\rho$ with $\rho \rightarrow \pi^+\pi^-$, $e^+e^- \rightarrow \gamma\phi$ with $\phi \rightarrow K^+K^-$, and direct $e^+e^- \rightarrow \gamma h^+h^-$ (we will use the convention $h = \pi, K, p$ from now on), look like the signal events we are searching for. To first order, the cross section of these continuum process scales like $1/s$, where s is the square of

¹ Cuts are simply conditions that an event must satisfy to be considered in the analysis. Cuts are necessary to eliminate background that would otherwise make a measurement difficult or even impossible.

the center of mass energy of the e^+e^- system. Taking the luminosity-weighted average beam-energies of each interval, and the $\gamma\gamma$ luminosities (see Table 3-1), we calculate that the $\Upsilon(4S)$ data scaled down by a factor of 0.404² represents the underlying continuum in the $\Upsilon(1S)$ data. This is true up to differences in momentum distributions and phase space. The error in the continuum scale factor is unknown because the luminosity ratio is expected to have a small but undetermined systematic error. We make the somewhat arbitrary decision to retain three significant digits in the continuum scale factor because it is sufficient for our purposes and there are 0.5% effects from second order terms in the cross section formulae.

To eliminate the contribution of continuum events from a $\Upsilon(1S)$ data variable distribution (e.g., the invariant mass of two tracks, the photon angular distribution) we proceed as follows,

- Obtain the $\Upsilon(4S)$ data distribution for the same variable.
- Efficiency correct both the $\Upsilon(1S)$ and $\Upsilon(4S)$ distributions, using a

GEANT [25] based Monte Carlo (MC) simulation of the detector. Examples of MC efficiency distributions are shown in Figures 3-3 and 7-3.

² If we are to be mathematically strict we should calculate the scale factor as

$$\sum_{1S \text{ runs}} \frac{\mathcal{L}_{1S \text{ run}}}{s_{1S \text{ run}}} \bigg/ \sum_{4S \text{ runs}} \frac{\mathcal{L}_{4S \text{ run}}}{s_{4S \text{ run}}}$$

with obvious notation. This is equivalent to redefining the average energy as

$$\frac{1}{\bar{E}^2} = \frac{1}{\mathcal{L}} \sum_{runs} \frac{\mathcal{L}_{run}}{E_{run}^2}.$$

However, our energy intervals are sufficiently narrow and this calculation does not change the last significant digit of the original scale factor. Similarly, taking into account second order terms in the energy dependence of the cross section, like the one that appears as m_ρ^2/s in the explicit formula for the $e^+e^- \rightarrow \gamma\rho$ cross section, also has an insignificant effect on the scale factor.

- Subtract the $\Upsilon(4S)$ distribution from the $\Upsilon(1S)$ distribution using a $\Upsilon(4S)$ scale factor of 0.404.

We call this set of steps “continuum subtraction” by definition. For compactness, we call such a distribution the “continuum subtracted <variable> distribution/plot” or “<variable> continuum subtracted distribution/plot”. Except for statistical fluctuations and phase space effects, the resulting 1S distribution should not have any contribution from continuum processes that scale as $1/s$.

It is important to notice that any continuum subtracted distribution is efficiency corrected. This means that a fit to a continuum subtracted distribution (for example, the continuum subtracted invariant mass distribution) gives the efficiency corrected number of events directly. Strictly speaking, this number of events is only correct if all the other variables we cut on have the same initial distribution in data and MC, or if the efficiency does not depend on them. In this note we use “flat MC”, defined as MC that is generated with a flat distribution in the mass and the helicity angles θ_γ , θ_π (these angles are defined in the appendix).

For example, the number of events obtained from the continuum subtracted invariant mass fit needs to be corrected to account for the fact that the helicity angle distributions are not flat in data (see for example Figure 4–9, and the efficiency is highly dependent on these variables (see Figure 7–3). This correction is done in Section 7.2.

A summary of the results from this section is shown in Table 3–1.

3.2 Event Selection

Event selection for $\Upsilon(1S) \rightarrow \gamma h^+ h^-$ is straightforward and can be thought of in terms of three major stages.

First we skim the data, keeping only those events that contain exactly one high-energy photon and two tracks. Next, we require that the total 4-momentum of these three elements be consistent with the colliding e^+e^- 4-momentum. Finally,

Table 3–1: Summary of the data used in this analysis. The continuum scale factor is obtained using $\gamma\gamma$ luminosities because the Bhabha luminosity is artificially high during $\Upsilon(1S)$ running due to the process $\Upsilon(1S) \rightarrow e^+e^-$.

	$\Upsilon(1S)$	$\Upsilon(4S)$	$\Upsilon(1S)\text{-off}$
Dataset	18, 19	9, 10, 12, 13, 14	18, 19
Average E_{beam} (GeV)	4.730	5.286	4.717
Range of E_{beam} (GeV)	4.727–4.734	5.270 – 5.300	4.714 – 4.724
$\mathcal{L}(e^+e^-)(fb^{-1})$	1.20 ± 0.02	3.56 ± 0.07	0.201 ± 0.004
$\mathcal{L}(\gamma\gamma)(fb^{-1})$	1.13 ± 0.02	3.49 ± 0.07	0.192 ± 0.004
$\Upsilon(1S)$ continuum scale factor	1	0.404	5.84

in the third stage, we project the surviving data onto the three different hadronic modes via hadron separation and QED suppression cuts.

However, checking the 4-momentum involves using the tracks masses. This means that the information from stage 2 should somehow be useful in stage 3. This is indeed the case, and the details of how we do it are revealed in this section.

3.2.1 Skim Cuts

We skim over the data in the “hardGam” subcollection. The hardGam subcollection was developed with this type of analysis in mind. For an event that passes the triggers ³ to be classified as hardGam it must pass the following cuts,

- $eGam1 > 0.5$
- $eSh2 < 0.7$
- $eOverP1 < 0.85$
- $eVis > 0.4$
- $aCosTh < 0.95$ where “eGam1” is the highest isolated shower energy

relative to the beam energy, “eSh2” is the energy of the second highest shower relative to the beam energy, “eOverP1” is the matched shower energy relative to

³ Triggers are basic criteria that an event must satisfy to be recorded during the data collection processes. Triggers are designed to get rid of trash and noise and reduce the size of the data sample while keeping all of the important information.

the momentum of the track with highest momentum, “eVis” is the total energy detected (charged tracks are assumed to be pions) relative to the center of mass energy, and “aCosTh” is the z component of the unitary total momentum vector.

Monte-Carlo predicts that about 75% of the generated $\Upsilon(1S) \rightarrow \gamma h^+ h^-$ signal passes the hardware and software triggers and gets classified as hardGam.

As mentioned above, we use this data to make our skim. To write an event from the hardGam subcollection into our skim we require the following topological cuts,

- There are exactly two “good tracks”; there can be any number of tracks that are not “good tracks” but these are not used in the analysis. We define a “good track” as a track that satisfies the following cuts; drift chamber track ionization energy loss (dE/dX) information is available, the ratio of number of wire hits to those expected is between 0.5 and 1.5, the pion fit has $\chi^2/d.o.f. < 20$ (here d.o.f. stands for degrees of freedom), and the distance of closest approach to the beam spot in the x-y plane (called DBCD) is less than $5 - 3.8P$ (mm) if $P < 1$ GeV/c (where P is the tracks momentum in GeV/c) and less than 1.2 mm for tracks with $P > 1$ GeV/c. This DBCD cut is common in the more sophisticated CLEO II/II.5 analyses. It performs better than a simple $DBCD < 5$ mm cut, because it takes into account the fact that tracks with higher momentum have a better measurement of DBCD since they scatter less.

- There is exactly one “good shower”, there can be any number of showers that are not “good showers” but these are not used in the analysis. We define a “good shower” as an unmatched shower with energy > 4 GeV.

These topological cuts are about 85% efficient for generated signal events that have passed the triggers and have been classified as hardGam.

The overall skim efficiency is between 60-65%, depending on the mode (see Table 3-4).

3.2.2 Analysis Cuts

After our skim we call any cuts we make “analysis cuts”. These cuts are done at analysis time and are mode dependent. As a convention, and unless otherwise stated, efficiencies for individual analysis cuts are reported relative to the events in the skim (not relative to the events generated).

4-momentum Cut

All fully reconstructed events should have the 4-momentum of the e^+e^- system. This constraint is usually implemented with a simple two-dimensional ΔE - p box cut, where ΔE is the difference between the reconstructed energy for the event and the colliding e^+e^- energy (E_{CM}), and p is the magnitude of the reconstructed total momentum for the event. Typical values for these cuts are $-0.03 < \Delta E/E_{CM} < 0.02$ and $p < 150$ MeV/c (taken from [19]).

The traditional ΔE - p box cut is somewhat useful. However, it does not take into account the correlation between the measured energy and momentum. Indeed, the signal lies in diagonal bands in the ΔE - p plane, making a box-shaped cut not optimal (see Figures 3–1a and 3–1b).

We use an alternative approach to the 4-momentum cut. After a simple substitution, $E_\gamma = p_\gamma = E_{CM} - E_{h+h-}$ (where E_γ is the photon’s energy, p_γ is the magnitude of the photons momentum, E_{CM} is the energy of the e^+e^- system, and E_{h+h-} is the energy of the hadron pair), we can write the E- p conservation equations as:

$$\vec{p}_{h+h-} + (E_{CM} - E_{h+h-})\hat{p}_\gamma = \vec{p}_{CM} \quad (3.1)$$

where, \vec{p}_{h+h-} is the di-hadron momentum, \hat{p}_γ is the photon’s momentum unit vector, and \vec{p}_{CM} is the momentum of the e^+e^- system (which is a few MeV because of the crossing angle). Equation 3.1 is a 3-constraint subset of the 4-momentum constraint and has the convenient property of avoiding the use of the measured photon’s energy, which has non-Gaussian asymmetric errors. It is important to

notice that Equation 3.1 contains the di-hadron energy, therefore, it can help discriminate between the various particle hypotheses.

We proceed as follows. After vertexing the hadron pair using the beam spot with its error matrix, we calculate the photon's direction from the hadron pair's vertex and the shower position. We then fit the event to the 3 constraints expressed in Equation (1) using the techniques outlined in [26] and cut on the χ^2 of the 3-constraint fit, $\chi_{E-p}^2(h) < 100$. To complete the 4-momentum requirement, we calculate $\Delta E(h) = E_{h+h-} + E_\gamma - E_{CM}$, where E_{h+h-} is the updated di-hadron energy after the constraint, and E_γ is the measured photon's energy, and require $-0.050 * E_{CM} < \Delta E(h) < 0.025 * E_{CM}$. Furthermore, we now have available $\chi_{E-p}^2(h)$ differences between different particle hypotheses, which help in particle identification (ID). This is discussed in more detail in the next section. Figure 3-1 compares the performance of the old and new approaches to the E-p cut.

At this point it is a good idea to check that the 4-momentum cut rejects background events that make it through our skim cuts (see Section 3.1). These events typically have one high energy shower, two tracks, and (an) additional element(s). One such background is $\Upsilon(1S) \rightarrow \gamma\pi^+\pi^-\pi^0$. Out of 25000 $\Upsilon(1S) \rightarrow \gamma\eta$, with $\eta \rightarrow \pi^+\pi^-\pi^0$ MC events ⁴ only 4 survive our 4-momentum cut. We conclude that our 4-momentum cut is good at rejecting background events that pass the skim cuts but have additional elements such as an extra photon, π^0 , pair of tracks, etc.

⁴ Thanks to Vijay Potlia for generating these events

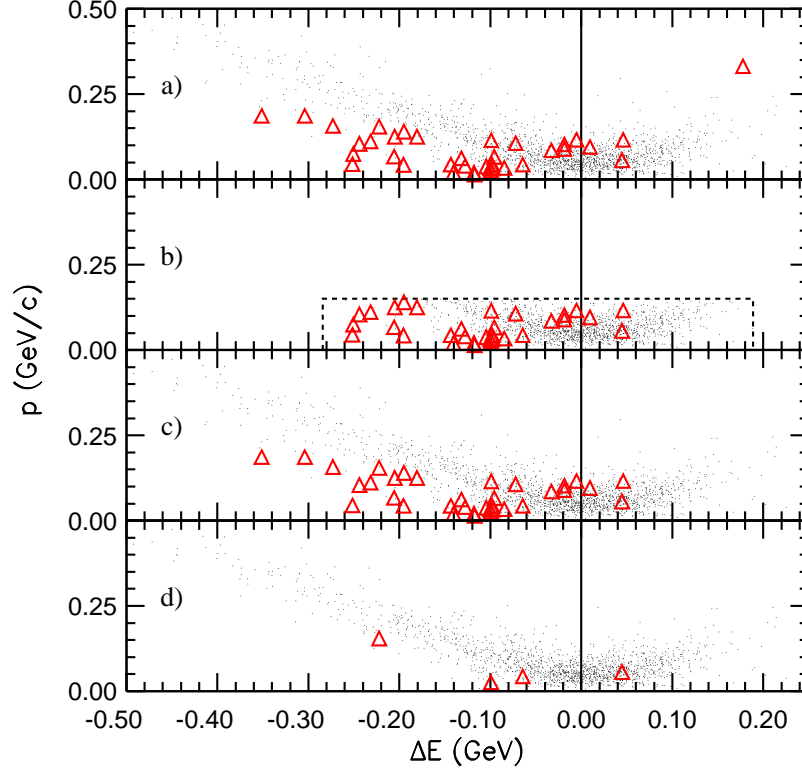


Figure 3-1: Distributions for different 4-momentum cuts. Signal MC events ($\Upsilon(1S) \rightarrow \gamma\pi^+\pi^-$) are represented by the black dots, and “background” MC events ($e^+e^- \rightarrow \gamma\phi, \phi \rightarrow K^+K^-$) appear as (red) triangles. Plot a) has no cuts. Plot b) has the old 4-momentum box-cut. Plot c) has the new 4-momentum cuts. Plot d) has the new 4-momentum cuts, and also a cut defined as $\chi^2_{E-p}(\pi) - \chi^2_{E-p}(K) < 0$. The particle ID potential of the newly available $\chi^2_{E-p}(h)$ is evident.

Hadron Separation

We define $\Delta\chi^2_{ID}(h_1 - h_2)$ for the particle hypotheses h_1 and h_2 of our charged track pair (e.g. $\Delta\chi^2_{ID}(\pi - K)$) as follows,

$$\begin{aligned} \Delta\chi^2_{ID}(h_1 - h_2) = & \sigma^2_{dE/dX}(h_1^+) - \sigma^2_{dE/dX}(h_2^+) + \sigma^2_{dE/dX}(h_1^-) - \sigma^2_{dE/dX}(h_2^-) \\ & - 2\log(\mathcal{L}_{RICH}(h_1^+)) + 2\log(\mathcal{L}_{RICH}(h_2^+)) \\ & - 2\log(\mathcal{L}_{RICH}(h_1^-)) + 2\log(\mathcal{L}_{RICH}(h_2^-)). \end{aligned} \quad (3.2)$$

where the idea is to combine the dE/dX and RICH information into one number.

Pairs of tracks with $\Delta\chi^2_{ID}(h_1 - h_2) < 0$ are more likely to be of type h_1 than of type h_2 .

In practice, we only add a tracks RICH information if its momentum is above the Cherenkov radiation threshold for both mass hypotheses and there are at least 3 photons within 3σ of the Cherenkov angle for at least one of the mass hypothesis. We also require that both hypotheses were actually analyzed by RICH during pass2.

In addition to RICH and dE/dX , and as hinted in the previous section, the difference in $\chi_{E-p}^2(h)$ from the constraint expressed in Equation 3.1 can help the particle ID (see Figures 3–1c and 3–1d). We define,

$$\Delta\chi_{E-p}^2(h_1 - h_2) = \chi_{E-p}^2(h_1) - \chi_{E-p}^2(h_2). \quad (3.3)$$

Events with $\Delta\chi_{E-p}^2(h_1 - h_2) < 0$ are more likely to be of type h_1 than of type h_2 .

In this analysis, to select h_1 and reject h_2 the default cut is simply $\Delta\chi_{ID}^2(h_1 - h_2) < 0$. This simple cut is highly efficient, has low fake rates, and is sometimes sufficient. However, out of the six possible cases when one hadron fakes another, there are three important cases where it pays off to also use $\Delta\chi_{E-p}^2(h_1 - h_2)$ together with $\Delta\chi_{ID}^2(h_1 - h_2)$ in an optimal way;

1. π background to K . This background comes from the continuum process $e^+e^- \rightarrow \gamma\rho, \rho \rightarrow \pi^+\pi^-$.
2. π background to p . Again, this background comes from the continuum process $e^+e^- \rightarrow \gamma\rho, \rho \rightarrow \pi^+\pi^-$.
3. K background to p . This background comes from the continuum process $e^+e^- \rightarrow \gamma\phi, \phi \rightarrow K^+K^-$.

In other words, the important cases occur when the lighter mass hypothesis fakes the heavier mass hypothesis.

Mathematically, one would expect that simply adding both $\Delta\chi_{ID}^2$ and $\Delta\chi_{E-p}^2$ together (like we just did when combining RICH and dE/dX), and cutting on the

grand $\Delta\chi^2$ is the way to go. Unfortunately, this simple approach fails because of large non-mathematical tails in the individual χ^2_{E-p} distributions.

Instead, for each of these three cases we define the best cut values (c_1, c_2) in $\Delta\chi^2_{ID} < c_1$ and $\Delta\chi^2_{E-p} < c_2$ as those that maximize

$$F(c_1, c_2) = \frac{R_e}{\sqrt{R_e + W * R_f}}, \quad (3.4)$$

where R_e (R_f) is the efficiency (fake rate) of the particle ID cuts and W is the rough ratio of the background to signal in the data sample for each case. Each W can't be known *a priori*, but a rough idea of its value can be obtained by doing a first iteration of the analysis with, for example, $c_1 = c_2 = 0$. We use $W = 20$, $W = 60$, and $W = 30$ for cases 1-3 respectively. Figure 3-2 shows $F(c_1, c_2)$ for each case. Table 3-2 shows the optimized cut values and their effect on particle ID.

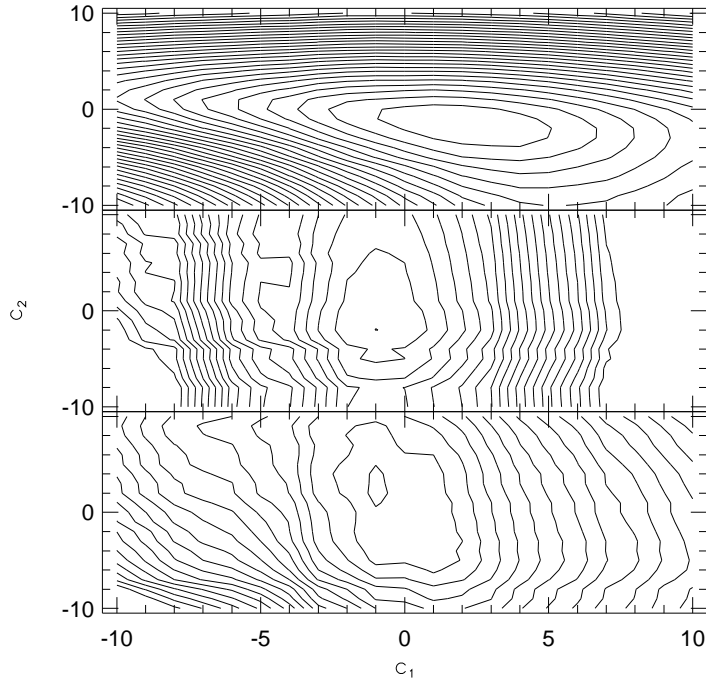


Figure 3-2: Contour plots of $F(c_1, c_2)$ as defined in Equation 3.4 for different signals and backgrounds from flat MC. Top has a K signal and a π background. Center has a p signal and a π background. Bottom has a p signal and a K background.

Table 3–2: Cut values, efficiencies, and fake rates for $\Delta\chi^2_{ID} < c_1$ and $\Delta\chi^2_{E-p} < c_2$ in flat MC. The different c_1, c_2 values are chosen so F from Equation 3.4 is maximun. Efficiency and fake rates of each cut are reported relative to events in the skim. Statistical errors in the efficiencies are 0.1% or less. Errors in the fake rates are statistick and are shown for completeness only.

	Cut Value		Signal efficiency (%)			Fake rate (%)		
	c_1	c_2	$\Delta\chi^2_{ID}$	$\Delta\chi^2_{E-p}$	Both	$\Delta\chi^2_{ID}$	$\Delta\chi^2_{E-p}$	Both
π faking K	3	-2	94.2	95.2	89.9	1.73 ± 0.09	14.5 ± 0.3	0.31 ± 0.04
π faking p	-1	-2	99.0	99.8	98.9	0.89 ± 0.06	1.03 ± 0.07	0.03 ± 0.01
K faking p	-1	3	98.8	99.3	98.1	1.89 ± 0.09	1.09 ± 0.07	0.10 ± 0.02

Quantum Electrodynamic Suppression

Quantum Electrodynamic (QED) background in this analysis comes from the abundant processes $e^+e^- \rightarrow \gamma e^+e^-$ and $e^+e^- \rightarrow \gamma\mu^+\mu^-$.

To reject $e^+e^- \rightarrow \gamma e^+e^-$ we require both tracks to have a matched shower with energy E such that $|E/p(\pi) - 0.95| > 0.1$, and to have $\Delta\chi_{ID}^2(h - e) < 0$.

To reject $e^+e^- \rightarrow \gamma\mu^+\mu^-$ we simply require $DPTHMU < 5$ ($DPTHMU$ was defined in Section 2.2.5) for both tracks in the K and p modes because particle ID cuts make the pion (and therefore the muon) fake rate small (see Tables 3–2 and 3–6). For the π mode we cannot use particle ID in a practical way because muons and pions have similar masses. Instead, to separate pions and muons we use a much stronger cut requiring that both tracks be within the barrel part of the muon chamber ($|\cos(\theta)| < 0.7$), both have $P > 1$ GeV/c and both have $DPTHMU < 5^5$.

To improve the overall muon suppression cut efficiency with virtually no increase in muon fakes, we flag an event as “not muonic” if any of the tracks deposit more than 600 MeV in the CC. This increases the cut efficiency by about 90% in the π mode and makes the detector more hermetic.

3.2.3 Cut Summary, Efficiencies, and Fake Rates

Table 3–3 summarizes the cuts used in this analysis. Figure 3–3 shows the overall Monte Carlo efficiency after all cuts. Figure 3–4 shows the fake rates according to the MC and the data for different particle ID cuts. The data fake rates and limit fake rates, which are measured for pions and kaons faking other

⁵ Other analyses (for example [18]) typically use $DPTHMU < 3$, our CLEO III MC has too many pion tracks with $3 < DPTHMU < 5$ and too few tracks with $DPTHMU = 0$.

hadrons, are calculated from the ρ and ϕ peaks in the continuum (see Figures 4-2 and 5-1). Tables 3-4 through 3-6 summarize the results of Figures 3-3 and 3-4.

Table 3–3: Cuts used in this analysis.

Motivation	Definition for $\Upsilon(1S) \rightarrow \gamma h^+ h^-$ (where $h = \pi, K$, or p)
Skim cuts	
Data acquisition	Event must pass hardware (Level1) and software triggers (pass2) and be of type hardGam
Topological	There are only two good tracks and only one isolated shower with $E > 4$ GeV
Analysis cuts	
Reconstructed event must have 4-momentum of the center-of-mass system	$\chi_{E-p}^2(h) < 100.0$ and $-0.050 < \Delta E(h)/E_{CM} < 0.025$
Hadron separation	Default is, $\Delta\chi_{ID}^2 < 0$. The three cases with a large fake population because of continuum processes use a simultaneously optimized cut on $\Delta\chi_{ID}^2$ and $\Delta\chi_{E-p}^2$, and are summarized in Table 3–2
QED background $e^+e^- \rightarrow \gamma e^+e^-$	Both tracks have a matched shower energy E that satisfies $ E/p(\pi) - 0.95 > 0.1$, and $\Delta\chi_{ID}^2(h - e) < 0$
QED background $e^+e^- \rightarrow \gamma\mu^+\mu^-$	For $h = K, p$ both tracks have $DPTHMU < 5$. For $h = \pi$ (At least one track has a matched shower energy > 600 MeV) or ((Both tracks have $\cos(\Theta) < 0.7$ and $P > 1$ GeV/c) and (both tracks have $DPTHMU < 5$))

Table 3–4: Efficiencies in % for cuts (as outlined in Table 3–3) for flat signal MC. Efficiencies in the second group are reported relative to the number of candidates that make it to the skim. The third part of the table shows the overall reconstruction efficiency. Statisticall errors are 0.1% or less.

Skim cuts	π	K	p
Hardware Trigger	89.7	89.0	90.9
Software Trigger	96.5	96.2	96.6
hardGam	78.4	79.9	76.5
Topological ($n_{tracks} = 2$ & $E_\gamma > 4GeV$)	73.3	67.6	72.3
Overall Skim efficiency	64.3	60.3	62.4
Analysis cuts	π	K	p
4-momentum	98.6	98.5	99.0
QED $e^+e^- \rightarrow \gamma e^+e^-$ suppression	93.9	87.4	93.1
QED $\mu^+\mu^- \rightarrow \gamma\mu^+\mu^-$ suppression	74.7	93.0	98.3
Hadron separation	97.1	89.0	97.8
Overall analysis efficiency	66.9	79.1	89.1
Overall reconstruction efficiency	43.0	47.6	55.6

Table 3–5: Efficiencies in % for cuts (as outlined in Table 3–3) for flat 4S MC. Efficiencies in the second group are reported relative to the number of candidates that make it to the skim. The third part of the table shows the overall reconstruction efficiency. Statisticall errors are 0.1% or less.

Skim cuts	π	K	p
Hardware Trigger	88.4	88.0	89.0
Software Trigger	94.6	94.6	94.8
hardGam	79.2	80.5	77.9
Topological ($n_{tracks} = 2$ & $E_\gamma > 4GeV$)	75.2	69.5	75.8
Overall Skim efficiency	66.9	62.7	66.6
Analysis cuts	π	K	p
4-momentum	97.1	97.0	97.4
QED $e^+e^- \rightarrow \gamma e^+e^-$ suppression	93.4	89.1	93.2
QED $\mu^+\mu^- \rightarrow \gamma\mu^+\mu^-$ suppression	75.8	92.5	98.1
Hadron separation	98.0	91.4	96.6
Overall analysis efficiency	67.4	80.2	87.3
Overall reconstruction efficiency	45.0	50.3	58.2

Table 3–6: Final efficiencies and fake rates after all cuts in %. Statistical errors for efficiencies are 0.1% or less. Statistical errors for fake MC rates are shown for completeness only. The 1S DATA corresponds to the 1S off resonance data sample. The MC was generated flat.

	π cuts	K cuts	p cuts
1S π MC	43.0	0.14 ± 0.01	< 0.007
4S π MC	45.0	0.29 ± 0.02	< 0.01
1S ρ DATA	–	< 1.2	< 0.2
4S ρ DATA	–	0.20 ± 0.06	< 0.06
1S K MC	1.27 ± 0.03	47.6	< 0.02
4S K MC	0.92 ± 0.04	50.3	< 0.06
1S ϕ DATA	< 3.8	–	< 2.0
4S ϕ DATA	4.14 ± 0.69	–	< 0.4
1S p MC	0.08 ± 0.02	0.34 ± 0.04	55.6
4S p MC	0.05 ± 0.01	0.37 ± 0.01	58.2

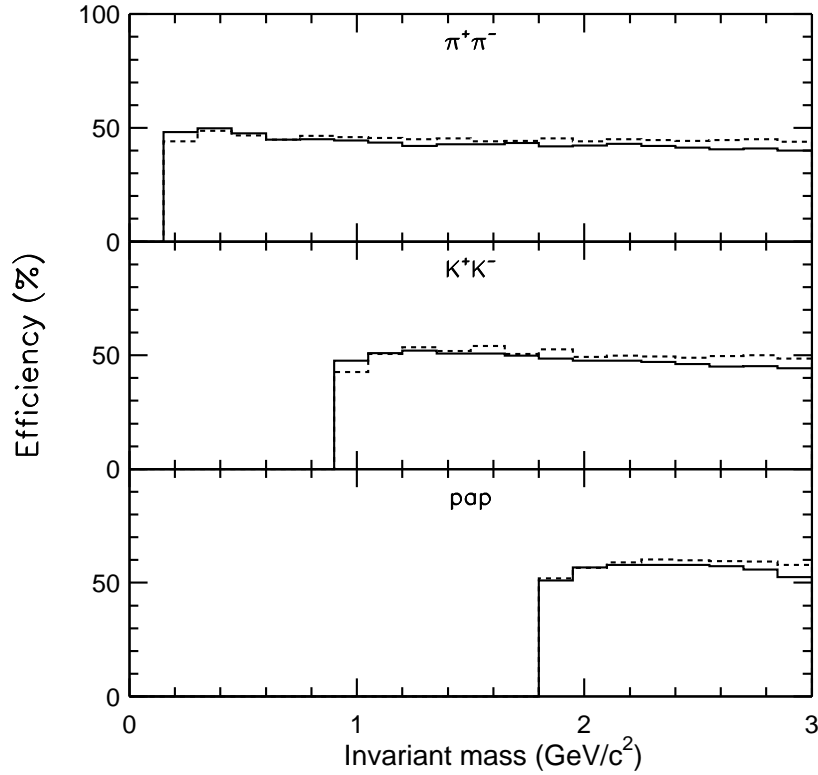


Figure 3–3: Final efficiencies for each mode as a function of invariant mass for the 1S (solid) and 4S (dashed) Monte Carlo data. The MC was generated with a flat angular distribution.

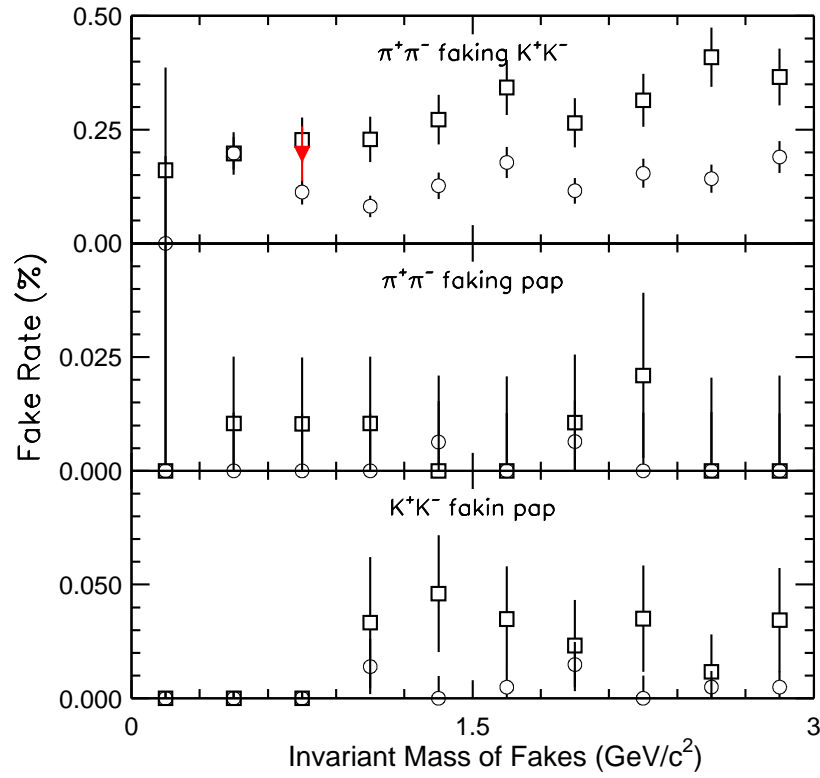


Figure 3–4: Fake rates for 1S (hollow circles) and 4S (hollow squares) according to flat MC. The (red) downward pointing triangle is obtained using the ρ peak in 4S data.

CHAPTER 4

EXCLUSIVE RADIATIVE DECAY $\Upsilon(1S) \rightarrow \gamma\pi^+\pi^-$

In Figure 4–2 the $\pi^+\pi^-$ invariant mass plot is shown for both 1S and 4S data. Figure 4–3 shows the continuum subtracted $\pi^+\pi^-$ invariant mass distribution (as defined in Section 3.2.1) with the most likely statistical fit overlayed (which is described in the next section). The number of events within 1Γ of the ρ region ($0.62 - 0.92 \text{ GeV}/c^2$) left after the continuum subtraction is 200 ± 300 , and 50 of these belong to the $f_0(980)$ low-mass tail.

4.1 Robustness of The Mass Distribution

In [27] the decay $\Upsilon(1S) \rightarrow \gamma\pi^0\pi^0$ is analyzed, and it is shown how the analysis stream warps the shape of the reconstructed resonance. This effect, which arises because of the particular π^0 behavior, raises problems when fitting the invariant mass distribution.

In Section 3.2.1 we claimed that if the data and MC had the same θ_γ and θ_π distributions, the fit to the continuum subtracted invariant mass distribution automatically gives the correct efficiency corrected number of events.

Here we test this claim. To this end, we generate 10000 $\Upsilon(1S) \rightarrow \gamma f_2(1270)$, with $f_2(1270) \rightarrow \pi^+\pi^-$ with flat θ_γ and θ_π distributions. We treat this MC as data and carry out the first two steps of the continuum subtraction process. The resulting peak has a mass of $1.278 \pm 0.002 \text{ GeV}/c^2$ and a width of $0.193 \pm 0.006 \text{ GeV}/c^2$, consistent with the generated mass and width of $1.275 \text{ GeV}/c^2$ and $0.185 \text{ GeV}/c^2$. More importantly, the number of reconstructed events from the fit is 10040 ± 180 , which is consistent with the number of generated events.

Figure 4–1 shows the reconstructed and efficiency corrected events, a fit to them, and the generated events.

We conclude that there is no warping of the mass distribution, and that the analysis stream behaves like we expect when obtaining the efficiency corrected number of events from data.

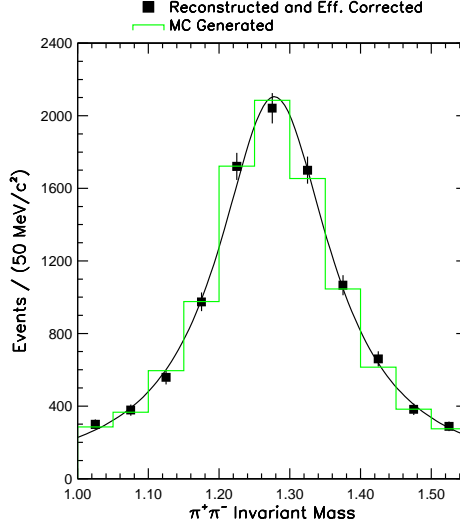


Figure 4–1: Reconstructed events and efficiency corrected events, a fit to them, and the generated events for $\Upsilon(1S) \rightarrow \gamma f_2(1270)$, with $f_2(1270) \rightarrow \pi^+\pi^-$ with flat θ_γ and θ_π distributions.

4.2 Statistical Fit of the Invariant Mass Distribution

The results of this section are summarized in Table 4–1.

Figure 4–3 shows possible signals for $\Upsilon(1S) \rightarrow \gamma f_0(980)$, $\Upsilon(1S) \rightarrow \gamma f_2(1270)$ and $\Upsilon(1S) \rightarrow \gamma f_4(2050)$. To determine the number of events in each signal we fit the invariant $\pi^+\pi^-$ mass continuum subtracted distribution with three spin-dependent, relativistic Breit-Wigner line shapes. The masses and widths are allowed to float, except for the width of the $f_4(2050)$ which has a very large error if allowed to float and is set to its PDG value. The PDG values[16] for the mass and width of the three resonances are $m_{f_0(980)} = 980 \pm 10 \text{ MeV}/c^2$, $\Gamma_{f_0(980)} = 70 \pm 15 \text{ MeV}/c^2$, $m_{f_2(1270)} = 1275.4 \pm 1.2 \text{ MeV}/c^2$, $\Gamma_{f_2(1270)} = 185.1^{+3.4}_{-2.6} \text{ MeV}/c^2$, $m_{f_4(2050)} = 2034 \pm 11 \text{ MeV}/c^2$, and $\Gamma_{f_4(2050)} = 222 \pm 19 \text{ MeV}/c^2$.

To measure the statistical significance of each signal we do multiple χ^2 fits fixing the signal area to different values while letting the mass and width of

the signal whose significance is being measured to float within 2σ of the PDG values. At the same time the rest of the fit parameters are fixed to the values that originally minimized the χ^2 . We assign each of these multiple fits a probability proportional to $e^{-\chi^2/2}$ and then normalize. We calculate the chance of the signal being due to a random fluctuation by adding the normalized probabilities for the fits with a negative or 0 signal. This method fails for the highly significant $f_2(1270)$ signal because the $e^{-\chi^2/2}$ value of fits with negative or 0 $f_2(1270)$ signal is of the order of 10^{-54} and our computing software can only handle numbers as small as 10^{-45} . For completeness we state that the significance of this signal is $< 10^{-45}$.

To measure the upper limit for the $f_J(2220)$ we also do multiple χ^2 fits for different fixed signal values, while keeping its mass and width constant at $m_{f_J(2220)} = 2.234 \text{ GeV}/c^2$ and $\Gamma_{f_J(2220)} = 17 \text{ MeV}/c^2$ as in [17]. The resulting probability plot is shown in Figure 4–5.

We find clear evidence for the $f_2(1270)$, evidence for the $f_0(980)$ and weak evidence for the $f_4(2050)$. We also put a 90% confidence level upper limit on $f_J(2220)$ production. Fit results are shown in Table 4–1.

Table 4–1: Results for $\Upsilon(1S) \rightarrow \gamma\pi^+\pi^-$. The branching fractions of $f_2(1270)$ and $f_4(2050)$ are taken from the PDG [16]. Errors shown are statistical only.

Mode	Area	B.F. (10^{-5})	Significance
$\gamma f_0(980), f_0(980) \rightarrow \pi^+\pi^-$	340^{+140}_{-130}	$1.6^{+0.7}_{-0.6}$	$8.3 \times 10^{-6} (4.3\sigma)$
$\gamma f_2(1270)$	1230 ± 100	10.4 ± 0.8	$< 10^{-45} (> 14\sigma)$
$\gamma f_4(2050)$	85 ± 30	3.6 ± 1.3	$5.2 \times 10^{-3} (2.6\sigma)$
$\gamma f_J(2220), f_J(2220) \rightarrow \pi^+\pi^-$	< 13	$< 6.2 \times 10^{-2}$	-

4.3 Angular Distribution of The Signal

The helicity angle distributions of θ_π and θ_γ are defined and described in the appendix. In this section we first obtain the helicity angular distributions of the $f_0(980)$, $f_2(980)$, and $f_4(2050)$ and then fit them to the predictions of the helicity formalism.

In practical terms, obtaining the helicity angle distribution of a particular resonance from data consists of two steps. First, we choose an invariant mass interval around the resonance peak to select events from the resonance and obtain a helicity angular distribution which has both signal and background events. Second, we subtract the contribution to the helicity angular distribution of the background events in the chosen mass interval to obtain what we want; the helicity angle distribution of the resonance.

Choosing the mass interval is not a trivial thing. If its too wide there will be too much background, and if its to narrow there will not be enough signal. To choose the optimum mass interval we need to know how much signal and background we are selecting. Therefore, the two steps described in the previous paragraph are related. How we deal with this is revealed in the next two sections.

4.3.1 Optimum Mass Interval

As described above, the first step in obtaining the helicity angle distribution for a resonance is choosing an invariant mass interval to select events from such a resonance. A standard 1Γ (which corresponds to 1.6σ for a spin 0 Breit-Wigner) cut around the mean mass of the resonance can be chosen as a “standard” interval. We could proceed this way, but in our case because of the large subtractions involved when obtaining the angular distribution, a considerable increase statistical significance of each bin in the helicity angular distribution can be achieved by choosing the mass interval carefully (see the last column of Table 4-2).

Let’s consider for example the $f_0(980)$ angular distribution. We begin with the $\Upsilon(1S)$ and the $\Upsilon(4S)$ efficiency corrected distributions. Before the continuum subtraction each bin in the $f_0(980)$ angular distribution has contributions from the high end mass tail of the ρ and the low mass tail of the $f_2(1270)$. In order to get the final angular distribution, both of these contributions are taken away by first doing a continuum subtraction using the scale factor $\alpha = 0.404$, and then

by subtracting the $f_2(1270)$ distribution outside the mass interval scaled by an appropriate scale factor β equal to the ratio of $f_2(1270)$ inside the mass interval and outside of it ¹. After all this, the contributions to the bins in the final angular distribution are,

$$N_{f_0(980)} = n_{f_0(980)} + n_{\rho(\Upsilon(1S))} + n_{f_2(1270)} - \alpha n_{\rho(\Upsilon(4S))} - \beta n'_{f_2(1270)} \approx n_{f_0(980)} \quad (4.1)$$

where $n_{f_0(980)}(n_{f_2(1270)})$ is the number of $f_0(980)(f_2(1270))$ obtained by integrating the fitted spin-dependent, relativistic Breit-Wigner function inside the mass interval, $n_{\rho(\Upsilon(1S))}(n_{\rho(\Upsilon(4S))})$ is the number of ρ 's inside the mass interval from continuum events at the $\Upsilon(1S)(\Upsilon(4S))$ energy, and $n'_{f_2(1270)}$ is the number of $f_2(1270)$ outside the mass interval being used to subtract the contribution of $f_2(1270)$ to the $f_0(980)$ angular distribution. Following this last definition, $\beta = n_{f_2(1270)}/n'_{f_2(1270)}$.

Each of these terms has an associated error. Assuming that $\Delta n = \sqrt{n}$, that the efficiency correction has infinite statistics, and ignoring the errors on the continuum scale factor α , the overall error is,

$$\Delta N_{f_0(980)} = \sqrt{n_{f_0(980)} + (\alpha + \alpha^2)n_{\rho(\Upsilon(4S))} + (2 + \beta + \beta^2)n_{f_2(1270)}}$$

We arrive to the conclusion that the mass interval $(\bar{m} - \Delta m, \bar{m} + \Delta m)$ which produces the helicity angle distribution with smallest relative bin-errors is the one

¹ Strictly speaking this is correct only to first order. The $f_2(1270)$ distribution itself has a small contamination from $f_0(980)$ and $f_4(2050)$. This effect, which we call cross-contamination, is ignored in Equation 4.1. Later, in section 4.2.2, we will show how to eliminate this small cross-contamination using all the resonances. The difference in how we actually get the helicity distributions and Equation 4.1 has an insignificant effect when calculating the optimal mass interval

that maximizes,

$$F_{f_0(980)}(\bar{m}, \Delta m) = \frac{n_{f_0(980)}}{\sqrt{n_{f_0(980)} + (\alpha + \alpha^2)n_{\rho(\Upsilon(4S))} + (2 + \beta + \beta^2)n_{f_2(1270)}}}. \quad (4.2)$$

The plot of $F_{f_0(980)}(\bar{m}, \Delta m)$ is shown in figure 4–6.

This same technique can be applied to the $f_2(1270)$ and $f_4(2050)$ resonances.

Results are shown in Table 4–2.

Table 4-2: Mean masses, widths in GeV/c² and inverse of the average bin relative error (F) from background subtractions for the angular distribution of different resonances. Standard mean masses and widths, corresponding to 1Γ , are taken from the fit in Figure 4-3, and are labeled with the subscript “s”, while those that maximize F are labeled with the subscript “m”. The last column shows the factor by which the effective statistics increase.

Resonance	$(\bar{m}_s, \Delta m_s)$	$F(m_s, \Delta m_s)$	$(\bar{m}_m, \Delta m_m)$	$F(m_m, \Delta m_m)$	$\frac{F^2(\bar{m}_m, \Delta m_m)}{F^2(m_s, \Delta m_s)}$
$f_0(980)$	(0.970, 0.070)	5.7	(0.985, 0.060)	6.0	1.11
$f_2(1270)$	(1.270, 0.120)	18.3	(1.590, 0.420)	20.6	1.27
$f_4(2050)$	(2.120, 0.220)	3.2	(2.240, 0.250)	3.4	1.13

4.3.2 Background Subtraction

The continuum subtraction of the helicity angle distribution is defined in Section 2.1. The subtraction of the tails from other resonances requires a closer look. Let us call the continuum subtracted helicity angle distribution of the events in the $f_0(980)$, $f_2(1270)$, and $f_4(2050)$ mass intervals $c_{f_0(980)}$, $c_{f_2(1270)}$, and $c_{f_4(2050)}$ respectively. Let us call the helicity angle distribution of the events that come exclusively from the resonance we are trying to select in the same mass intervals (that is, the true helicity angle distribution of the resonance) $t_{f_0(980)}$, $t_{f_2(1270)}$, and $t_{f_4(2050)}$ respectively. The continuum subtracted helicity angle distribution of a resonance is being contaminated by the tails of the other resonances. Keeping this in mind we write ²

$$\begin{cases} c_{f_0(980)} = t_{f_0(980)} + \beta t_{f_2(1270)} \\ c_{f_2(1270)} = t_{f_2(1270)} + \gamma t_{f_0(980)} + \delta t_{f_4(2050)} \\ c_{f_4(2050)} = t_{f_4(2050)} + \epsilon t_{f_2(1270)} \end{cases} \quad (4.3)$$

Where the small numbers β , γ , δ , and ϵ are the ratios of the number of events from a resonance in the mass interval where the contamination is taking place to the number of events from the same resonance in the mass interval used to select it. Using the $(m_m, \Delta m_m)$ values in Table 4-2 and the fit in Figure 4-3 we obtain $\beta = 8.5 \times 10^{-3}$, $\gamma = 6.0 \times 10^{-2}$, $\delta = 9.7 \times 10^{-2}$, and $\epsilon = 0.13$.

To obtain the background subtracted helicity angular distributions we simply invert the system of equations expressed in Equation 4.3. The solution can be

² Here the cross contamination between the $f_0(980)$ and the $f_4(2050)$ is ignored. There is no mathematical problem in including these contamination terms, but the system of equations would be more complicated than it needs to be since this type of cross contamination is negligible.

conveniently expressed as,

$$\begin{cases} t_{f_2(1270)} = \frac{1}{1-\beta\gamma-\delta\epsilon}(c_{f_0(1270)} - \gamma c_{f_0(980)} - \delta c_{f_4(2050)}) \\ t_{f_0(980)} = c_{f_0(980)} - \beta t_{f_2(1270)} \\ t_{f_4(2050)} = c_{f_0(2050)} - \epsilon t_{f_2(1270)} \end{cases} \quad (4.4)$$

As a check, if we ignore the second order terms the previous solution becomes,

$$\begin{cases} t_{f_2(1270)} = c_{f_0(1270)} - \gamma c_{f_0(980)} - \delta c_{f_4(2050)} \\ t_{f_0(980)} = c_{f_0(980)} - \beta c_{f_2(1270)} \\ t_{f_4(2050)} = c_{f_0(2050)} - \epsilon c_{f_2(1270)} \end{cases}$$

which is indeed is the solution when cross-contamination is ignored.

4.3.3 Statistical Fit of the Helicity Angular Distributions

For each resonance, we fit the data to the simultaneous $\cos\theta_\gamma$ and $\cos\theta_\pi$ helicity angle distribution obtained from data using Equation 4.4 to the helicity formalism prediction, Equations 23-27, projected on each angle and folded in opposite directions around their symmetry axis in order to show both distributions on the same plot. The corresponding J value of the best fit for each resonance, shown in Figures 4–8 through 4–10, is defined as the J assignment (J_a). We obtain $J_a = 1$ for the $f_0(980)$ which is inconsistent with the known spin of the $f_0(980)$ which is $J = 0$. For the $f_2(1270)$ and the $f_4(2050)$ we obtain $J_a = 2$ and $J_a = 4$ respectively, which is consistent with their known spins.

To have an idea of how well the angular distribution determines J among the hypotheses $J = 0, 1, 2, 3, 4$, we do a statistical fit for each hypothesis and assign each one a probability proportional to $e^{-(\chi^2 + d.o.f.)/2}$ where *d.o.f.* are the degrees of freedom in the fit. The resulting normalized probability distributions give an idea of the assigned J significance and are shown in Figure 4–11. In particular,

this figure shows that the $J_a = 1$ for the $f_0(980)$ inconsistency can be due to a statistical fluctuation.

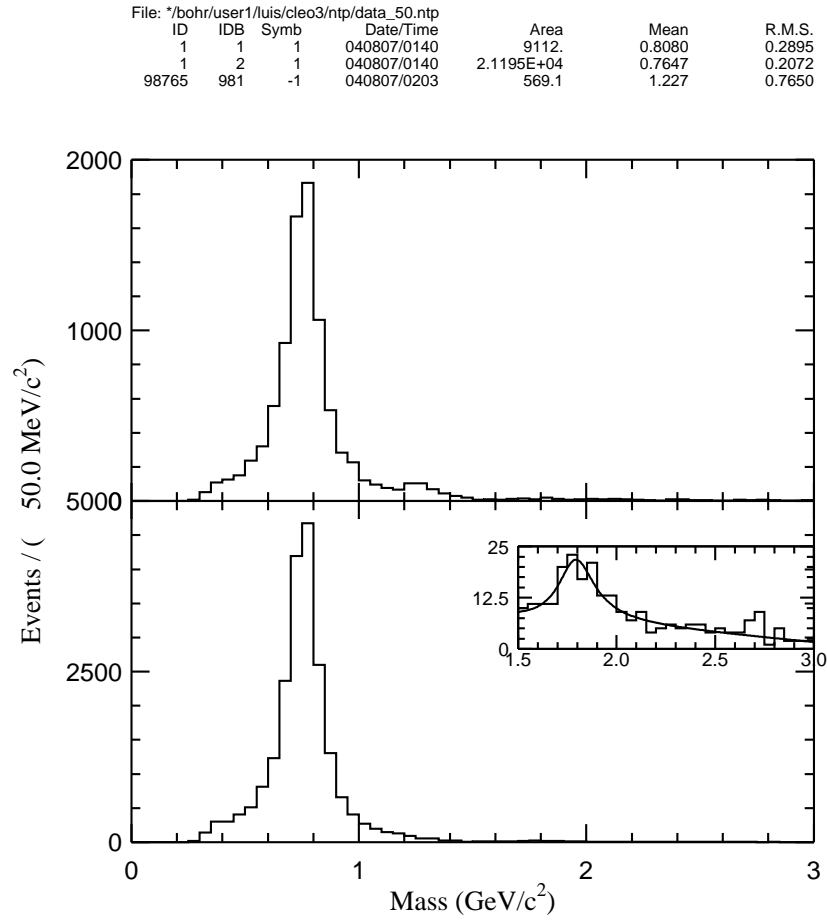


Figure 4–2: Invariant mass of $\pi^+\pi^-$ for 1S (top) and 4S (bottom) data. For the 4S data we show a blow-up of the mass region $1.5 - 3 \text{ GeV}/c^2$ where the ρ^* can be seen.

MINUIT χ^2 Fit to Plot		9&3	
U1S→Gamma h h. masspi axis			
File: Generated internally		22-JUL-2004 11:51	
Plot Area Total/Fit	1544.1 / 1542.1	Fit Status 3	
Func Area Total/Fit	1359.7 / 1359.7	E.D.M. 8.848E-06	
$\chi^2 = 44.7$ for 54 - 8 d.o.f.,		C.L.= 52.7%	
Errors	Parabolic	Minos	
Function 1: f_0			
MOD	435.70	± 165.4	- 167.0 + 177.3
MEAN	0.96672	± 1.5714E-02	- 1.2374E-02 + 1.8160E-02
WIDTH	7.05219E-02	± 3.2912E-02	- 4.3455E-02 + 4.4879E-02
* SPIN	0.00000E+00	± 0.0000E+00	- 0.0000E+00 + 0.0000E+00
* THRESHOLD	0.28000	± 0.0000E+00	- 0.0000E+00 + 0.0000E+00
Function 2: f_2			
MOD	998.59	± 77.96	- 78.12 + 77.92
MEAN	1.2678	± 7.5905E-03	- 7.1319E-03 + 8.0978E-03
WIDTH	0.12353	± 1.4273E-02	- 1.3459E-02 + 1.5382E-02
* SPIN	2.0000	± 0.0000E+00	- 0.0000E+00 + 0.0000E+00
* THRESHOLD	0.28000	± 0.0000E+00	- 0.0000E+00 + 0.0000E+00
Function 3: f_4			
MOD	104.37	± 38.84	- 38.76 + 38.91
MEAN	2.1191	± 5.4515E-02	- 5.8898E-02 + 4.9096E-02
* WIDTH	0.22200	± 0.0000E+00	- 0.0000E+00 + 0.0000E+00
* SPIN	4.0000	± 0.0000E+00	- 0.0000E+00 + 0.0000E+00
* THRESHOLD	0.28000	± 0.0000E+00	- 0.0000E+00 + 0.0000E+00

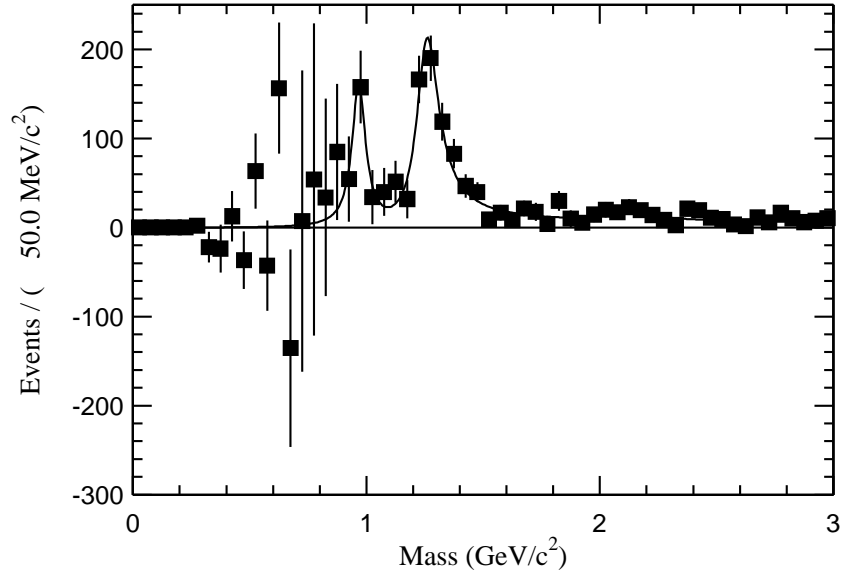


Figure 4–3: Continuum subtracted (as defined in Section 3.2.1) invariant mass of $\pi^+\pi^-$ from $\Upsilon(1S) \rightarrow \gamma\pi^+\pi^-$.

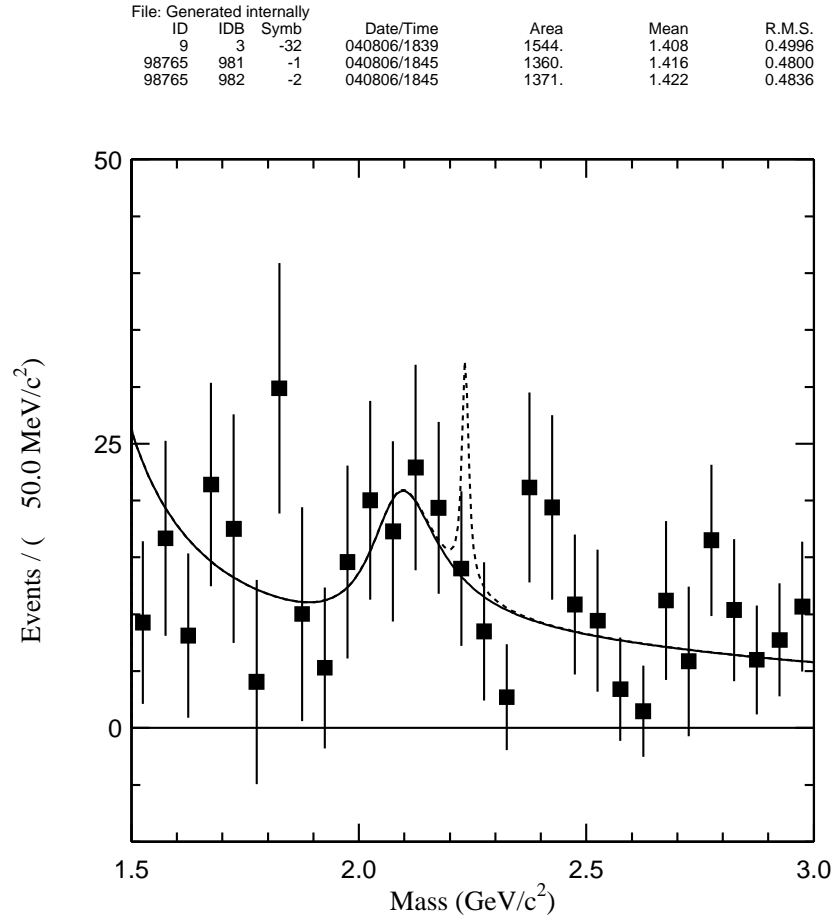


Figure 4–4: Blow up of the invariant mass of $\pi^+\pi^-$ in the $f_4(2050)$ mass region, including the upper limit on the $f_J(2220)$ shown as a dashed line.

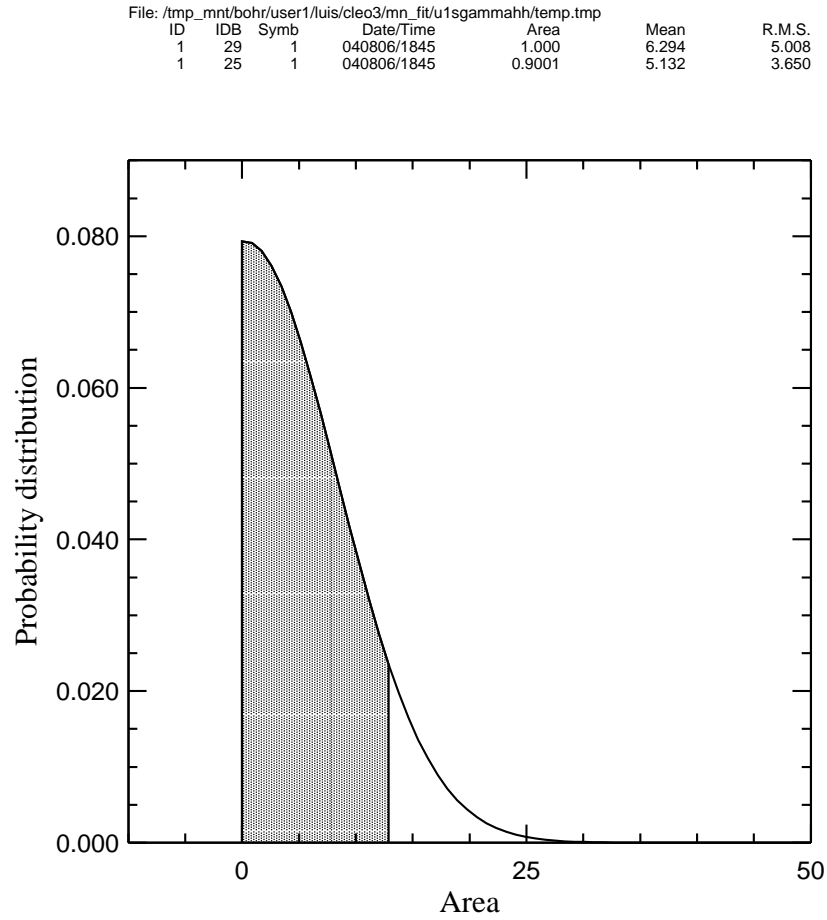


Figure 4–5: Normalized probability distribution for different $f_J(2220) \rightarrow \pi^+\pi^-$ signal areas. The shaded area spans 90% of the probability.

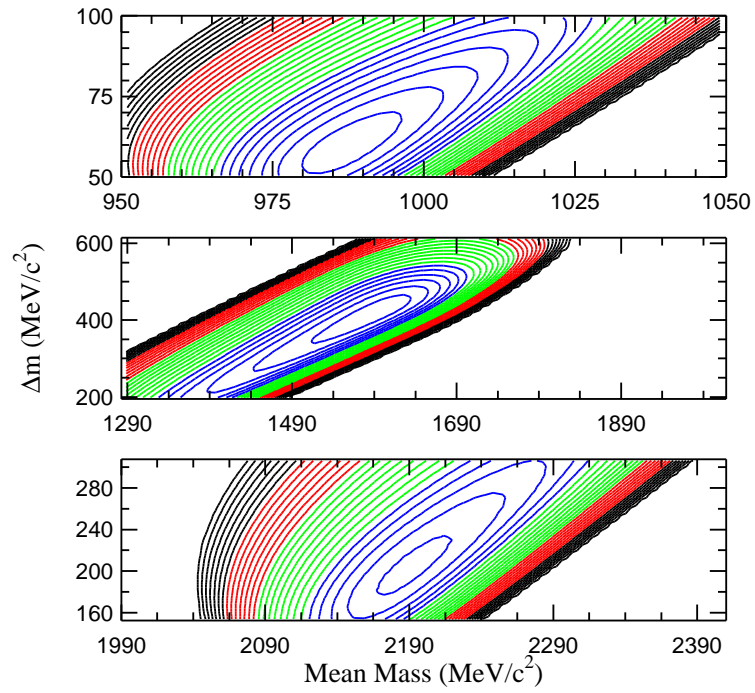


Figure 4–6: Contour plot of the inverse of the average relative bin-error from background subtractions in the $f_0(980)$ (top), $f_2(1270)$ (middle), and $f_4(2050)$ (bottom) angular distribution.

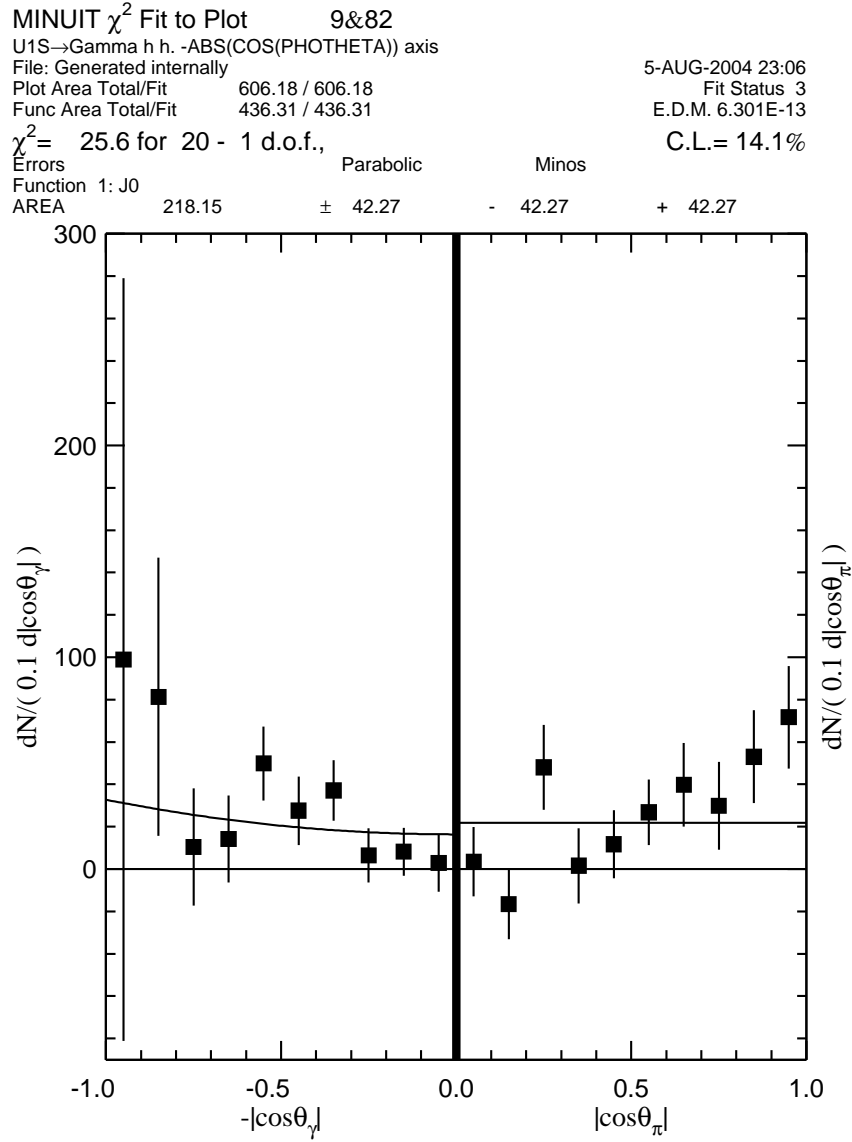


Figure 4–7: Angular distribution for the excess events in the $f_0(980)$ mass region. The fit corresponds to $J = 0$.

MINUIT χ^2 Fit to Plot 9&82
 U1S→Gamma h h. -ABS(COS(PHOTHETA)) axis
 File: Generated internally
 Plot Area Total/Fit 606.18 / 606.18
 Func Area Total/Fit 478.89 / 478.89
 5-AUG-2004 23:06
 Fit Status 3
 E.D.M. 1.115E-05
 $\chi^2 = 15.2$ for 20 - 2 d.o.f., C.L.= 65.1%
 Errors Parabolic Minos
 Function 1: J1
 AREA 239.45 \pm 39.31 - 39.33 + 39.29
 Θ 1.32483E-03 \pm 0.3852 - 0.0000E+00 + 0.3537

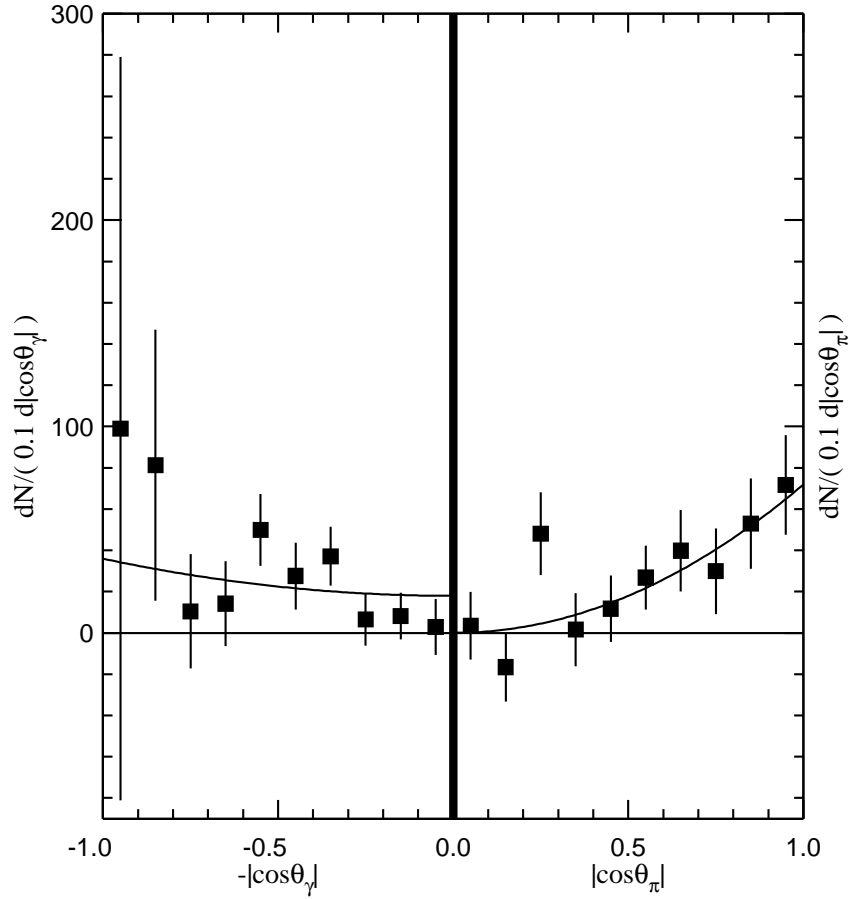


Figure 4–8: Angular distribution for the excess events in the $f_0(980)$ mass region. The fit corresponds to $J = 1$.

MINUIT χ^2 Fit to Plot 9&72
 U1S→Gamma h h. -ABS(COS(PHOTHETA)) axis
 File: Generated internally
 Plot Area Total/Fit 1673.4 / 1673.4
 Func Area Total/Fit 1733.8 / 1733.8
 5-AUG-2004 23:06
 Fit Status 3
 E.D.M. 9.701E-06
 $\chi^2 = 27.3$ for 20 - 3 d.o.f., C.L.= 5.4%
 Errors Parabolic Minos
 Function 1: J2
 AREA 866.97 ± 43.10 - 45.85 + 46.07
 Θ 4.25267E-04 $\pm 7.7843E-02$ - 0.0000E+00 + 0.1238
 Φ 0.29838 ± 0.1098 - 0.1478 + 9.9862E-02

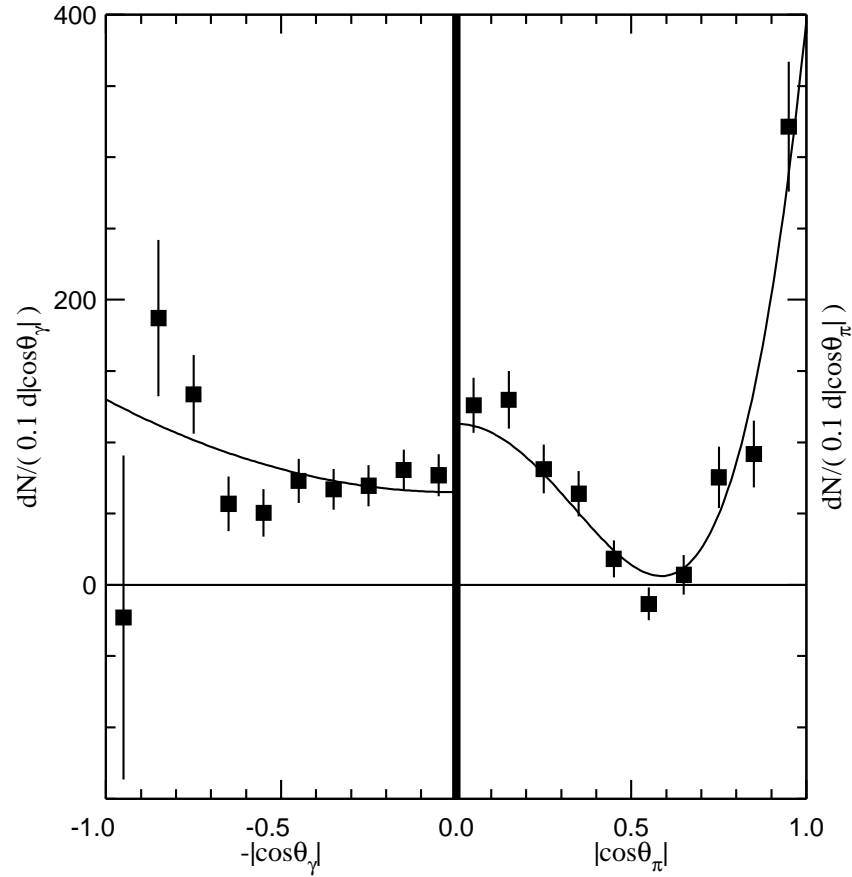


Figure 4–9: Angular distribution for the excess events in the $f_2(1270)$ mass region. The fit corresponds to $J = 2$.

MINUIT χ^2 Fit to Plot 9&92
 U1S→Gamma h h. -ABS(COS(PHOTHETA)) axis
 File: Generated internally
 Plot Area Total/Fit 159.93 / 159.93
 Func Area Total/Fit 127.08 / 127.08
 5-AUG-2004 23:06
 Fit Status 3
 E.D.M. 5.300E-07
 $\chi^2 = 19.6$ for 20 - 3 d.o.f., C.L.= 29.3%
 Errors Parabolic Minos
 Function 1: J4
 AREA 63.528 ± 1.408 - 14.91 + 0.0000E+00
 Θ 1.5697 $\pm 5.8174E-02$ - 0.3398 + 0.0000E+00
 Φ 0.16919 ± 0.6887 - 0.0000E+00 + 0.0000E+00

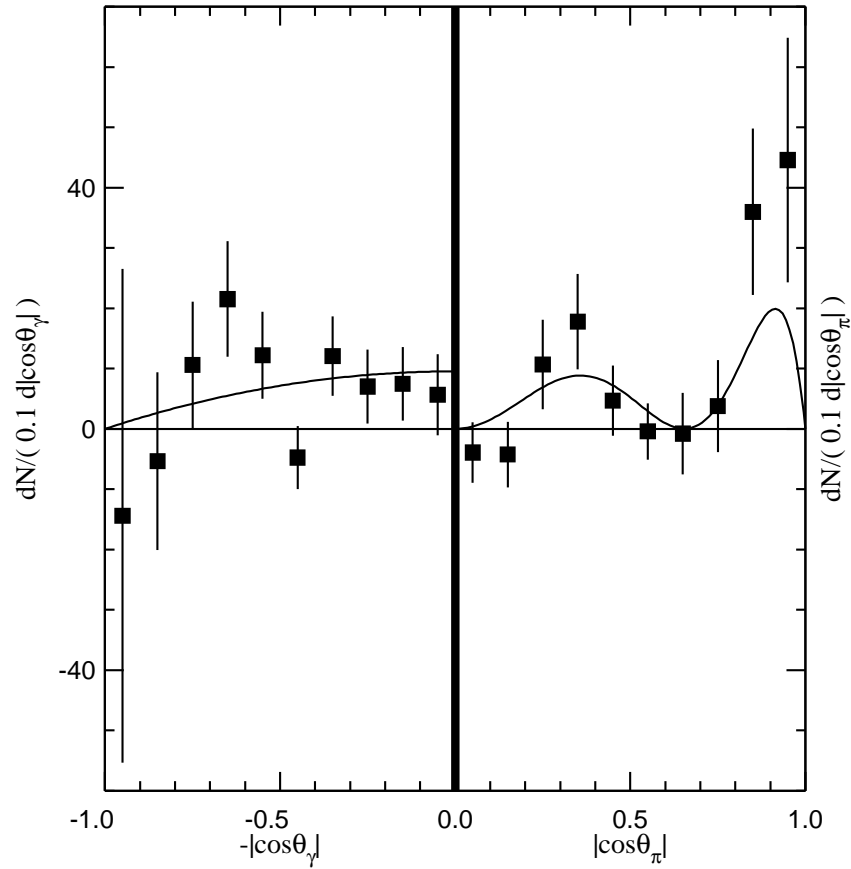


Figure 4–10: Angular distribution for the excess events in the $f_4(2250)$ mass region. The fit corresponds to $J = 4$.

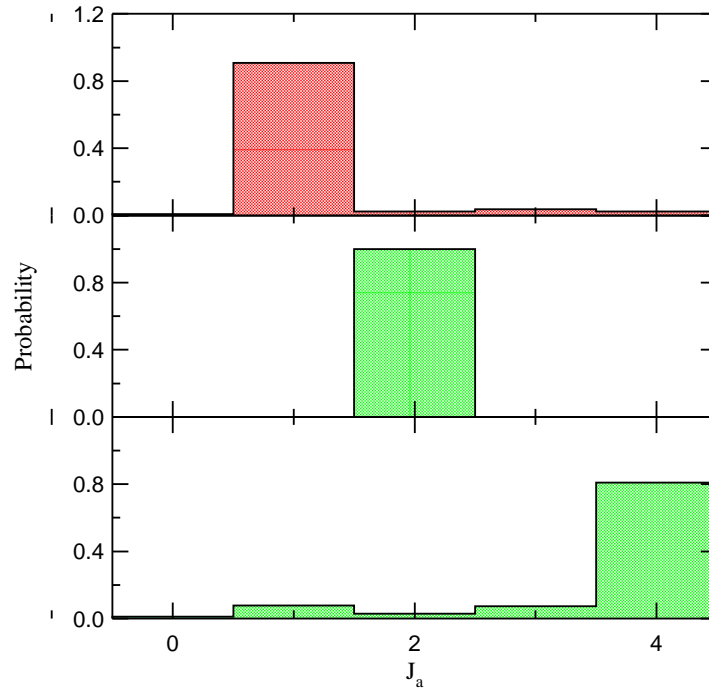


Figure 4–11: J_a probability distribution for resonances in the $f_0(980)$ (top), $f_2(1270)$ (middle), and $f_4(2050)$ (bottom) invariant mass region when only the hypotheses $J_a = 0, 1, 2, 3, 4$ are considered.

CHAPTER 5

EXCLUSIVE RADIATIVE DECAY $\Upsilon(1S) \rightarrow \gamma K^+ K^-$

In figure 5–1 the $K^+ K^-$ invariant mass plot is shown for both resonance and continuum running. This figure also has an inset showing the $\sigma_{dE/dX}(K)$ for both tracks for events in the $1.1 - 3 \text{ GeV}/c^2$ region. This inset indicates that most of the events in this mass region have indeed two kaons and that the amount of ρ reflection is small. Furthermore, when the $\pi^+ \pi^-$ invariant mass is plotted for these events only 40 out of 700 can be fit under a ρ peak (this fit is what we use to calculate the pion faking kaon rate in Table 3–6).

Figure 5–2 shows our fit to the $K^+ K^-$ invariant mass continuum subtracted plot as defined in Section 3.2.1 with the most likely statistical fit overlayed (which is described in the next section). The number of events near the ϕ region ($1.01 - 1.03 \text{ GeV}/c^2$) left after the continuum subtraction is 50 ± 70 .

5.1 Statistical Fit of the Invariant Mass Distribution

The results of this section are summarized in Table 5–1.

From the measurement of the previous section we expect a small contribution (≈ 50 events assuming no interference) from $f_2(1270) \rightarrow K^+ K^-$. We do find some evidence for $f_2(1270) \rightarrow K^+ K^-$ events (110 ± 40) in the fit. We also find strong evidence for the resonance $f'_2(1525)$ and weak evidence for the $f_0(1710)$ resonance. The $f_2(1270)$, and $f_0(1710)$ are fitted with their widths fixed to their PDG values[16] because they have large errors if allowed to float. The rest of the resonances parameters are consistent with their PDG values[16], which are $m_{f'_2(1525)} = 1525 \pm 5 \text{ MeV}/c^2$, $\Gamma_{f'_2(1525)} = 76 \pm 10 \text{ MeV}/c^2$, $m_{f_0(1710)} = 1715 \pm 6 \text{ MeV}/c^2$, and $\Gamma_{f_0(1710)} = 125 \pm 10 \text{ MeV}/c^2$. We also observe an excess of events in the $2 - 3 \text{ GeV}/c^2$ region which we can't attribute to any known resonances.

Significances of the signals of the identified resonances in the fit are calculated as described in the previous section. The $\Upsilon(1S) \rightarrow \gamma f_J(2220)$, $f_J(2220) \rightarrow K^+ K^-$ upper limit is also calculated using multiple fits, except that this time the events under the $f_J(2220)$ are of unknown origin, so we use a first order polynomial allowed to float. The significance of the excess of events in the $2 - 3 \text{ GeV}/c^2$ invariant mass region is calculated assuming a normal distribution; we simply add up the number of events in each bin along with its error. Results are shown in Table 5–1.

Table 5-1: Results for $\Upsilon(1S) \rightarrow \gamma K^+ K^-$

Mode	Area	Branching Fraction (10^{-5})	Significance
$\gamma f_2(1270)$	110 ± 40	23 ± 8	$5.4 \times 10^{-4}(3.3\sigma)$
$\gamma f_2'(1525)$	360^{+80}_{-70}	$3.9^{+0.9}_{-0.7}$	$< 10^{-45}(> 14\sigma)$
$\gamma f_0(1710), f_0(1710) \rightarrow K^+ K^-$	75 ± 30	0.35 ± 0.14	$7.5 \times 10^{-4}(3.2\sigma)$
$\gamma K^+ K^-(2 - 3 \text{ GeV}/c^2)$	220 ± 20	1.03 ± 0.12	8.8σ
$\gamma f_J(2220), f_J(2220) \rightarrow K^+ K^-$	< 10	$< 5 \times 10^{-2}$	-

5.2 Angular Distribution of The Signal

In this section we adapt the ideas presented in Section 3.4.3 to the $\Upsilon(1S) \rightarrow \gamma K^+ K^-$ situation.

The derived statistical errors from the signal and background subtractions can be used to calculate the mass interval which best represents the helicity angular distribution. The inverse of the expected average relative bin error as a function of the mass interval is shown in Figure 5-5, and the mass interval that maximizes it are tabulated in Table 5-2.

Table 5–2: Mean masses, widths in_{mass} and inverse of the average bin relative error (F) from background subtractions for the angular distribution of different resonances. Standard mean masses and widths, corresponding to 1Γ , are taken from the fit in Figure 5–2, and are labeled with the subscript “s”, while those that maximize F are labeled with the subscript “m”. The last column shows the factor by which the effective statistics increase.

Resonance	$(\bar{m}_s, \Delta m_s)$	$F(m_s, \Delta m_s)$	$(\bar{m}_m, \Delta m_m)$	$F(m_m, \Delta m_m)$	$\frac{F^2(m_m, \Delta m_m)}{F^2(m_s, \Delta m_s)}$
$f_2(1270)$	(1.276, 0.185)	3.5	(1.300, 0.100)	4.1	1.37
$f'_2(1525)$	(1.540, 0.085)	9.6	(1.565, 0.100)	9.8	1.04
$f_0(1710)$	(1.760, 0.125)	3.1	(1.780, 0.095)	3.3	1.13

The tails from the resonances contribute to the continuum subtracted helicity distributions,

$$\begin{cases} c_{f_2(1270)} = t_{f_2(1270)} + \beta t_{f'_2(1525)} \\ c_{f'_2(1525)} = t_{f'_2(1525)} + \gamma t_{f_2(1270)} + \delta t_{f_0(1710)} \\ c_{f_0(1710)} = t_{f_0(1710)} + \epsilon t_{f'_2(1525)} \end{cases} \quad (5.1)$$

Where again the small numbers β , γ , δ , and ϵ are the ratios of the number of events from a resonance in the mass interval where the contamination is taking place to the number of events from the same resonance in the mass interval used to select it. Using the $(m_m, \Delta m_m)$ values in Table 5–2 and the fit in Figure 5–2 we obtain $\beta = 1.3 \times 10^{-2}$, $\gamma = 0.14$, $\delta = 0.11$, and $\epsilon = 0.19$.

The background subtracted helicity angular distributions are,

$$\begin{cases} t_{f'_2(1525)} = \frac{1}{1-\beta\gamma-\delta\epsilon}(c_{f'_2(1525)} - \gamma c_{f_2(1270)} - \delta c_{f_0(1710)}) \\ t_{f_2(1270)} = c_{f_2(1270)} - \beta t_{f'_2(1525)} \\ t_{f_0(1710)} = c_{f_0(1710)} - \epsilon t_{f'_2(1525)} \end{cases} \quad (5.2)$$

The the best fit for each resonance and the excess of events in the 2–3 GeV/c² are shown in Figures 5–6 through 5–9. The best spin assignment for the $f_2(1270)$ is $J_a = 2$, for the $f'_2(1525)$ it is $J_a = 2$, for the it is $f_0(1710)$, and it is $J_a = 1$ for the excess of events in the 2 – 3 GeV/c² mass region. The $J_a = 2$ value for the $f_0(1710)$ is inconsistent with its known spin. Also, examination of the normalized helicity amplitudes for the $f_2(1270)$ reveals that they are inconsistent with those obtained for the $f_2(1270)$ in the $\pi^+\pi^-$ mode.

The assigned J probability distributions are shown in Figure 5–11. They reveal that the inconsistencies in the $f_2(1270)$ and $f_0(1710)$ are not significant and can be attributed to the statistical uncertainty.

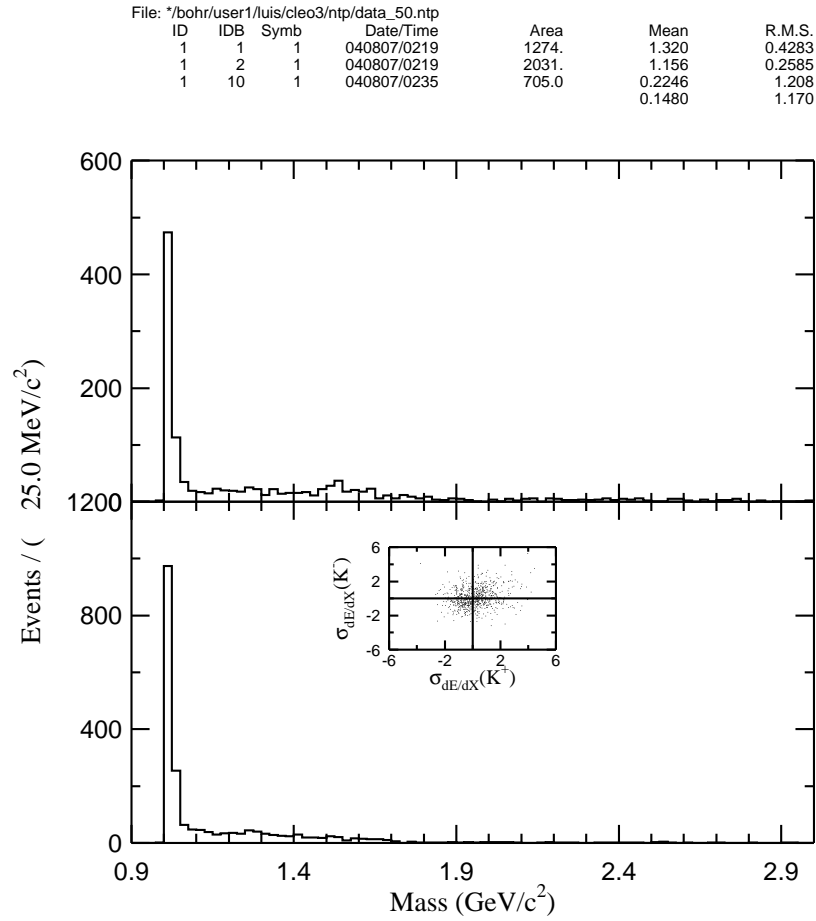
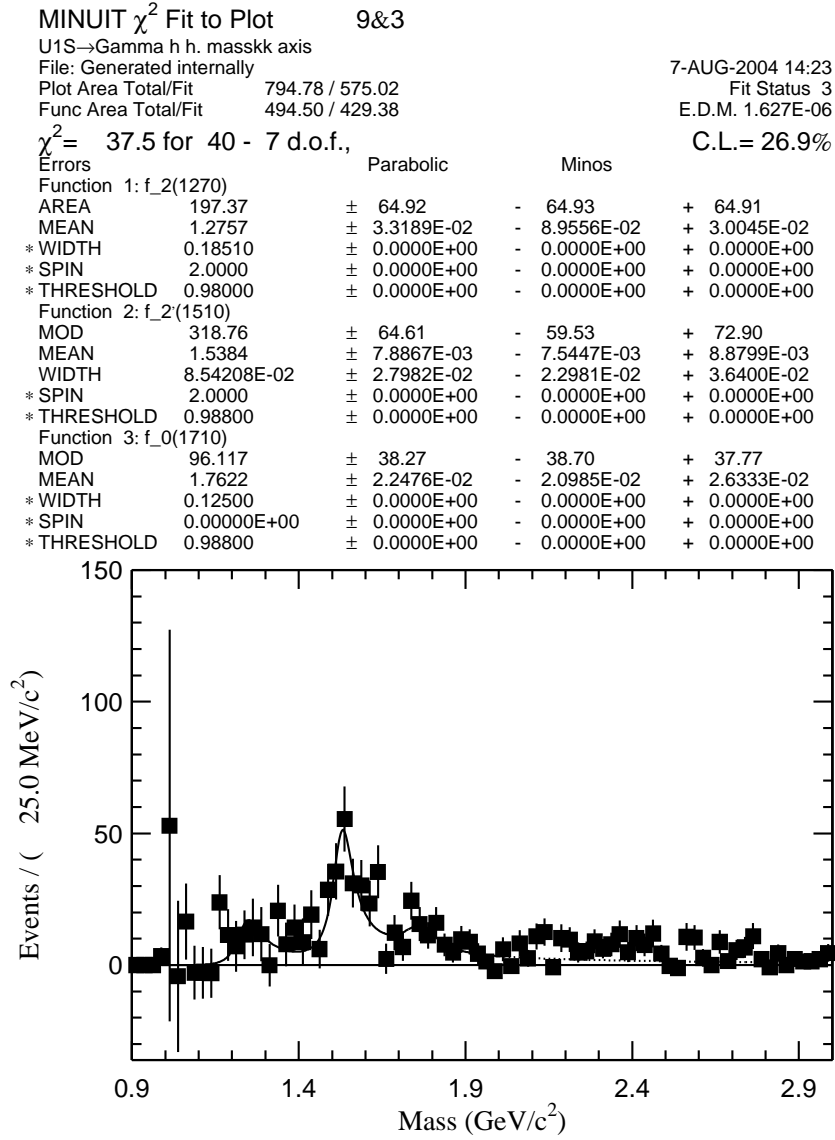


Figure 5–1: Invariant mass of K^+K^- for 1S (top) and 4S (bottom) data. For the 4S data the inset shows the $\sigma_{dE/dX}(K)$ for both tracks for events in the 1.1 – 3 GeV/c² mass region. This inset indicates that most of the events are constant with having two kaons.

Figure 5–2: Continuum subtracted invariant mass of K^+K^- .

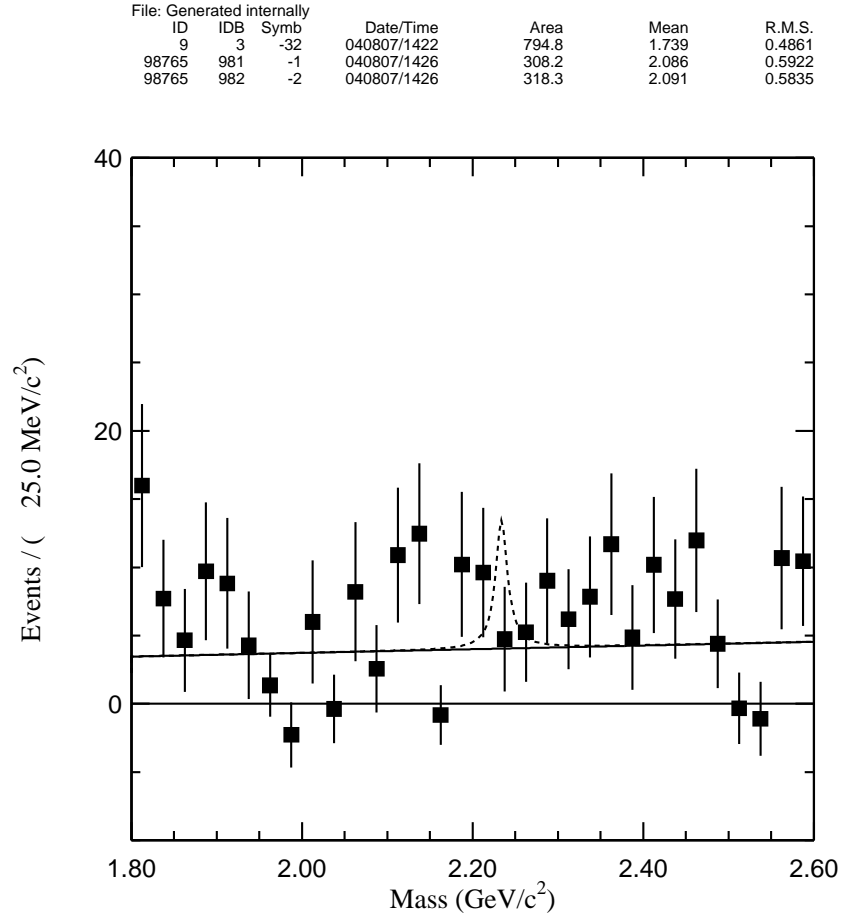


Figure 5–3: Blow up of the $f_J(2220)$ region, with the 90% CL upper limit overlaid. The mass and width are taken to be $m_{f_J(2220)} = 2.234 \text{ GeV}/c^2$ and $\Gamma_{f_J(2220)} = 17 \text{ MeV}/c^2$ as in [17].

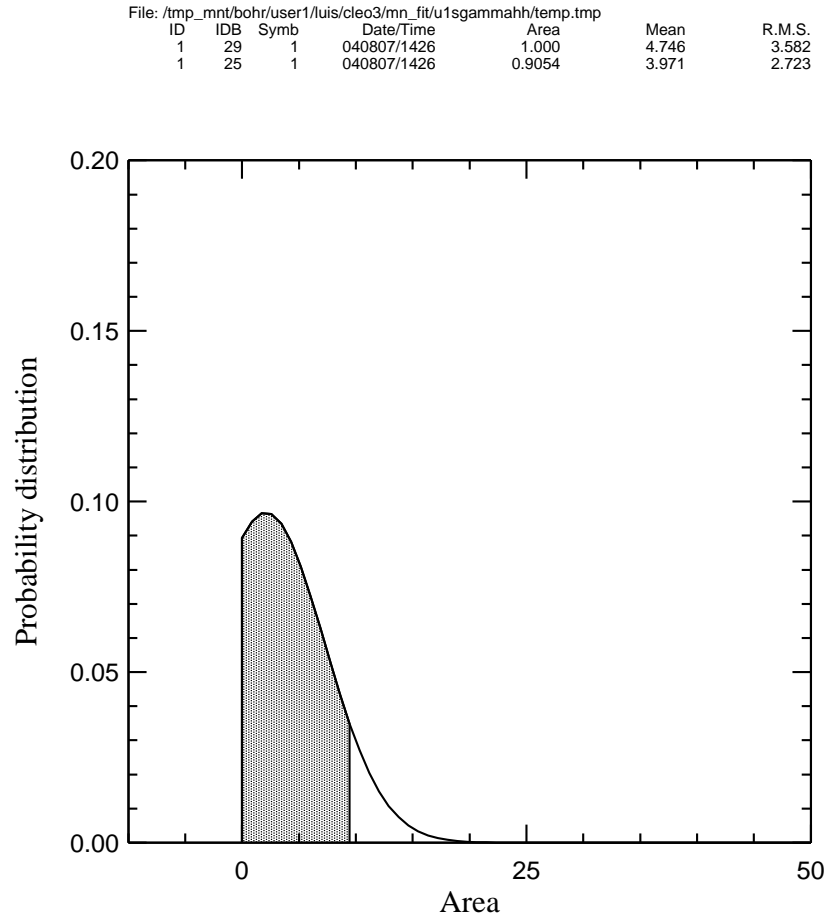


Figure 5–4: Normalized probability distribution for different $f_J(2220) \rightarrow K^+K^-$ signal areas. The shaded area spans 90% of the probability.

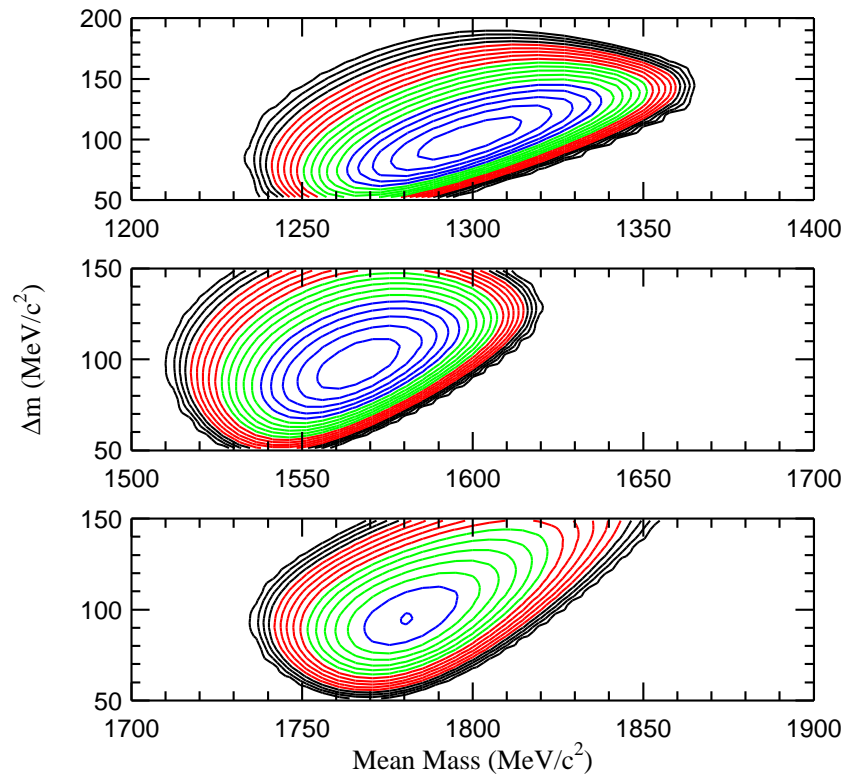


Figure 5–5: Contour plot of the inverse of the average relative bin-error from background subtractions in the $f_2(1270)$ (top), $f_2'(1525)$ (middle), and $f_0(1710)$ (bottom) angular distributions.

MINUIT χ^2 Fit to Plot 9&82
 U1S→Gamma h h. -ABS(COS(PHOTHETA)) axis
 File: Generated internally
 Plot Area Total/Fit 517.49 / 517.49
 Func Area Total/Fit 129.01 / 129.01
 5-AUG-2004 23:16
 Fit Status 3
 E.D.M. 5.475E-05
 $\chi^2 = 17.8$ for 20 - 3 d.o.f., C.L.= 40.4%
 Errors Parabolic Minos
 Function 1: J2
 AREA 64.505 ± 17.78 - 17.78 + 17.78
 Θ 7.95385E-03 ± 1.347 - 0.0000E+00 + 0.5745
 Φ 1.4108 ± 0.4602 - 0.2689 + 0.0000E+00

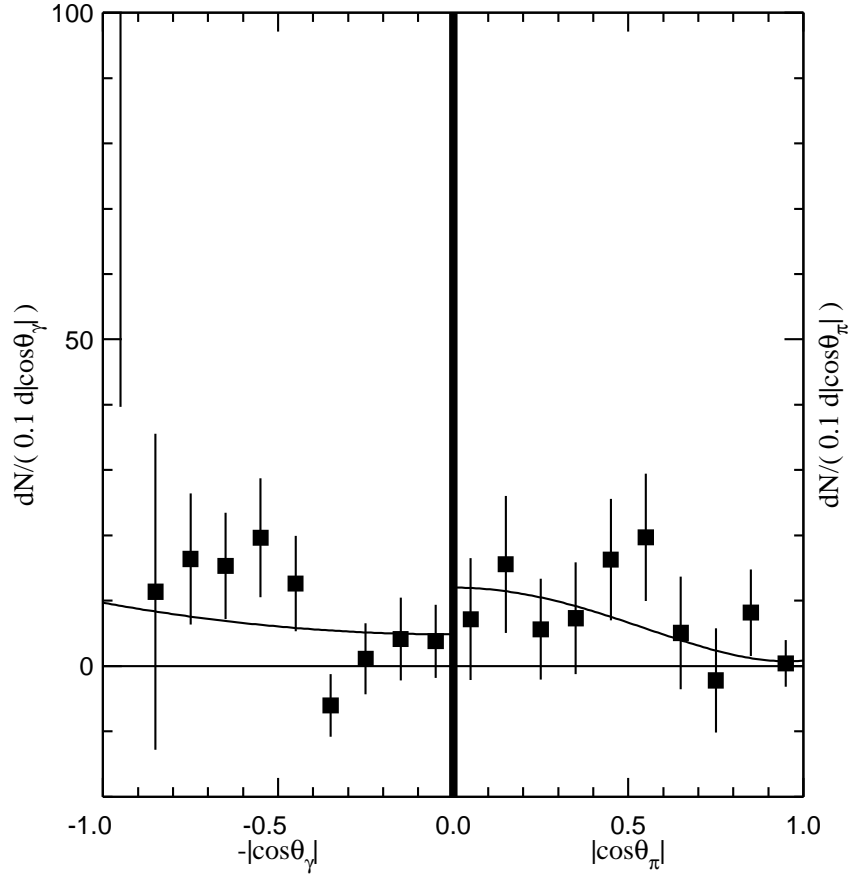


Figure 5–6: Background subtracted K^+K^- angular distribution in the $f_2(1270)$ mass region as defined in the text. The fit corresponds to $J = 2$.

MINUIT χ^2 Fit to Plot 9&72
 U1S→Gamma h h. -ABS(COS(PHOTHETA)) axis
 File: Generated internally
 Plot Area Total/Fit 284.44 / 284.44
 Func Area Total/Fit 367.87 / 367.87
 5-AUG-2004 23:16
 Fit Status 3
 E.D.M. 3.771E-06
 $\chi^2 = 20.9$ for 20 - 3 d.o.f., C.L.= 23.3%
 Errors Parabolic Minos
 Function 1: J2
 AREA 183.94 \pm 18.70 - 19.29 + 19.25
 Θ 6.76443E-04 \pm 0.1885 - 0.0000E+00 + 0.2757
 Φ 0.50343 \pm 0.1298 - 0.1593 + 0.1248

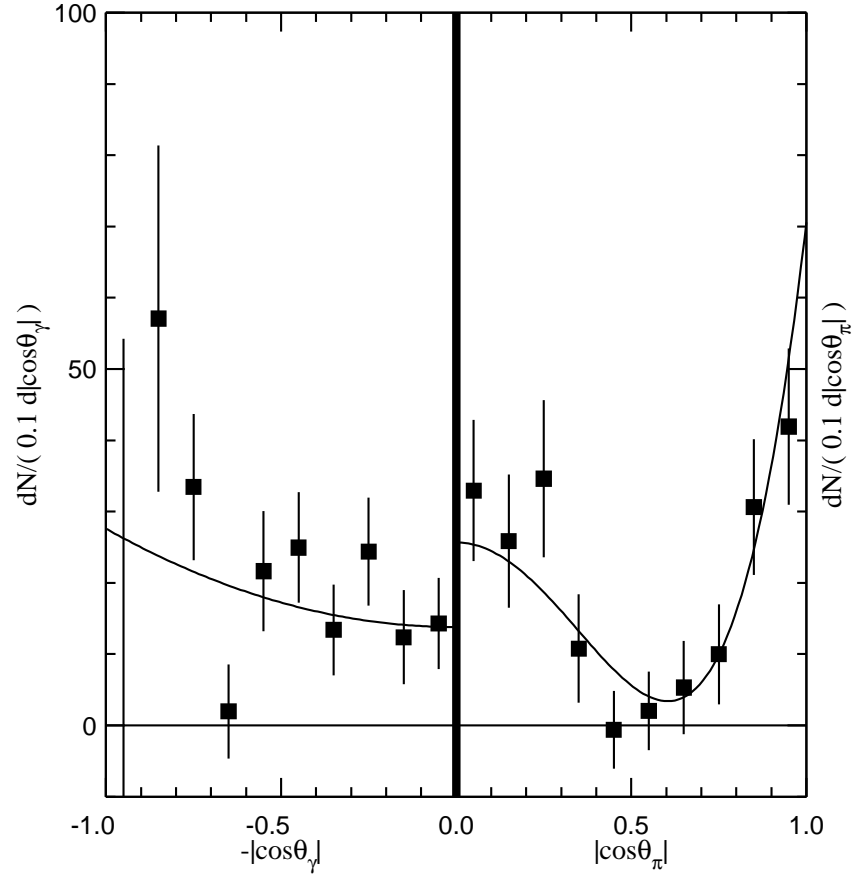


Figure 5-7: Background subtracted K^+K^- angular distribution in the $f_2'(1525)$ mass region as defined in the text. The fit corresponds to $J = 2$.

MINUIT χ^2 Fit to Plot 9&92
 U1S→Gamma h h. -ABS(COS(PHOTHETA)) axis
 File: Generated internally
 Plot Area Total/Fit 129.47 / 129.47
 Func Area Total/Fit 79.031 / 79.031
 5-AUG-2004 23:16
 Fit Status 3
 E.D.M. 1.721E-05
 $\chi^2 = 28.0$ for 20 - 3 d.o.f., C.L.= 4.5%
 Errors Parabolic Minos
 Function 1: J2
 AREA 39.516 ± 10.80 - 10.81 + 10.80
 Θ 2.99860E-04 ± 0.3847 - 0.0000E+00 + 0.4645
 Φ 1.5696 ± 0.2633 - 0.3060 + 0.0000E+00

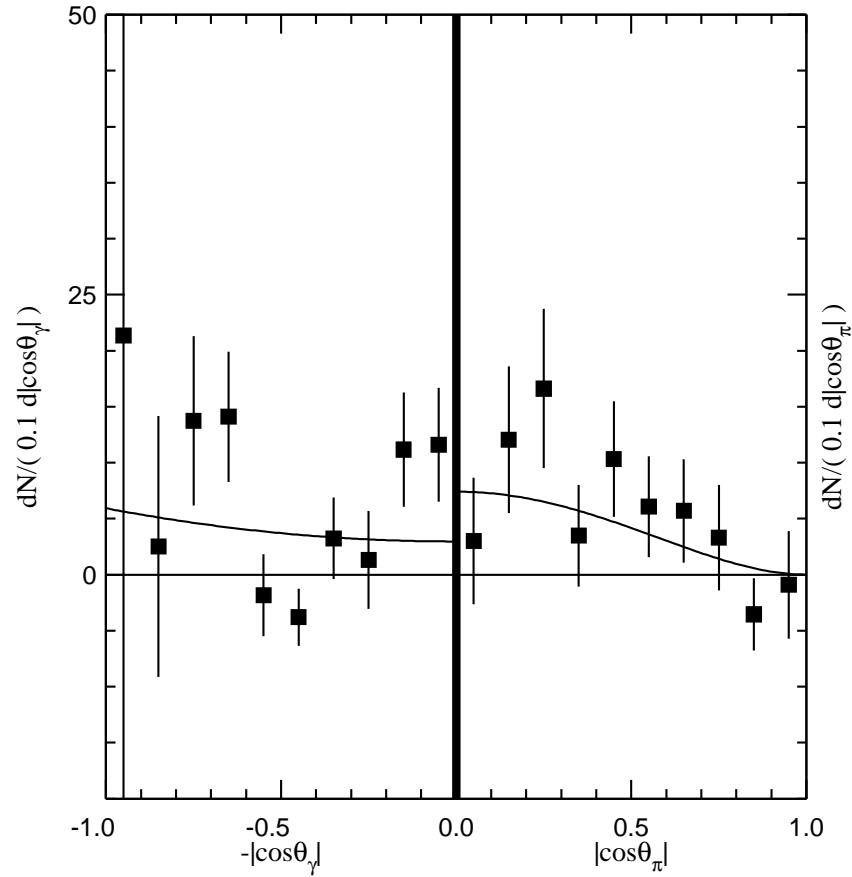


Figure 5–8: Background subtracted K^+K^- angular distribution in the $f_0(1710)$ mass region as defined in the text. The fit corresponds to $J = 2$.

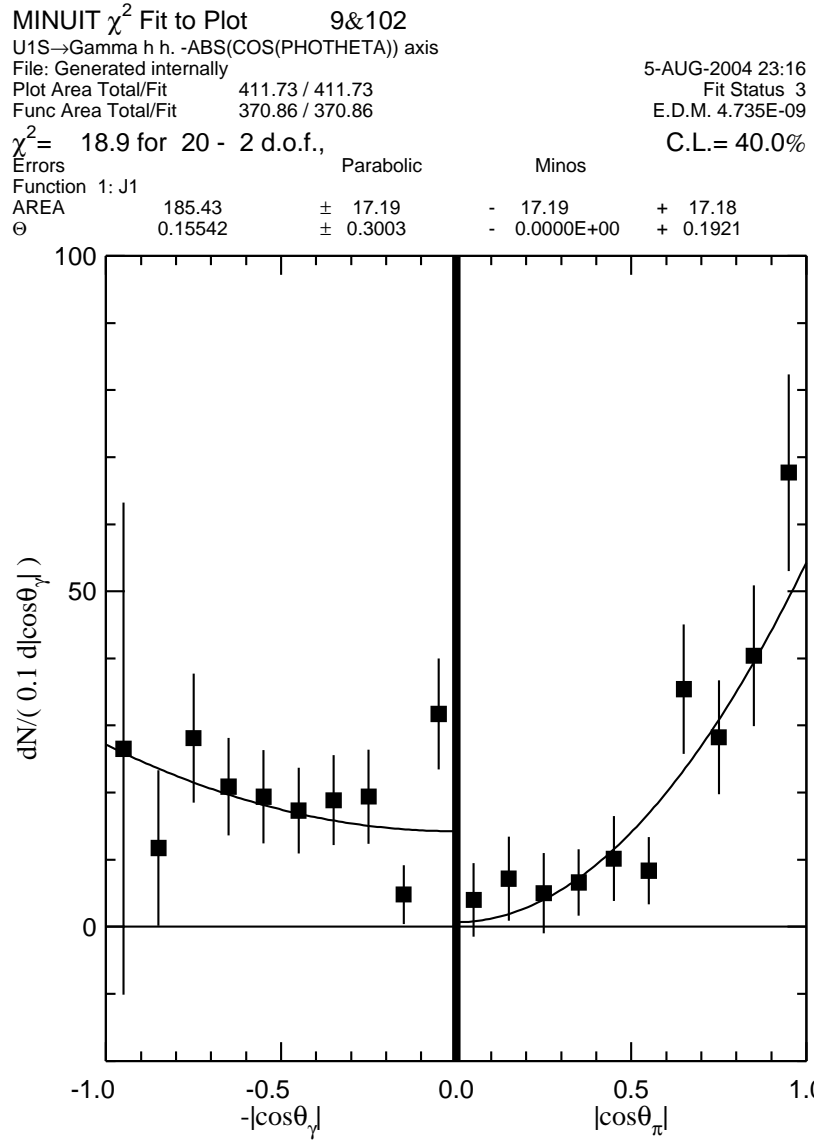


Figure 5-9: K^+K^- angular distribution for events within the 2 – 3 GeV/c^2 .

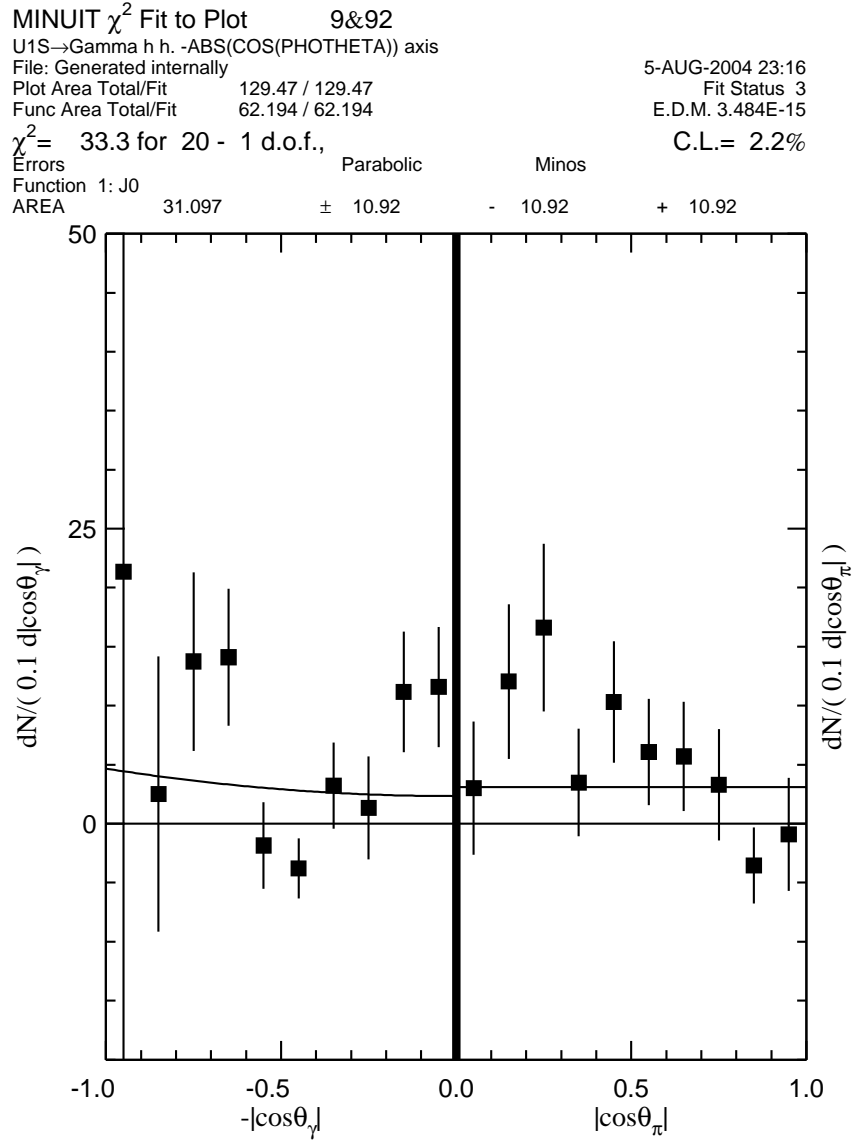


Figure 5–10: Background subtracted K^+K^- angular distribution in the $f_0(1710)$ mass region as defined in the text. The fit corresponds to $J = 0$.

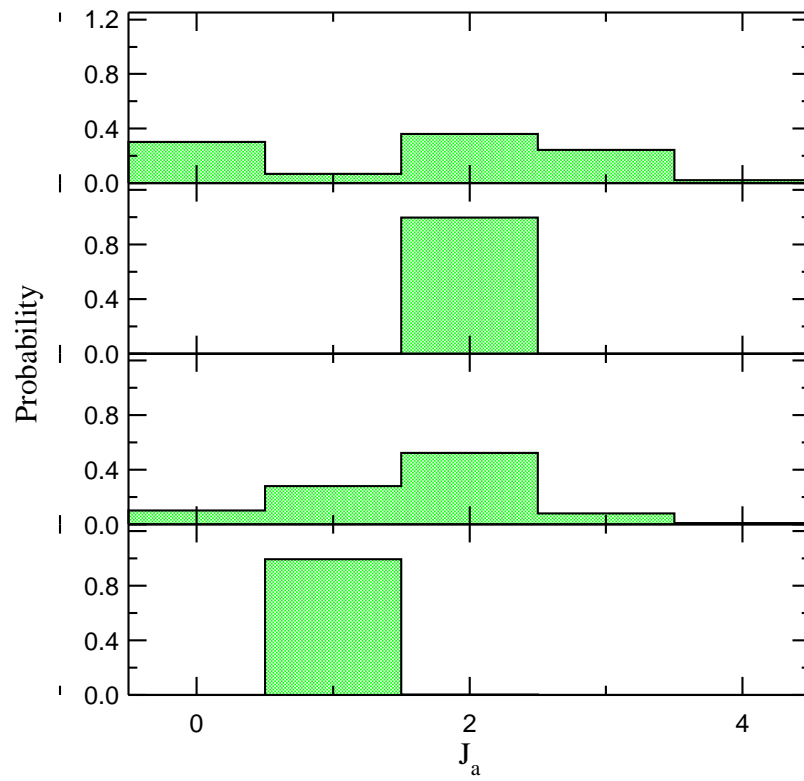


Figure 5–11: J_a probability distribution for resonances in the $f_2(1270)$ (top), $f'_2(1525)$ (middle-top), $f_0(1710)$ (middle-bottom) invariant mass region and the excess of events in the $2 - 3 \text{ GeV}/c^2$ (bottom) region when only the hypotheses $J_a = 0, 1, 2, 3, 4$ are considered.

CHAPTER 6

EXCLUSIVE RADIATIVE DECAY $\Upsilon(1S) \rightarrow \gamma p\bar{p}$

In figure 6–1 the $p\bar{p}$ invariant mass plot is shown for both 1S and 4S data, with an inset showing that most of the events indeed have a proton and an anti-proton and that the ρ and ϕ reflections are small. The enhancement at $3.1 \text{ GeV}/c^2$ in the 4S plot corresponds to the process $e^+e^- \rightarrow \gamma J/\psi$ with $J/\psi \rightarrow p\bar{p}$. This enhancement is not as pronounced in the 1S plot because the 1S data only has 32.4% of the luminosity of the 4S data. The number of events in the J/ψ invariant mass region after continuum subtraction is 6 ± 3 and is consistent with 0.

Figure 6–2 shows the continuum subtracted invariant $p\bar{p}$ mass distribution (as defined in Section 3.2.1) with a 90% confidence level upper limit for $f_J(2220)$ overlaid. A direct fit to the $f_J(2220)$ yields 12 ± 5 events.

There is an excess of events in the continuum subtracted invariant mass plot. We measure this excess and the upper limit of $e^+e^- \rightarrow \gamma f_J(2220)$, $f_J(2220) \rightarrow p\bar{p}$ the same way we measured the excess of events inside $2 \text{ GeV}/c^2 < m(K^+K^-) < 3 \text{ GeV}/c^2$ region and the $f_J(2220)$ upper limit in Section 5.1. Results are shown in Table 6–1.

The $p\bar{p}$ angular distribution for the mass range $2 \text{ GeV}/c^2 < m(p\bar{p}) < 3 \text{ GeV}/c^2$ is shown in Figure 6–4 with the most likely J assignment, $J_a = 1$, fit overlaid. The probability distribution for J_a is shown in Figure 6–5.

Table 6–1: Results for $\Upsilon(1S) \rightarrow \gamma p\bar{p}$.

Mode	Area	B.F. or 90 % U.L. (10^{-5})	Significance
$\gamma p\bar{p}$ ($2 - 3 \text{ GeV}/c^2$)	85 ± 18	0.41 ± 0.08	4.85σ
$\gamma f_J(2220), f_J(2220) \rightarrow p\bar{p}$	< 20	$< 9 \times 10^{-2}$	-

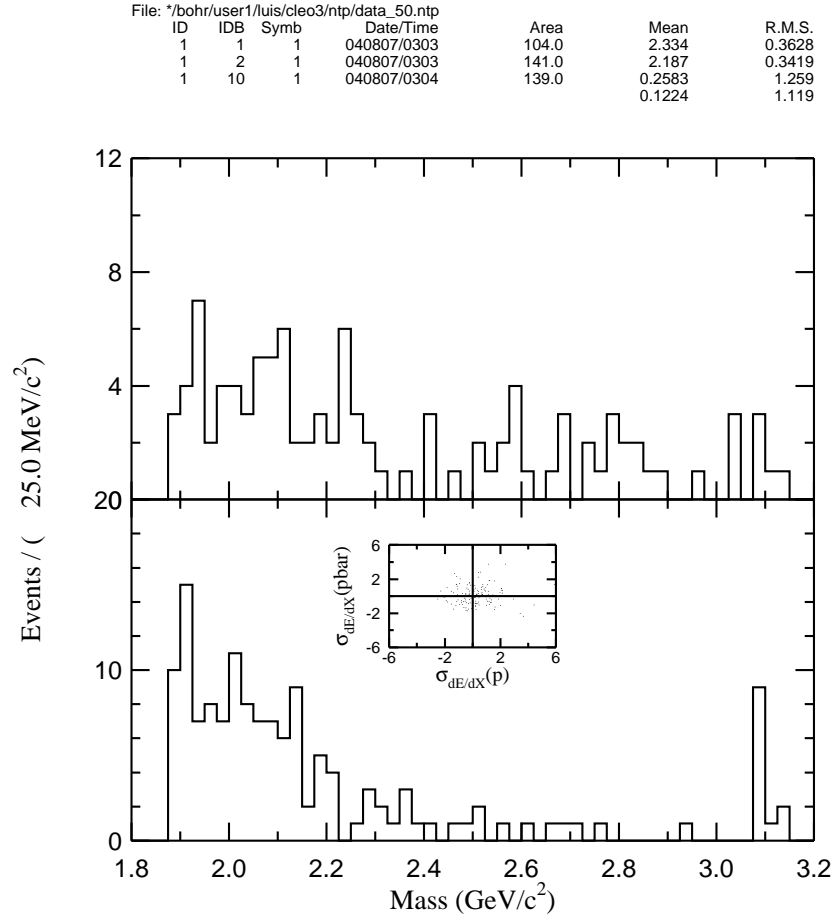


Figure 6–1: Invariant mass of $p\bar{p}$ for 1S (top) and 4S (bottom) running. For the 4S running the inset is consistent with the events having a proton and an anti-proton.

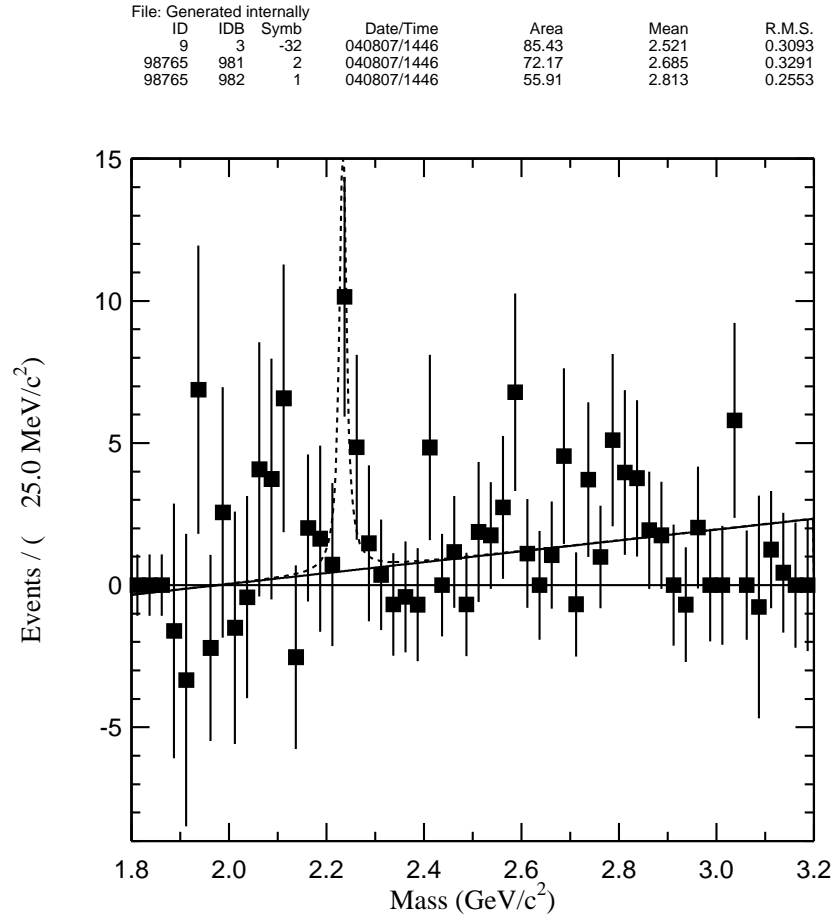


Figure 6–2: Invariant mass of $p\bar{p}$. The plot is continuum subtracted and efficiency corrected. An overlay with the 90% confidence level upper limit for $f_J(2220)$ is shown. The mass and width are taken to be $m_{f_J(2220)} = 2.234 \text{ GeV}/c^2$ and $\Gamma_{f_J(2220)} = 17 \text{ MeV}/c^2$ as in [17].

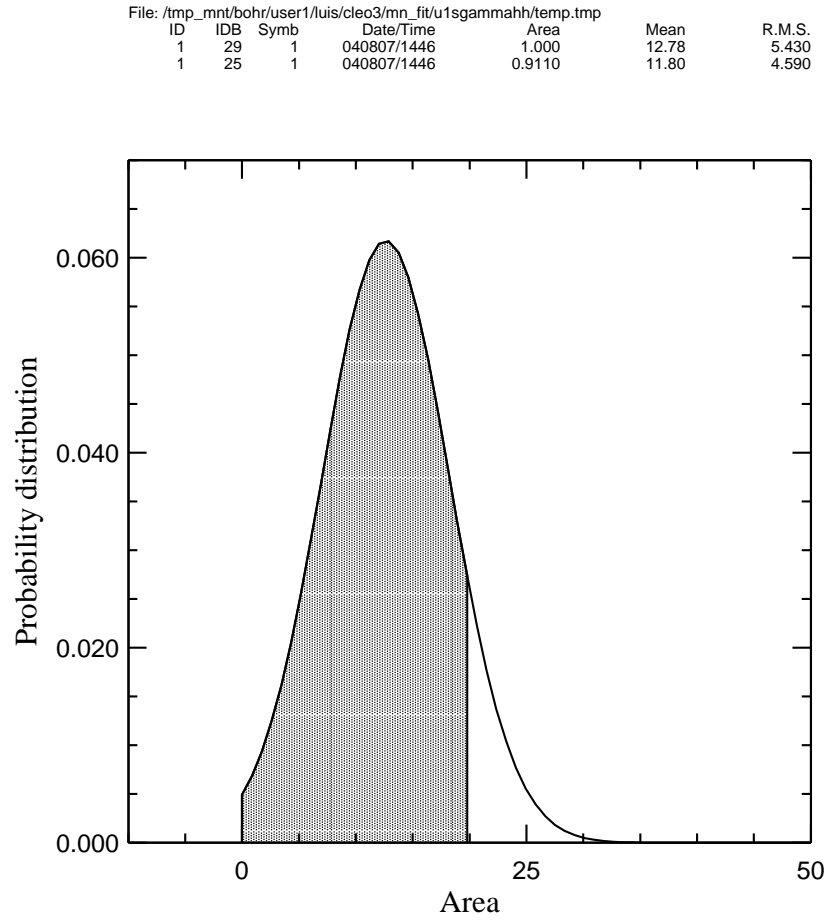


Figure 6–3: Normalized probability distribution for different $f_J(2220) \rightarrow p\bar{p}$ signal areas. The shaded area spans 90% of the probability.

MINUIT χ^2 Fit to Plot 9&22
 U1S→Gamma h h. -ABS(COS(PHOTHETA)) axis
 File: Generated internally 2-AUG-2004 18:12
 Plot Area Total/Fit 256.69 / 256.69 Fit Status 3
 Func Area Total/Fit 134.57 / 134.57 E.D.M. 1.845E-05
 $\chi^2 = 19.5$ for 20 - 2 d.o.f., C.L.= 36.4%
 Errors Parabolic Minos
 Function 1: J1
 AREA 67.287 \pm 10.91 - 10.93 + 10.88
 Θ 1.20611E-03 \pm 0.4148 - 0.0000E+00 + 0.3544

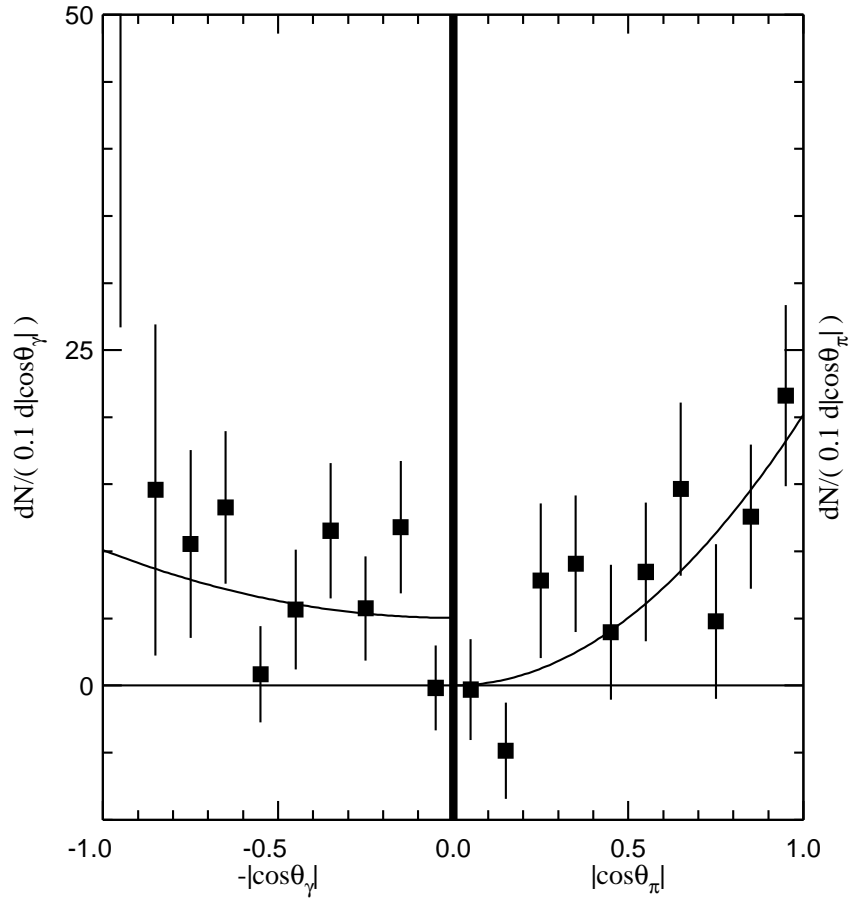


Figure 6–4: $p\bar{p}$ angular distribution for the excess of events in the mass range $2 \text{ GeV}/c^2 < m(p\bar{p}) < 3 \text{ GeV}/c^2$.

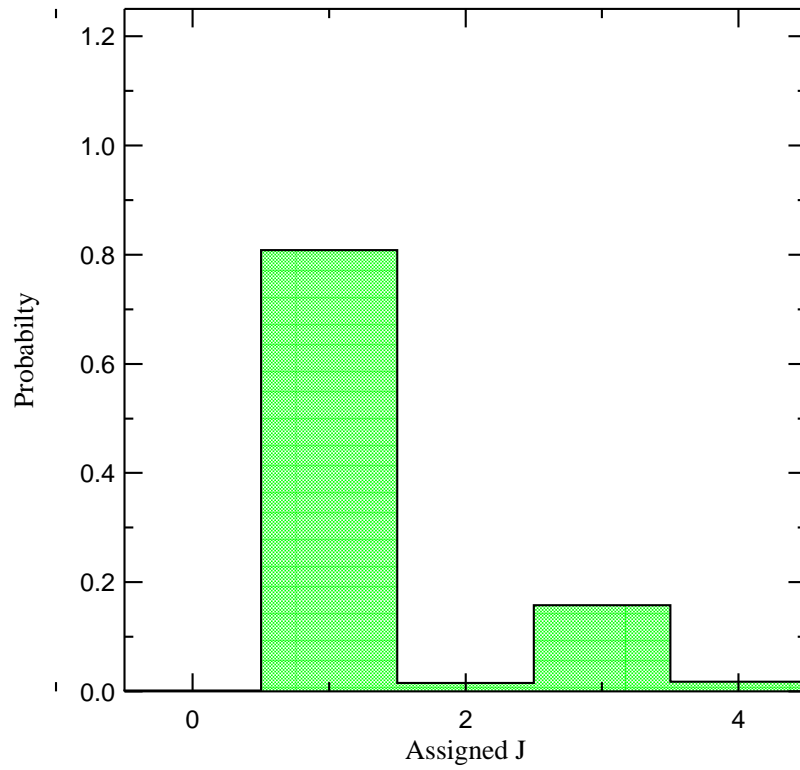


Figure 6–5: J_a probability distribution for the excess of events in the mass range $2 \text{ GeV}/c^2 < m(p\bar{p}) < 3 \text{ GeV}/c^2$ when only the hypotheses $J_a = 0, 1, 2, 3, 4$ are considered.

CHAPTER 7

SYSTEMATIC UNCERTAINTIES

Systematic uncertainties are any sources of experimental uncertainty other than the statistical ones. Limits on the accuracy of our detector simulation and any physical processes that interferes with the experimental measurement are typical examples of systematic uncertainties. These uncertainties need to be identified, quantified, and if possible, corrected.

7.1 Cuts

From now on we report individual cut efficiencies relative to the events that survive all the other cuts.

According to our MC, most of the skim cuts, except for the hardGam requirement, are nearly 100% efficient. Therefore, such cuts should not be a source of systematic uncertainty. The only skim cut worth taking a closer look at is the hardGam cut, which is about 93% efficient in MC. Measuring this efficiency in our data is not possible because events not classified as hardGam are not in the data to begin with. Closer examination of our MC reveals that that most of the 7% inefficiency in hardGam comes from the eOverP1 cut (4%), some from the Sh2 cut (2%), and the rest (1%) from the other cuts present in hardGam. We can measure the efficiency of eOverP1 in data by looking at the eOverP2 distribution of data tracks from ρ and ϕ decay. We are satisfied by this check on the MC modeling (see Tables 7-1 and 7-2), and we won't measure how well MC models the rest of the hardGam cuts, which are 97% efficient in MC.

To quantify the quality in the MC modeling of our analysis cuts in the π and K modes we use the ρ and ϕ signals present in our data¹. In this case the process is straightforward. We measure the ρ and ϕ signal signals in data and MC over a floating background function with all cuts in place, and with all in place cuts except the one under consideration. From these numbers we calculate the effective efficiency of the cut. The differences between data and MC are taken as the systematic errors which are added in quadrature. Results are shown in Tables. 7-1- 7-2. The 4-momentum cut does not appear because its efficiency is close to 100%.

Cuts	MC eff.	Data eff.	Systematic Error
eOverP2	96.2	96.6	0.4
QED $e^+e^- \rightarrow \gamma e^+e^-$ suppression	93.1	94.2	1.2
QED $\mu^+\mu^- \rightarrow \gamma\mu^+\mu^-$ suppression	75.3	77.7	3.2
Hadron separation	96.9	96.8	-0.1
Overall analysis cut systematic error			± 3

Table 7-1: Efficiencies for $\Upsilon(1S) \rightarrow \gamma\pi^+\pi^-$ for flat signal MC, efficiencies from data (ρ), and the derived systematic error in %. Efficiencies are reported as the number of signal events after all cuts divided by the number of signal events with all cuts except the one under consideration. Statisticall errors are 0.1% or less.

For the proton case we don't have a clean sample with high statistics of $e^+e^- \rightarrow \gamma p\bar{p}$ events in data. By extension we take the systematic error in this mode to be 10%.

7.1.1 Justification of the DPTHMU Cut

The reason we prefer to use $DPTHMU < 5$, instead of the more traditional (see [18]) $DPTHMU < 3$ used in CLEO II, is that, for some unknown reason, our CLEO III MC has too many π tracks with $3 < DPTHMU < 5$.

¹ A study using K_S^0 or Λ signals from hadronic environments would have larger statistics, but is problematic because the large number of tracks and showers artificially decrease the cut efficiency. See [28] Appendix A.3 for an example.

Cuts	MC Eff.	Data Eff.	Systematic Error
eOverP2	98.5	100	1.5
QED $e^+e^- \rightarrow \gamma e^+e^-$ suppression	98.1	99.3	1.3
QED $\mu^+\mu^- \rightarrow \gamma\mu^+\mu^-$ suppression	93.5	96.4	3.1
Hadron separation	88.4	82.2	-7.0
Overall analysis cut systematic error			± 8

Table 7-2: Efficiencies for $\Upsilon(1S) \rightarrow \gamma K^+ K^-$ for flat signal MC, efficiencies from data (ϕ), and the derived systematic error in %. Efficiencies are reported as the number of signal events after all cuts divided by the number of signal events with all cuts except the one under consideration. Statistical errors are 0.1% or less.

To observe this fact we first select a relatively clean sample of pion tracks by requiring the event to have a $\pi^+\pi^-$ invariant mass consistent with the ρ mass, and to pass all our analysis cuts except for the cut on $DPTHMU$ on one track. For such events we plot the rate as a function of momentum, at which the π track whose $DPTHMU$ cut we released has $DPTHMU > 3$ and $DPTHMU > 5$. To increase our statistics we do this procedure twice, once for each track, and average the fake rate. Figure 7-1 shows the results. Clearly the CLEO III MC we are using has some problem modeling the $DPTHMU < 3$ cut.

To keep the systematic error low we choose a cut at $DPTHMU < 5$ ($DPTHMU < 3$ gives a systematic error of about 20%). This does not change the efficiency in data very much, but it increases the efficiency reported by MC, bringing it closer to reality. The increase in μ fakes after loosening the cut is estimated to be low using QED MC (see Figure 7-2).

7.2 Angular Distribution of Signal

The photon and tracks from the process $\Upsilon(1S) \rightarrow \gamma X$ with $X \rightarrow h^+h^-$ have a different angular distribution than that of flat MC. Examples of possible angular distributions are shown in the appendix.

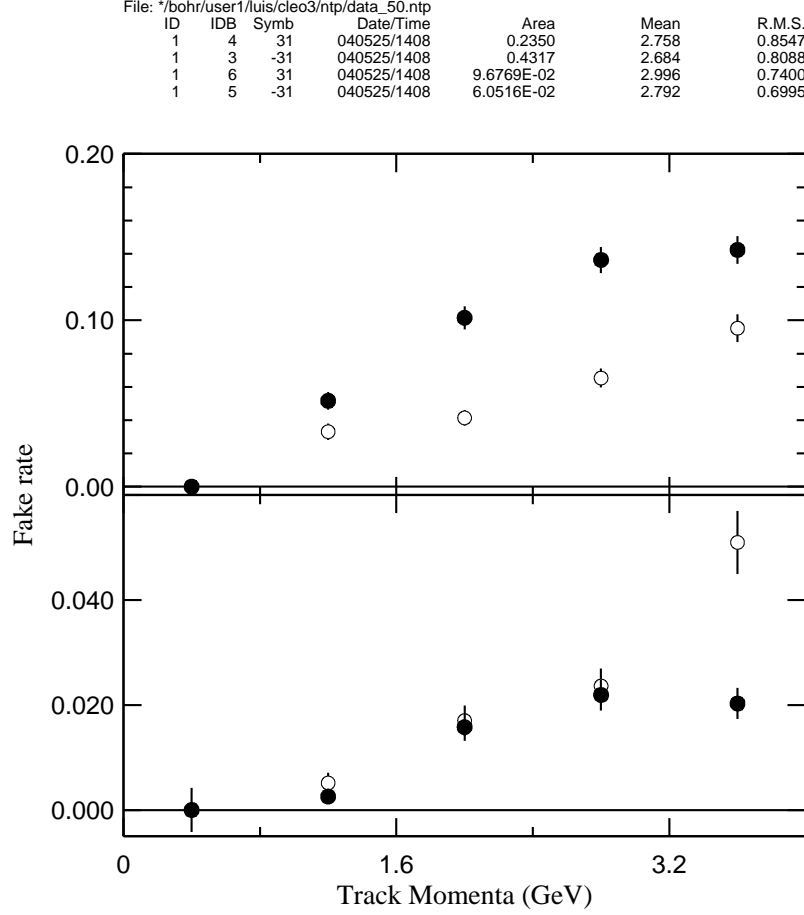


Figure 7–1: Pion faking muon fake rates for a cut on $DPTHMU < 3$ (top) and $DPTHMU < 5$ (bottom). MC is shown as solid circles while ρ from data is shown as hollow circles. Fake rates are reported relative to all events that pass all cuts, except for the $DPTHMU$ cut for one of the tracks.

Figure 7–3 shows the efficiency in flat MC as a function of $\cos\theta_\gamma$ and $\cos\theta_{h^+}$ ². Note that the K and p modes are nearly insensitive to the track angular distribution, while the π mode is more sensitive to θ_{h^+} . This happens because of the stronger muon rejection cut in the π mode.

We measure the systematic effects of flat MC efficiency by convoluting each plot in Figure 7–3 with different possible angular distributions calculated in the

² θ_γ and θ_{h^+} are the helicity angles of the sequential decay, defined in the appendix (see Figure 2).

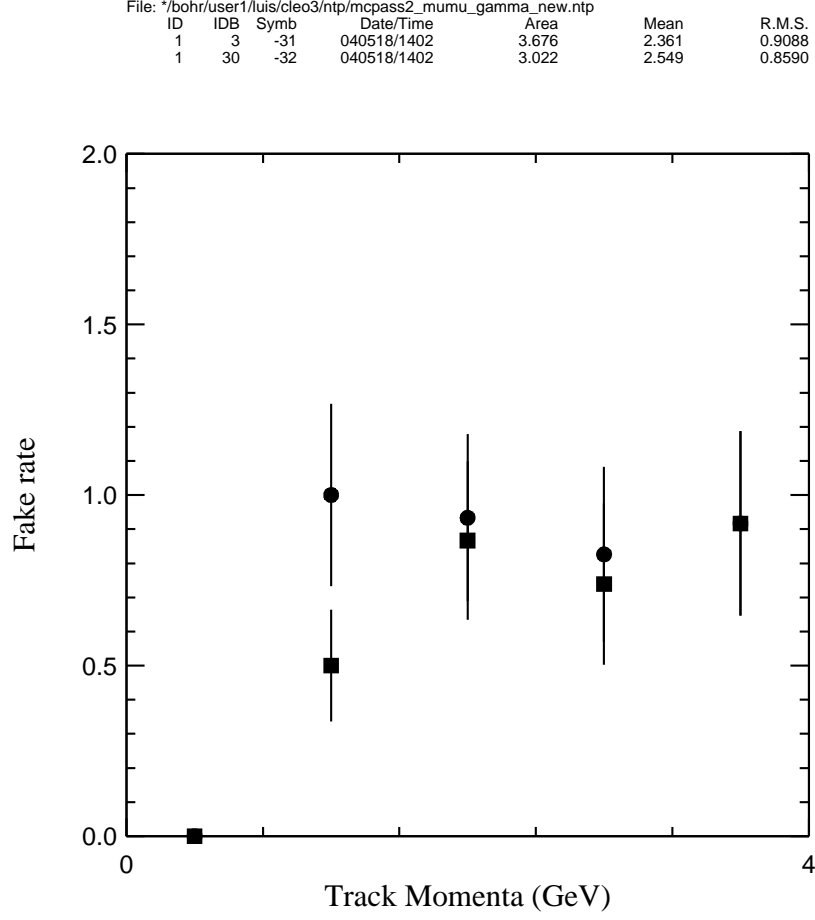


Figure 7–2: Muon faking pion fake rate (in %) for $DPTHMU < 3$ (solid squares) and $DPTHMU < 5$ (solid circles). There is a complete overlap in the last bin.

appendix. Tables 7–3–7–4 show the necessary correction factors relative to flat MC efficiency for decays with definite γ and X helicities λ_γ and λ_X , due to the non-flat photon and hadron distributions. We call these factors $\epsilon_{\lambda_\gamma \lambda_X}^{J_X}(\gamma)$ and $\epsilon_{\lambda_\gamma \lambda_X}^{J_X}(h)$ respectively.

The efficiency of a decay with definite λ_γ , λ_X can be obtained using the flat MC efficiency corrected by a factor $\epsilon_{\lambda_\gamma \lambda_X}^{J_X} = \epsilon_{\lambda_\gamma \lambda_X}^{J_X}(\gamma) \times \epsilon_{\lambda_\gamma \lambda_X}^{J_X}(h)$. In general, the final state is a mixture of all possible λ_γ , λ_X pairs, and the efficiency correction factor is,

$$\epsilon^{J_X} = \cos^2 \Theta \cos^2 \Phi \epsilon_{10}^{J_X} + \sin^2 \Theta \epsilon_{11}^{J_X} + \cos^2 \Theta \sin^2 \Phi \epsilon_{12}^{J_X}. \quad (7.1)$$

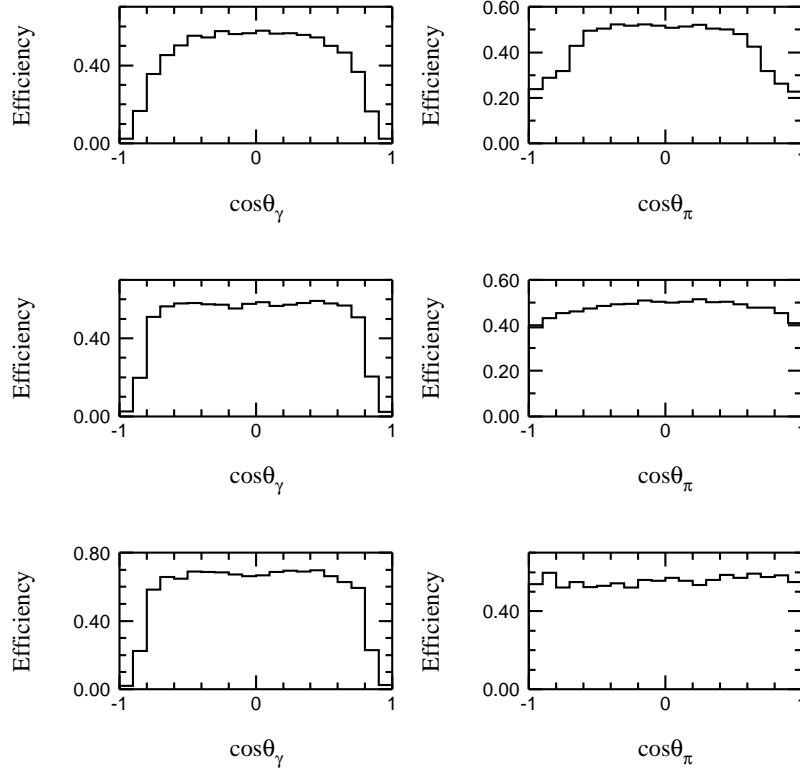


Figure 7-3: Flat MC efficiency as a function of $\cos\theta_\gamma$ (left column) and as a function of $\cos\theta_{h^+}$ (right column). Top row corresponds to the pion mode, middle row to the kaon mode and bottom row to the proton mode.

The fits in Figures 4-8 and 4-10 and 5-6-5-8 measure the pair (Θ, Φ) . These values are summarized in Table 7-5, where they are used to obtain ϵ^{J_X} for each mode.

The pair (Θ, Φ) carry an error which is a source of systematic uncertainty. We calculate this systematic uncertainty by inspecting the differences in efficiency when (Θ, Φ) move away from the value which gives the minimum chi-squared, χ_{min}^2 ,

Mode	a_{10} or a_{12} $\Theta = 0$	a_{11} $\Theta = \frac{\pi}{2}$
π	0.910	1.18
K	0.925	1.15
p	0.922	1.16

Table 7-3: $\epsilon_{\lambda_\gamma \lambda_X}^{J_X}(\gamma)$, efficiency correction with respect to flat MC factors due to the non-flat angular distribution of the photon in $\Upsilon(1S) \rightarrow \gamma X$ for different X spin values (J_X) and γ , X helicities ($\lambda_\gamma, \lambda_X$).

Mode	J_X	a_{10} $\Theta = 0, \Phi = 0$	a_{11} $\Theta = \frac{\pi}{2}$	a_{12} $\Theta = 0, \Phi = \frac{\pi}{2}$
$X \rightarrow \pi^+ \pi^-$	0	1.00	-	-
	1	0.785	1.11	-
	2	0.829	0.934	1.15
	3	0.898	0.853	1.03
	4	0.899	0.863	0.922
$X \rightarrow K^+ K^-$	0	1.00	-	-
	1	0.944	1.03	-
	2	0.950	0.988	1.04
	3	0.957	0.971	1.01
	4	0.965	0.962	0.992

Table 7-4: $\epsilon_{\lambda_\gamma \lambda_X}^{J_X}(h)$, efficiency correction factors with respect to non-flat MC due to the track angular distribution in $\Upsilon(1S) \rightarrow \gamma X$, with $X \rightarrow h^+ h^-$ for different X spin values (J_X) and γ , X helicities ($\lambda_\gamma, \lambda_X$).

under the condition $\chi^2 < \chi_{min}^2 + 1$ ³. For $J_X > 1$ both (Θ, Φ) are free to move, defining a surface in the (Θ, Φ) plane. These surfaces are shown in Figure 7-4 for the $f_2(1270)$, $f_4(2050)$, and $f_2'(1525)$.

At this point we can check whether (Θ, Φ) depend on the mass of the decay. We split the $f_2(1270)$ and the $f_2'(1525)$ into a high mass and a low mass region. The plots of the error surfaces of the measured (Θ, Φ) show no significant separation for the different mass regions (see Figures 7-5 and 7-6).

³ In a two dimensional linear problem such a set of points defines the surface of the standard error ellipse.

Results for the correction factor and its systematic error are shown in Table 7-5.

Upper limits on $\Upsilon(1S) \rightarrow \gamma f_2(2220)$, $f_2(2220) \rightarrow h^+h^-$ are changed to include the angular distribution's effect on efficiency. Since we can't measure the helicity amplitudes in this case, we choose the worst possible case where the corrected efficiency is lowest. This always corresponds to $\Theta = \Phi = 0$. Results are in Table 7-6.

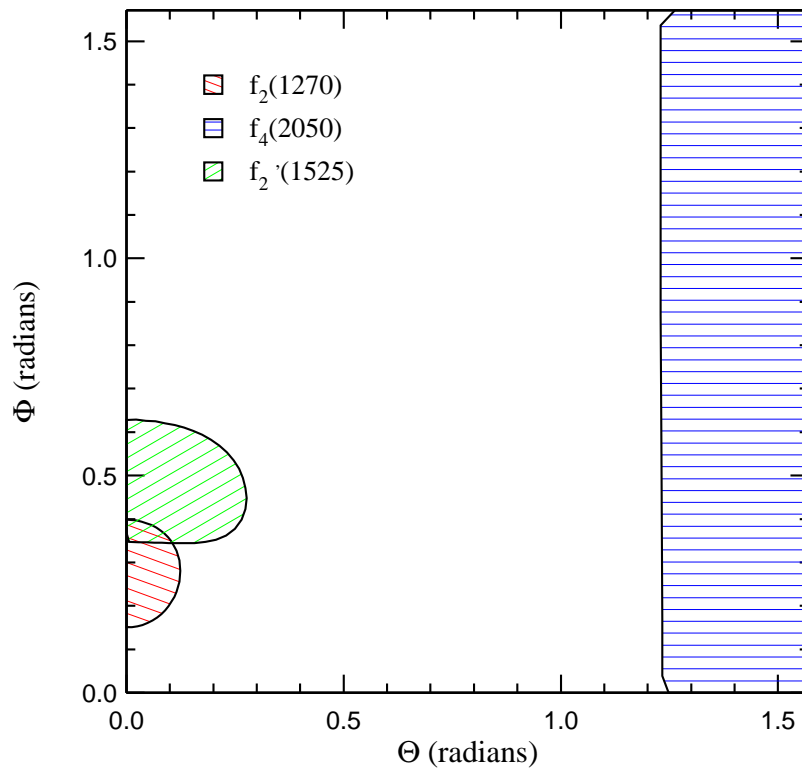


Figure 7-4: Surfaces in the (Θ, Φ) plane used to determine the systematic uncertainty in the efficiency correction factor for the modes with $f_2(1270)$, $f_4(2050)$, and $f_2'(1525)$. The $f_4(2050)$ surface may seem large, but when drawn in spherical coordinates it is a small “north pole cap”.

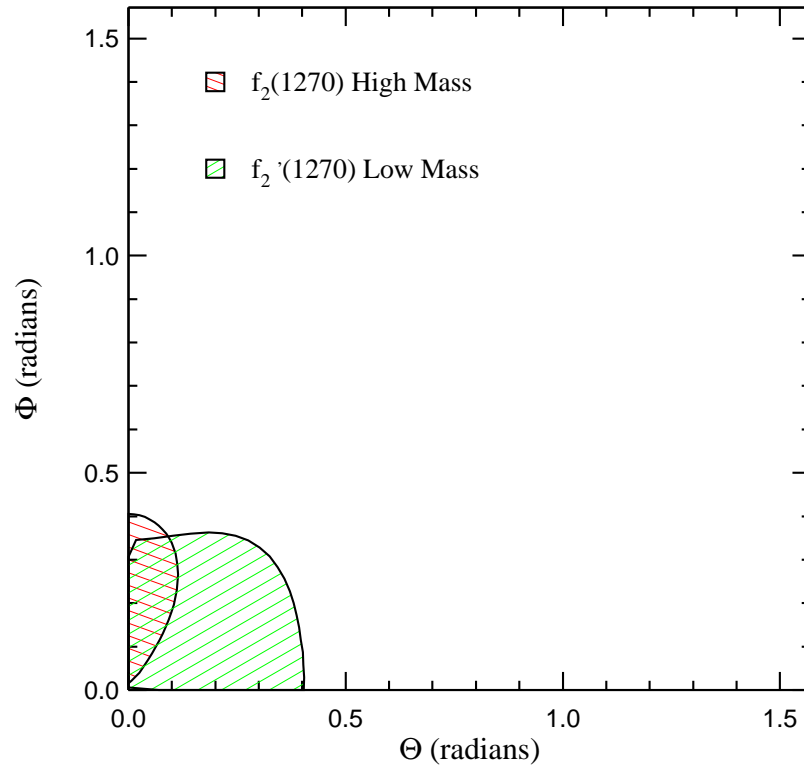


Figure 7–5: Measured (Θ, Φ) surfaces for the $f_2(1270)$ high and low mass regions.

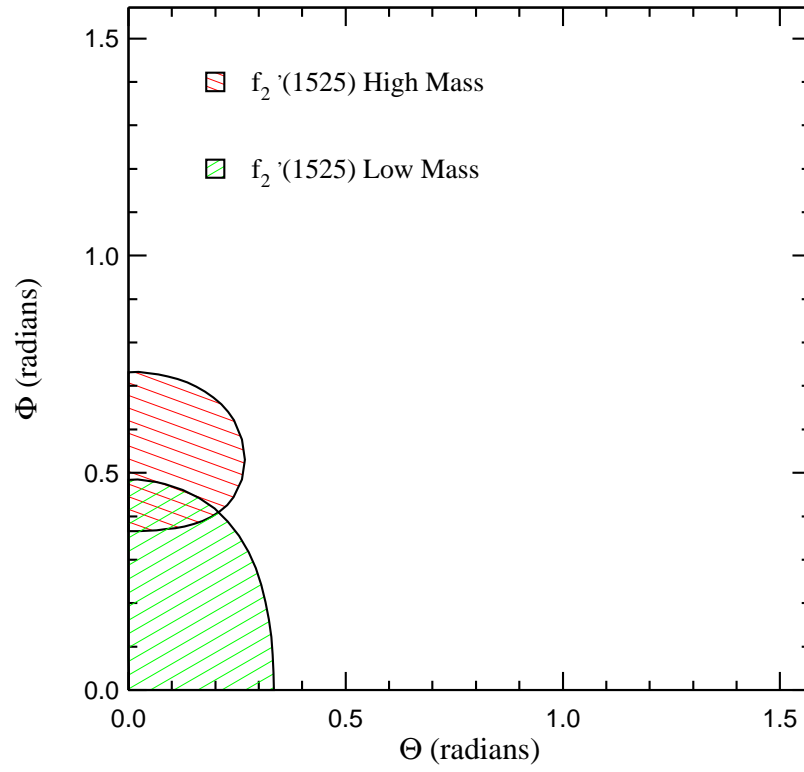


Figure 7-6: Measured (Θ, Φ) surfaces for the $f'_2(1525)$ high and low mass regions.

Table 7–5: Measured (Θ, Φ) , calculated ϵ^{J_X} , efficiency correction factor interval when (Θ, Φ) move away from their measured value under the condition that χ^2 stay within one unit of its minimum value, and the systematic uncertainty on the correction factor.

Mode	J_X	Θ	Φ	ϵ^{J_X}	Interval	Sys. Err. (%)
$\gamma f_0(980)$	0	0	0	0.91	0.91 - 0.91	0
$\gamma f_0(980)$	1	$0.0^{+0.4}_{-0.0}$	0	0.71	0.71 - 0.80	+13
$\gamma f_2(1270)$	2	$0.00^{+0.08}_{-0.00}$	$0.30^{+0.15}_{-0.10}$	0.78	0.76 - 0.80	± 3
$\gamma f_4(2050)$	4	$1.57^{+0.00}_{-0.34}$	0.2 ± 0.7	1.02	1.00 - 1.02	-2
$\gamma f'_2(1525)$	2	$0.00^{+0.27}_{-0.00}$	$0.50^{+0.12}_{-0.16}$	0.90	0.89 - 0.91	± 1
$\gamma f_0(1710)$	0	0	0	0.93	0.93-0.93	0
$\gamma K^+ K^-, 2 \text{ GeV}/c^2 < m(K^+ K^-) < 3 \text{ GeV}/c^2$	1	$0.16^{+0.19}_{-0.16}$	0	0.88	0.87 - 0.91	$^{+3}_{-1}$
$\gamma p \bar{p}, 2 \text{ GeV}/c^2 < m(p \bar{p}) < 3 \text{ GeV}/c^2$	1	$0.00^{+0.35}_{-0.00}$	0	0.92	0.92 - 0.95	+3

Table 7–6: Worst case efficiency correction factors and their effect on upper limits of $\Upsilon(1S) \rightarrow \gamma f_J(2220)$, $f_J(2220) \rightarrow h^+ h^-$ decays.

Mode	Worst case correction	Upper limit increase (%)
$f_J(2220) \rightarrow \pi^+ \pi^-$	0.75	+33
$f_J(2220) \rightarrow K^+ K^-$	0.88	+14
$f_J(2220) \rightarrow p \bar{p}$	0.92	+9

7.3 Different Hadronic Fake Rates Between 1S and 4S

Differences in the fake rates of hadronic events between the 1S and 4S data are another potential source of systematic errors when doing a continuum subtraction.

In principle this is a second order effect since the contamination is proportional to the difference of two small numbers. However since we have such a large number of ρ and ϕ events in the underlying 1S continuum, we should quantify any possible signal contamination. Section 3.2.2 outlines the three cases we need to worry about; ρ events contaminating the K^+K^- invariant mass plot, ρ contaminating the $p\bar{p}$ invariant mass plot, and ϕ events contaminating the $p\bar{p}$ invariant mass plot.

It is reasonable to assume that the 1S and 4S fake rates stay within 50% of each other (see Section 3.3.2 for some examples from MC measurements). With this assumption, taking $n_\rho \approx 20000$ and $n_\phi \approx 2000$ in the 1S data, and the fake rates measured in data (see Table 3–6) we can calculate the systematic uncertainties. We expect ± 27 events from ρ to contaminate the K^+K^- invariant mass plot. However, these events can be ignored as source of systematic uncertainty because 90% of them fall in the $1 - 1.5 \text{ GeV}/c^2$ region, below the $f_2'(1525)$ peak. We also expect ± 7 from ρ and ± 3 events from ϕ contaminating the $p\bar{p}$ invariant mass plot. This represents a $\pm 8\%$ systematic error for the $\Upsilon(1S) \rightarrow \gamma p\bar{p}$ mode.

7.4 Other Systematic Sources

Besides the systematic uncertainties described above, we also add a 2% systematic effect from track finding (1% per track) and 5% from the number of $\Upsilon(1S)$.

We find no evidence for non-resonant hadron pairs that could interfere with the resonances. There is a possible interference between $f_2(1275)$ and $f_2'(1525)$ because they both are in the $J = 2$ state. From the $f_2(1275)$ measurement in the $\pi^+\pi^-$ mode we expect 3 events from this source in the $f_2'(1525)$ mass region $1.45 -$

1.6 GeV/c². In the most extreme cases we have, $N \propto ||A_{f'_2(1525)}||^2 + ||A_{f_2(1270)}||^2 \pm 2||A_{f'_2(1525)}|| ||A_{f_2(1270)}||$, where $A_{f'_2(1525)}$ and $A_{f_2(1270)}$ are the amplitudes associated with $f'_2(1525)$ and $f_2(1270)$ respectively. From the data we have $N \approx 300$, and using the fact that $||A_{f_2(1270)}||^2$ contributes with 3 events, the contribution from $||A_{f'_2(1525)}||^2$ can range from 400 to 200 events. This represents a 30% variation from the central value. Since this is the extreme interference case, we take half of this value, 15%, as a reasonable systematic uncertainty from possible interference in the $f'_2(1525)$.

The possible decay $\Upsilon(1S) \rightarrow \rho\pi$ could contaminate our $\pi^+ \pi^-$ invariant mass plot, since a π^0 with a momentum greater than 4 GeV/c² looks very much like a photon. Using phase space MC and isospin symmetry, we estimate that about 40% of possible $\Upsilon(1S) \rightarrow \rho\pi$ have such a π^0 . The latest measured upper limit [24] for this decay mode is 1.9×10^{-6} . This gives an upper limit of 16 events in the efficiency corrected $\pi^+ \pi^-$ invariant mass plot, of which 10 events fall in the ρ mass region, behind the $f_0(980)$ mass region. The remaining potential 6 events could contaminate the rest of the invariant mass region. None of the signal regions is affected by more than 1%.

To test the robustness of the statistical fits, we redo them with all masses and widths of possible resonances required to stay within 1σ of their nominal PDG values [16]. The results from fitting the data in this way are within the statistical errors when compared to the fit results summarized in Table 4-1 and 5-1. We do not observe a systematic difference between these two fitting techniques.

The branching ratios for $f_2(1270) \rightarrow \pi^+ \pi^-$, $f_4(2050) \rightarrow \pi^+ \pi^-$, and $f'_2(1525) \rightarrow K^+ K^-$ are taken from the PDG [16] and contribute to the systematic uncertainty with $^{+2}_{-3}$, ± 9 , and ± 3 percent respectively.

7.5 Overall Systematic Uncertainties

We combine the systematic errors of each section in quadrature. Tables 7–7–7–8 summarize the systematic errors.

Table 7–7: Systematic errors expressed as % from the different sources described in the text. Not shown in the table, but included in the total, are a systematic uncertainty of 5% from the number of $\Upsilon(1S)$, a 2% systematic uncertainty from MC tracking in all the modes, a 15% systematic uncertainty in the $\gamma f'_2(1525)$ from possible interference with $\gamma f_2(1270)$, an 8% systematic uncertainty in the $\gamma p\bar{p}$ mode from possible hadronic contamination, and the systematic uncertainties in the $f_2(1270)$, $f_4(2050)$, and $f'_2(1525)$ hadronic branching fractions.

Mode	Analysis Cuts	Angular Distribution	Total
$\gamma f_0(980)$	± 3	0	± 6
$\gamma f_2(1270)$	± 3	± 3	± 7
$\gamma f_4(2050)$	± 3	+2	± 7
$\gamma f'_2(1525)$	± 8	± 1	± 20
$\gamma f_0(1710)$	± 8	0	± 10
$\gamma K^+ K^-(2 - 3 \text{ GeV}/c^2)$	± 8	$^{+1}_{-3}$	± 10
$\gamma p\bar{p}(2 - 3 \text{ GeV}/c^2)$	± 10	−3	± 14

Table 7–8: Increase in the upper limits of $\Upsilon(1S) \rightarrow \gamma f_J(2220)$ for different $f_J(2220)$ decay modes due to the possible systematic effects described in the text added in quadrature. Not shown in the table, but included in the total, are a 5% contribution from the number of $\Upsilon(1S)$ and of 2% contribution from MC tracking.

Mode	Analysis Cuts	Angular Distribution	Total
$f_J(2220) \rightarrow \pi^+ \pi^-$	$\pm 3\%$	+33%	+34%
$f_J(2220) \rightarrow K^+ K^-$	$\pm 8\%$	+14%	+17%
$f_J(2220) \rightarrow p\bar{p}$	$\pm 10\%$	+9%	+14%

CHAPTER 8

RESULTS AND CONCLUSION

We report on a new search for two-body radiative $\Upsilon(1S)$ decays. We place stringent limits on the production of the $f_J(2220)$ particle in the pion and kaon modes, and a less stringent limit in the proton mode where some excess of events is observed in the region of interest.

In the decay channel $\Upsilon(1S) \rightarrow \gamma\pi^+\pi^-$ we find clear evidence for the resonance $f_2(1270)$ and measure a branching fraction of $(13.3 \pm 1.4) \times 10^{-5}$, which is consistent with the earlier CLEO measurement of $(7.4_{-1.8}^{+2.7}) \times 10^{-5}$ [18]. The angular distributions of the photon and tracks strongly indicate that the hadron pairs we assign to the $f_2(1270)$ are indeed in a $J = 2$ state, and that nature prefers to produce the $f_2(1270)$ with 0 helicity. In contrast, for $J/\psi \rightarrow \gamma f_2(1270)$ it was found [29] that the $f_2(1270)$ is produced at equal rates with both helicity 0 and helicity 1, and at a rate consistent with 0 for helicity 2, but more recently [30] measured helicity 0 dominance for this same mode.

There is a barely significant (4.3σ) excess of events in the $f_0(980) \rightarrow \pi^+\pi^-$ invariant mass region. The angular distributions of the photon and tracks indicate that this excess of events is in a $J = 1$ state, rather than $J = 0$ which would be the case if the excess were due to $f_0(980)$ decays. It may be that this excess is due to non-resonant $\gamma\pi^+\pi^-$ production. We conclude that more data is needed to resolve this situation.

We find weak evidence for the production of the resonance $f_4(2050)$ in the $\Upsilon(1S) \rightarrow \gamma\pi^+\pi^-$ decay channel.

In the decay channel $\Upsilon(1S) \rightarrow \gamma K^+K^-$ we find strong evidence for the production of the resonance $f'_2(1525)$ and weak evidence for the production of

$f_0(1710)$. The photon and track angular distributions show that the two tracks attributed to the $f'_2(1525)$ are indeed in a $J = 2$ state and that the $f'_2(1525)$ is produced mostly with helicity 0. This is consistent with Kramer's theoretical prediction [31] and similar measurements done in the J/ψ system [32].

There is also evidence of an excess of events in the $2 - 3 \text{ GeV}/c^2 \ K^+ K^-$ invariant mass region, which we cannot attribute to any known resonances.

Finally, we also find evidence of an excess of events in the channel $\Upsilon(1S) \rightarrow \gamma p \bar{p}$, which we cannot attribute to any known resonances. We find no evidence of an enhancement near $p \bar{p}$ threshold. Such an enhancement was recently reported by [33] in the J/ψ system, and is currently being interpreted (See e.g. [34], [35], [36]).

When comparing the radiative $\Upsilon(1S)$ decays studied in this analysis to radiative J/ψ decays we observe a suppression ratio of 0.09 that is in reasonable agreement with the naive expectation of 0.025 obtained from scaling arguments.

Table 8–1 summarizes our results.

While we find hadronic resonances at a level consistent with the estimate of Section 1.2, we do not observe any glueball states. This is not the result we would expect from a naive interpretation of QCD, as the two gluons from a $\Upsilon(1S)$ radiative decay can form a bound state directly and need to go through at least two strong interaction vertexes to form a hadron.

Internal consistency in QCD predicts the existence of glueballs. Even though theoretical calculations of the glueball mass spectrum exist, a clear glueball observation has not been made yet. We conclude that more glueball searches are necessary to clarify this situation.

Table 8–1: Final measured branching ratios, measured branching ratios reported relative to J/ψ branching ratios, and statistical significance for each decay channel. The measured branching ratios have been corrected by the factors calculated in Appendix A2. For the branching ratios the first uncertainty is statistical and the second is systematic.

Channel	Branching Fraction $\times (10^{-5})$	$\frac{\Upsilon(1S)}{J/\psi}$	Significance
$\gamma f_0(980), f_0(980) \rightarrow \pi^+\pi^-$	$1.8_{-0.7}^{+0.8} \pm 0.1$	-	4.3σ
$\gamma f_2(1270)$	$13.3 \pm 1.0 \pm 0.9$	0.09 ± 0.01	$> 14\sigma$
$\gamma f_4(2050)$	$3.5 \pm 1.3 \pm 0.2$	0.019 ± 0.006	2.6σ
$\gamma f_2'(1525)$	$4.3_{-0.8}^{+1.0} \pm 0.9$	$0.09_{-0.04}^{+0.05}$	$> 14\sigma$
$\gamma f_0(1710), f_0(1710) \rightarrow K^+K^-$	$0.38 \pm 0.16 \pm 0.04$	$0.007_{-0.005}^{+0.004}$	3.2σ
γK^+K^-	$1.14 \pm 0.14 \pm 0.11$	-	9.1σ
$\gamma p\bar{p}$	$0.41 \pm 0.08 \pm 0.10$	0.011 ± 0.005	4.8σ
$\gamma f_J(2220), f_J(2220) \rightarrow \pi^+\pi^-$	< 0.08	-	-
$\gamma f_J(2220), f_J(2220) \rightarrow K^+K^-$	< 0.06	-	-
$\gamma f_J(2220), f_J(2220) \rightarrow p\bar{p}$	< 0.11	-	-

APPENDIX HELICITY FORMALISM FOR TWO BODY DECAYS

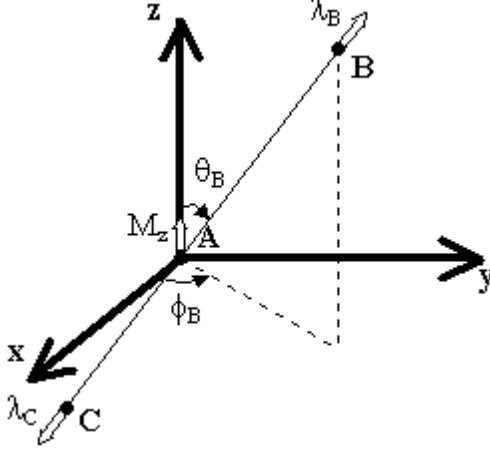
Helicity formalism can be used to obtain the angular distribution of a decay process. In this appendix we restrict ourselves to the case of two body decays. The situation is as follows: particle A with spin J_A , and z-axis spin projection M_A decays to two particles, $A \rightarrow B + C$ with definite helicity λ_B and λ_C . Let the direction of the of the decay be $\hat{n}(\theta, \phi) = \hat{n}(\theta_B, \phi_B) = \hat{p}_B = -\hat{p}_C$ (see Figure 1). The amplitude for this decay is,

$$\mathcal{A}_{\lambda_B \lambda_C}^{M_A} = \langle \theta \phi \lambda_B \lambda_C | H | J_A M_A \rangle . \quad (1)$$

We have little chance of directly calculating 1. But we can exploit the fact that H conserves angular momentum by considering the basis $\{ \langle j m \lambda_B \lambda_C | \}$, where j is the total angular momentum of $B + C$ and m its projection along the z axis¹. Inserting this basis into Equation 1,

$$\begin{aligned} \mathcal{A}_{\lambda_B \lambda_C}^{M_A} &= \sum_{jm} \langle \theta \phi \lambda_B \lambda_C | j m \lambda_B \lambda_C \rangle \langle j m \lambda_B \lambda_C | H | J_A M_A \rangle \\ &= \sum_{jm} \langle \theta \phi \lambda_B \lambda_C | j m \lambda_B \lambda_C \rangle \delta_{j J_A} \delta_{m M_A} A_{\lambda_B \lambda_C} \\ &= \langle \theta \phi \lambda_B \lambda_C | J_A M_A \lambda_B \lambda_C \rangle A_{\lambda_B \lambda_C} . \end{aligned}$$

¹ The rotational invariance of helicities is a necessary condition to construct $\{ \langle j m \lambda_B \lambda_C | \}$ as a basis for the two-particle state $B + C$. Rotational invariance is one of two key ideas in helicity formalism. The other key idea, which is boost invariance, is useful in sequential decays.

Figure 1: $A \rightarrow B + C$.

The above equation contains two factorized terms. The first term is independent of the interaction H and contains the angular distribution information we are interested in. The second term, $A_{\lambda_B \lambda_C}$, is usually called the “helicity coupling amplitude”. It is independent of the angular distribution, and contains the physics of the decay (in particular it depends on λ_B and λ_C , but not on M_A). In the helicity formalism, the helicity coupling amplitudes are unknown parameters.

For strong and electromagnetic decays there is another invariance of H we can exploit; parity. For these kind of interactions it can be shown by inserting the parity operator that,

$$A_{-\lambda_B - \lambda_C} = (-1)^{J_A - J_B - J_C} \eta_A \eta_B \eta_C A_{\lambda_B \lambda_C} \quad (2)$$

where $\eta_A \eta_B \eta_C$ is the product of the parity of particles A, B and C. This useful property of $A_{\lambda_B \lambda_C}$ reduces the number of unknown parameters in the angular distribution of strong and electromagnetic decays.

The next step is to derive explicit formulae for $\langle \theta \phi \lambda_B \lambda_C | J_A M_A \lambda_B \lambda_C \rangle$ for the $B + C$ system. Such derivation, which is out of the scope of this appendix, will

be omitted here². The result can be expressed in terms of the Wigner functions,

$$\langle \theta \phi \lambda_B \lambda_C | J_A M_A \lambda_B \lambda_C \rangle = \sqrt{\frac{2J+1}{4\pi}} D_{M_A, \lambda}^{*J_A}(\phi, \theta, -\phi) \quad (3)$$

where $\lambda = \lambda_B - \lambda_C$ and,

$$D_{M_A, \lambda}^{J_A}(\phi, \theta, -\phi) = e^{-i\phi(M_A - \lambda)} d_{M_A, \lambda}^{J_A}(\theta). \quad (4)$$

The functions $d_{M_A, \lambda}^{J_A}(\theta)$ have real values, and some of them are given in the particle data book.

We have finally arrived to the following important relation,

$$\mathcal{A}_{\lambda_B \lambda_C}^{M_A} = \sqrt{\frac{2J_A+1}{4\pi}} D_{M_A, \lambda}^{*J_A} \mathcal{A}_{\lambda_B \lambda_C}. \quad (5)$$

All helicity distribution calculations are reduced to handling these basic amplitudes. Here are some of their very important properties,

$$\mathcal{A}_{\lambda_B \lambda_C}^{M_A} = 0 \quad \text{if} \quad |\lambda_B - \lambda_C| > J_A, \quad (6)$$

$$\| \mathcal{A}_{\lambda_B \lambda_C}^{-M_A} \| = \| \mathcal{A}_{\lambda_B \lambda_C}^{M_A} \|, \quad (7)$$

$$\int_0^{2\pi} d\phi \mathcal{A}_{\lambda_B \lambda_C}^{M_A} \mathcal{A}_{\lambda'_B \lambda'_C}^{*M'_A} = 2\pi \delta_{(\lambda - \lambda')}^{(M_A - M'_A)} \mathcal{A}_{\lambda_B \lambda_C}^{M_A} \mathcal{A}_{\lambda'_B \lambda'_C}^{*M'_A}, \quad (8)$$

$$\int d\Omega \mathcal{A}_{\lambda_B \lambda_C}^{M_A} \mathcal{A}_{\lambda'_B \lambda'_C}^{*M'_A} = \delta_{(\lambda - \lambda')}^{(M_A - M'_A)} \| \mathcal{A}_{\lambda_B \lambda_C} \| ^2. \quad (9)$$

Property 6 is a reflection of the physical fact that the projection of the total angular momentum along a particular axis cannot be greater than the total angular momentum itself.

² The interested reader can find this derivation in [37]

$\| \mathcal{A}_{\lambda_B \lambda_C}^{M_A} \|^2$ is the angular distribution of a final state where M_A and the helicities of B and C are known (see Equation 1). However, it is usually the case that $M_A \lambda_B \lambda_C$ are not known. In such cases we can only measure the overall angular distribution, which is simply the average over possible initial states of the incoherent sum of final states,

$$\frac{dP}{d\Omega_B} = \sum_{M_A \lambda_B \lambda_C} P_{M_A} \frac{dP_{\lambda_B \lambda_C}^{M_A}}{d\Omega_B} = \sum_{M_A \lambda_B \lambda_C} P_{M_A} \| \mathcal{A}_{\lambda_B \lambda_C}^{M_A} \|^2 \quad (10)$$

where P_{M_A} is the weight of the initial state M_A and $d\Omega_B = d(\cos(\theta_B))d\phi_B$.

Next, consider a sequential decay, $A \rightarrow B + C$ with $C \rightarrow D + E$ (see Figure 2). The rotational and boost invariance of helicities makes it easy to extend the helicity formalism to this case. To do so we consider a new reference frame, O' , at rest with C , such that $\hat{z}' = \hat{n}(\theta_B, \phi_B)^3$. All particle helicities remain the same in O' , and in particular $M_z(C) = -\lambda_C$ (the negative sign arises from the fact that $\hat{n}(\theta_B, \phi_B)$ is the direction in which B is traveling). It is now straightforward to calculate the intermediate amplitude $\mathcal{C}_{\lambda_D \lambda_E}^{-\lambda_C}$ at O' . Of course $\mathcal{A}_{\lambda_B \lambda_C}^{M_A}$ is still calculated at A 's original rest frame. Since λ_C is an intermediate state, the helicity amplitude for the final state $\lambda_B \lambda_D \lambda_E$ is,

$$\mathcal{A}_{\lambda_B \lambda_D \lambda_E}^{M_A} = \sum_{\lambda_C} \mathcal{A}_{\lambda_B \lambda_C}^{M_A} \mathcal{C}_{\lambda_D \lambda_E}^{-\lambda_C} \quad (11)$$

where we have coherently summed over the intermediate state C . If $M_A \lambda_B \lambda_D \lambda_E$ are not known,

$$\frac{dP}{d\Omega_B d\Omega_D} = \sum_{M_A \lambda_B \lambda_D \lambda_E} P_{M_A} \frac{dP_{\lambda_B \lambda_D \lambda_E}^{M_A}}{d\Omega_B d\Omega_D} = \sum_{M_A \lambda_B \lambda_D \lambda_E} P_{M_A} \| \mathcal{A}_{\lambda_B \lambda_D \lambda_E}^{M_A} \|^2. \quad (12)$$

³ This condition does not unlikely determine O' . We can be more precise by defining $O' = L(\vec{p}_C)R(\phi_B, \theta_B, 0)O$, where L is the Lorentz Boost operator, R is the rotation operator in terms of the Euler angles, and O is A 's original rest frame.

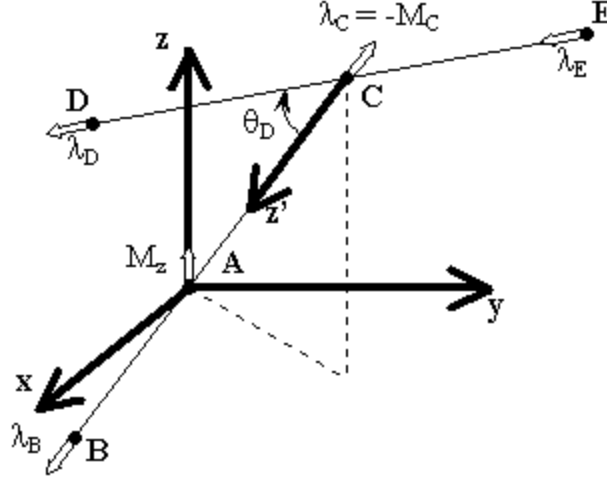


Figure 2: $A \rightarrow B + C$ and $C \rightarrow D + E$. The drawing is peculiar in that C 's daughters are drawn as seen in C 's rest frame (back-to-back).

The sequential decay amplitudes have the following important properties,

$$\| \mathcal{AC}_{\lambda_B \lambda_D \lambda_E}^{-M_A} \| = \| \mathcal{AC}_{\lambda_B \lambda_D \lambda_E}^{M_A} \|, \quad (13)$$

$$\int_0^{2\pi} d\phi_B \int_0^{2\pi} d\phi_D \| \mathcal{AC}_{\lambda_B \lambda_D \lambda_E}^{M_A} \|^2 = 4\pi^2 \sum_{\lambda_C} \| \mathcal{A}_{\lambda_B \lambda_C}^{M_A} \|^2 \| \mathcal{C}_{\lambda_D \lambda_E}^{\lambda_C} \|^2. \quad (14)$$

This kind of logic can be extended to a general two-body decay chain.

Example: $\Upsilon(1S) \rightarrow \gamma f_2(1270) (f_2(1270) \rightarrow \pi^+ \pi^-)$

From our previous discussion we can immediately write (see Equation 11),

$$\mathcal{AC}_{\lambda_\gamma \lambda_{\pi^+} \lambda_{\pi^-}}^{M_{\Upsilon(1S)}} = \sum_{\lambda_{f_2(1270)}} \mathcal{A}_{\lambda_\gamma \lambda_{f_2(1270)}}^{M_{\Upsilon(1S)}} \mathcal{C}_{\lambda_{\pi^+} \lambda_{\pi^-}}^{-\lambda_{f_2(1270)}}$$

In this case, $\lambda_{\pi^-} = \lambda_{\pi^+} = 0$, $\lambda_\gamma = \pm 1$. In CLEO $M_{\Upsilon(1S)} = \pm 1$, there is no $M_{\Upsilon(1S)} = 0$ since at the $\Upsilon(1S)$ energy electrons couple only to positrons of the opposite helicity, this way $P_1 = P_{-1} = \frac{1}{2}$ and $P_0 = 0$ is an excellent approximation.. There are therefore four amplitudes we must consider, \mathcal{AC}_{100}^1 , \mathcal{AC}_{100}^{-1} , \mathcal{AC}_{-100}^1 and \mathcal{AC}_{-100}^{-1} .

The overall angular distribution is (see Equation 12),

$$\begin{aligned} \frac{dP}{d\Omega_\gamma d\Omega_{\pi^+}} &= \frac{1}{2} \| \mathcal{A} \mathcal{C}_{100}^1 \|^2 + \frac{1}{2} \| \mathcal{A} \mathcal{C}_{-100}^1 \|^2 + \frac{1}{2} \| \mathcal{A} \mathcal{C}_{100}^{-1} \|^2 + \frac{1}{2} \| \mathcal{A} \mathcal{C}_{100}^{-1} \|^2 \\ &= \| \mathcal{A} \mathcal{C}_{100}^1 \|^2 + \| \mathcal{A} \mathcal{C}_{-100}^1 \|^2 \end{aligned} \quad (15)$$

where we have used property 13. The two relevant amplitudes are,

$$\begin{aligned} \mathcal{A} \mathcal{C}_{100}^1 &= \mathcal{A}_{10}^1 \mathcal{C}_{00}^0 + \mathcal{A}_{11}^1 \mathcal{C}_{00}^{-1} + \mathcal{A}_{12}^1 \mathcal{C}_{00}^{-2} \\ \mathcal{A} \mathcal{C}_{-100}^1 &= \mathcal{A}_{-10}^1 \mathcal{C}_{00}^0 + \mathcal{A}_{-1-1}^1 \mathcal{C}_{00}^1 + \mathcal{A}_{-1-2}^1 \mathcal{C}_{00}^2 \end{aligned}$$

where we have used the fact that $|\lambda_\gamma - \lambda_{f_2(1270)}| \leq J_{T(1S)} = 1$ to sum over all possible $\lambda_{f_2(1270)}$.

All that remains is to substitute,

$$\begin{aligned} \| \mathcal{A} \mathcal{C}_{100}^1 \|^2 &= \| \mathcal{A}_{10}^1 \mathcal{C}_{00}^0 \|^2 + \| \mathcal{A}_{11}^1 \mathcal{C}_{00}^{-1} \|^2 + \| \mathcal{A}_{12}^1 \mathcal{C}_{00}^{-2} \|^2 + \\ &\quad \{ \mathcal{A}_{10}^1 \mathcal{C}_{00}^0 \mathcal{A}_{11}^{*1} \mathcal{C}_{00}^{*-1} + \mathcal{A}_{10}^1 \mathcal{C}_{00}^0 \mathcal{A}_{12}^{*1} \mathcal{C}_{00}^{*-2} + \mathcal{A}_{11}^1 \mathcal{C}_{00}^{-1} \mathcal{A}_{12}^{*1} \mathcal{C}_{00}^{*-2} + c.c. \} \\ \| \mathcal{A} \mathcal{C}_{-100}^1 \|^2 &= \| \mathcal{A}_{-10}^1 \mathcal{C}_{00}^0 \|^2 + \| \mathcal{A}_{-1-1}^1 \mathcal{C}_{00}^1 \|^2 + \| \mathcal{A}_{-1-2}^1 \mathcal{C}_{00}^2 \|^2 + \\ &\quad \{ \mathcal{A}_{-10}^1 \mathcal{C}_{00}^0 \mathcal{A}_{-1-1}^{*1} \mathcal{C}_{00}^{*1} + \mathcal{A}_{-10}^1 \mathcal{C}_{00}^0 \mathcal{A}_{-1-2}^{*1} \mathcal{C}_{00}^{*2} + \mathcal{A}_{-1-1}^1 \mathcal{C}_{00}^1 \mathcal{A}_{-1-2}^{*1} \mathcal{C}_{00}^{*2} + c.c. \} \end{aligned} \quad (16)$$

into Equation 15.

Doing so will give us the full angular distribution of the decay chain. However, using property 8, all the cross terms inside $\{...\}$ vanish if we integrate over ϕ_{π^+} or ϕ_γ . For the time being we integrate over both ϕ_{π^+} and ϕ_γ . We will return to the

terms inside $\{...\}$ later.

$$\begin{aligned}
& \int_0^{2\pi} d\phi_\gamma \int_0^{2\pi} d\phi_{\pi^+} \frac{dP}{d\Omega_\gamma d\Omega_{\pi^+}} = \\
& 4\pi^2 [(\| \mathcal{A}_{10}^1 \|^2 + \| \mathcal{A}_{-10}^1 \|^2) \| \mathcal{C}_{00}^0 \|^2 + \\
& (\| \mathcal{A}_{11}^1 \|^2 + \| \mathcal{A}_{-1-1}^1 \|^2) \| \mathcal{C}_{00}^1 \|^2 + \\
& (\| \mathcal{A}_{12}^1 \|^2 + \| \mathcal{A}_{-1-2}^1 \|^2) \| \mathcal{C}_{00}^2 \|^2] \\
& = \frac{15}{4} [\| A_{10} \|^2 \| C_{00} \|^2 (d_{11}^1(\theta_\gamma)^2 + d_{1-1}^1(\theta_\gamma)^2) d_{00}^2(\theta_{\pi^+})^2 + \\
& \| A_{11} \|^2 \| C_{00} \|^2 (d_{10}^1(\theta_\gamma)^2 + d_{-10}^1(\theta_\gamma)^2) d_{10}^2(\theta_{\pi^+})^2 + \\
& \| A_{12} \|^2 \| C_{00} \|^2 (d_{1-1}^1(\theta_\gamma)^2 + d_{-1-1}^1(\theta_\gamma)^2) d_{20}^2(\theta_{\pi^+})^2] \\
& = \frac{15}{4} \| C_{00} \|^2 [\| A_{10} \|^2 \frac{1}{2} (1 + \cos^2 \theta_\gamma) (\frac{3}{2} \cos^2 \theta_{\pi^+} - \frac{1}{2})^2 + \\
& \| A_{11} \|^2 \sin^2 \theta_\gamma (\sqrt{\frac{3}{2}} \sin \theta_{\pi^+} \cos \theta_{\pi^+})^2 + \\
& \| A_{12} \|^2 \frac{1}{2} (1 + \cos^2 \theta_\gamma) (\frac{3}{8} \sin^4 \theta_{\pi^+})].
\end{aligned}$$

At this point it is convenient to define the normalized helicity amplitudes,

$$\begin{aligned}
a_{10} &= \frac{A_{10}}{\sqrt{\| A_{10} \|^2 + \| A_{11} \|^2 + \| A_{12} \|^2}} \\
a_{11} &= \frac{A_{11}}{\sqrt{\| A_{10} \|^2 + \| A_{11} \|^2 + \| A_{12} \|^2}} \\
a_{12} &= \frac{A_{12}}{\sqrt{\| A_{10} \|^2 + \| A_{11} \|^2 + \| A_{12} \|^2}}
\end{aligned}$$

which satisfy,

$$\| a_{10} \|^2 + \| a_{11} \|^2 + \| a_{12} \|^2 = 1. \quad (17)$$

The normalized probability distribution, $\frac{dU}{d(\cos \theta_\gamma)d(\cos \theta_{\pi^+})}$, can be obtained by dividing the probability distribution by the branching fraction of the sequential decay,

$$\begin{aligned} P &= 2 \|C_{00}\|^2 (\|A_{10}\|^2 + \|A_{11}\|^2 + \|A_{12}\|^2) \\ &= \|C_{00}\|^2 \|A_{10}\|^2 + \|C_{00}\|^2 \|A_{11}\|^2 + \|C_{00}\|^2 \|A_{12}\|^2 + \\ &\quad \|C_{00}\|^2 \|A_{-10}\|^2 + \|C_{00}\|^2 \|A_{-1-1}\|^2 + \|C_{00}\|^2 \|A_{-1-2}\|^2. \end{aligned}$$

This way,

$$\begin{aligned} \frac{dU}{d(\cos \theta_\gamma)d(\cos \theta_{\pi^+})} &= \|a_{10}\|^2 \frac{3}{8}(1 + \cos^2 \theta_\gamma) \frac{5}{8}(3 \cos^2 \theta_{\pi^+} - 1)^2 + \\ &\quad \|a_{11}\|^2 \frac{3}{4} \sin^2 \theta_\gamma \frac{15}{4} (\sin \theta_{\pi^+} \cos \theta_{\pi^+})^2 + \\ &\quad \|a_{12}\|^2 \frac{3}{8}(1 + \cos^2 \theta_\gamma) \frac{15}{16} \sin^4 \theta_{\pi^+}. \end{aligned}$$

It is useful to project the angular distribution on θ_γ and θ_{π^+} ,

$$\begin{aligned} \frac{dU}{d \cos \theta_{\pi^+}} &= \|a_{10}\|^2 \frac{5}{8}(3 \cos^2 \theta_{\pi^+} - 1)^2 + \|a_{11}\|^2 \frac{15}{4} (\sin \theta_{\pi^+} \cos \theta_{\pi^+})^2 + \\ &\quad \|a_{12}\|^2 \frac{15}{16} \sin^4 \theta_{\pi^+} \end{aligned} \quad (18)$$

$$\frac{dU}{d \cos \theta_\gamma} = (\|a_{10}\|^2 + \|a_{12}\|^2) \frac{3}{8}(1 + \cos^2 \theta_\gamma) + \|a_{11}\|^2 \frac{3}{4} \sin^2 \theta_\gamma. \quad (19)$$

Let us now return to the terms inside $\{\dots\}$ in Equation 16. It turns out that for these terms a substantial simplification occurs if we integrate over $\cos \theta_{\pi^+}$. After some algebra, we arrive at the following expression,

$$\frac{dU}{d(\phi_\gamma - \phi_{\pi^+})} = \frac{1}{2\pi} \left(1 - \frac{1}{\sqrt{6}} \{a_{10}a_{12}^* + a_{10}^*a_{12}\} \cos[2(\phi_\gamma - \phi_{\pi^+})]\right). \quad (20)$$

Example: $\Upsilon(1S) \rightarrow \gamma f_4(2050)(f_4(2050) \rightarrow \pi^+\pi^-)$

For the case $f_4(2050)$ the calculation is very similar to the $f_2(1270)$ case discussed above. The allowed helicities for $f_4(2050)$ are the same as the allowed helicities for $f_2(1270)$. This makes the angular distribution calculation very similar to the $f_2(1270)$ case, the only difference being that the functions $d_{\lambda_{f_2(1270)0}}^2$ are replaced by $d_{\lambda_{f_4(2050)0}}^4$.

The photon's angular distribution comes out to be the same. The result for the pion's normalized angular distribution is,

$$\begin{aligned} \frac{dU}{d \cos \theta_{\pi^+}} = & \|a_{10}\|^2 \frac{9}{128} (35 \cos^4 \theta_{\pi^+} - 30 \cos^2 \theta_{\pi^+} + 3)^2 + \\ & \|a_{11}\|^2 \frac{45}{32} (\sin \theta_{\pi^+} \cos \theta_{\pi^+})^2 (7 \cos^2 \theta_{\pi^+} - 3)^2 + \\ & \|a_{12}\|^2 \frac{45}{64} \sin^4 \theta_{\pi^+} (7 \cos^2 \theta_{\pi^+} - 1)^2. \end{aligned} \tag{21}$$

Fit of the Helicity Angular Distribution Obtained from Data

In practice, a particular bin in the helicity angular distribution obtained from data has bins with $dN = NdU$ events, where N is the total number of events (which is allowed to float during the fit), and dU is the portion of the normalized probability assigned to the bin by the helicity formalism prediction.

To incorporate Equation 17 directly into the fit we make the following change of variables,

$$\|a_{10}\| = \cos \Theta \cos \Phi; \quad \|a_{12}\| = \cos \Theta \sin \Phi; \quad \|a_{11}\| = \sin \Theta. \tag{22}$$

Because of this definition, both Θ and Φ should be required to be within the interval $(0, \frac{\pi}{2})$ during the fit. The new variables have the convenient property that for $J=0$, $\Phi = \Theta = 0$, and for $J = 1$, $\Phi=0$. In general there are 1, 2 and 3 degrees

of freedom for the fits with $J = 0$, $J = 1$, and $J > 1$ respectively. One degree of freedom always corresponds to the number of events, N , and the other two correspond to Θ and Φ , which determine the magnitude of the normalized helicity amplitudes through Equation 22⁴.

When fitting, it is preferable to choose the full 2D helicity angular distribution which is a function of θ_γ and θ_{π^+} instead of its one dimensional projections. The 2D choice is better not only because the 2D distribution carries the maximum amount of information, but because in general the efficiency depends on both the pion and photon helicity angles, which can lead to complications when efficiency correcting the one-dimensional projections. Building on the two previous examples the 2D helicity angular distributions for $J = 0, 1, 2, 3, 4$ are (for compactness we define $x = \cos \theta_{\pi^+}$ and $y = \cos \theta_\gamma$),

$$\frac{dN_{J=0}}{dxdy} = N_{J=0} \frac{3}{8} (1 + y^2) \frac{1}{2} \quad (23)$$

$$\begin{aligned} \frac{dN_{J=1}}{dxdy} = N_{J=1} & \left(\cos^2 \Theta \frac{3}{8} (1 + y^2) \frac{3}{2} x^2 + \right. \\ & \left. \sin^2 \Theta \frac{3}{4} (1 - y^2) \frac{3}{4} (1 - x^2) \right) \end{aligned} \quad (24)$$

⁴ Obtaining the error of the normalized helicity amplitudes requires some matrix multiplication. For compactness let us define $\vec{a} = \begin{pmatrix} a_{10} \\ a_{12} \\ a_{11} \end{pmatrix}$ and $\vec{\omega} = \begin{pmatrix} \Theta \\ \Phi \end{pmatrix}$. The error matrix for the normalized helicity amplitudes is,

$$< \delta \vec{a} \delta \vec{a}^T > = \frac{\partial \vec{a}}{\partial \vec{\omega}} < \delta \vec{\omega} \delta \vec{\omega}^T > \frac{\partial \vec{a}^T}{\partial \vec{\omega}}$$

where $< \delta \vec{\omega} \delta \vec{\omega}^T >$ is the error matrix obtained from the fit.

$$\begin{aligned}
\frac{dN_{J=2}}{dxdy} = N_{J=2} & \left(\cos^2 \Theta \cos^2 \Phi \frac{3}{8}(1+y^2) \frac{5}{8}(3x^2-1)^2 + \right. \\
& \sin^2 \Theta \frac{3}{4}(1-y^2) \frac{15}{4}x^2(1-x^2) + \\
& \left. \cos^2 \Theta \sin^2 \Phi \frac{3}{8}(1+y^2) \frac{15}{16}(1-x^2)^2 \right)
\end{aligned} \tag{25}$$

$$\begin{aligned}
\frac{dN_{J=3}}{dxdy} = N_{J=3} & \left(\cos^2 \Theta \cos^2 \Phi \frac{3}{8}(1+y^2) \frac{7}{8}(5x^3-3x)^2 + \right. \\
& \sin^2 \Theta \frac{3}{4}(1-y^2) \frac{21}{32}(1-x^2)(5x^2-1)^2 + \\
& \left. \cos^2 \Theta \sin^2 \Phi \frac{3}{8}(1+y^2) \frac{105}{16}x^2(1-x^2)^2 \right)
\end{aligned} \tag{26}$$

$$\begin{aligned}
\frac{dN_{J=4}}{dxdy} = N_{J=4} & \left(\cos^2 \Theta \cos^2 \Phi \frac{3}{8}(1+y^2) \frac{9}{128}(35x^4-30x^2+3)^2 + \right. \\
& \sin^2 \Theta \frac{3}{4}(1-y^2) \frac{45}{32}x^2(1-x^2)(7x^2-3)^2 + \\
& \left. \cos^2 \Theta \sin^2 \Phi \frac{3}{8}(1+y^2) \frac{45}{64}(1-x^2)^2(7x^2-1)^2 \right).
\end{aligned} \tag{27}$$

In this analysis, because of our low statistics (and by low statistics we mean that there are numerous bins with < 1 events in the 2D plots), we project Equations 23-27 on $x = \cos \theta_\pi$, and $y = \cos \theta_\gamma$. We also fold each distribution around its symmetry axis $x = 0$ and $y = 0$ to increase each bin's statistics. Finally, we do a simultaneous fit to both distributions and obtain N , Θ , and Φ .

Admittedly, this procedure has the problems described previously when 2D fits were advocated, which can give rise to systematic effects in the measured helicity amplitudes. In essence, we need to use a unitary weight function proportional to the efficiency distribution (see Figure 7-3) in the integrals used to make the projections. This affects the relative strength of each helicity amplitude and the overall efficiency, but does not change each projected shape. However, the helicity amplitudes themselves are only used to calculate systematic effects on the efficiency

of resonances, so by simultaneously fitting the unweighted 1D projections we are just ignoring the systematics on the systematics.

Finally, let us consider the $\phi_\gamma - \phi_{\pi^+}$ distribution for $J = 2$. Equation 20 becomes,

$$\frac{dN_{J=2}}{d(\phi_\gamma - \phi_{\pi^+})} = \frac{N_{J=2}}{2\pi} \left(1 - \frac{1}{\sqrt{6}} \{\cos^2 \Theta \sin 2\Phi \cos \Delta\} \cos[2(\phi_\gamma - \phi_{\pi^+})]\right) \quad (28)$$

where the new degree of freedom Δ is the relative phase between a_{10} and a_{20} . The deviation from the flat distribution is characterized by

$$R = \frac{1}{\sqrt{6}} \{\cos^2 \Theta \sin 2\Phi \cos \Delta\} \leq \frac{1}{\sqrt{6}}. \quad (29)$$

The bigger this factor is, the easier it is to observe in data. Figure 3 shows the continuum subtracted $\phi_\gamma - \phi_{\pi^+}$ distribution for events near the $f_2(1270)$ resonance. The factor R obtained from fitting the distribution is non-significant. It is a bit tedious but straightforward to calculate the $\phi_\gamma - \phi_{\pi^+}$ distribution for other J values. We will not present those results here. They are not very interesting because we need large statistics to observe deviations from the flat distribution, and there is no effect on the efficiency from non-flat $\phi_\gamma - \phi_{\pi^+}$ distributions.

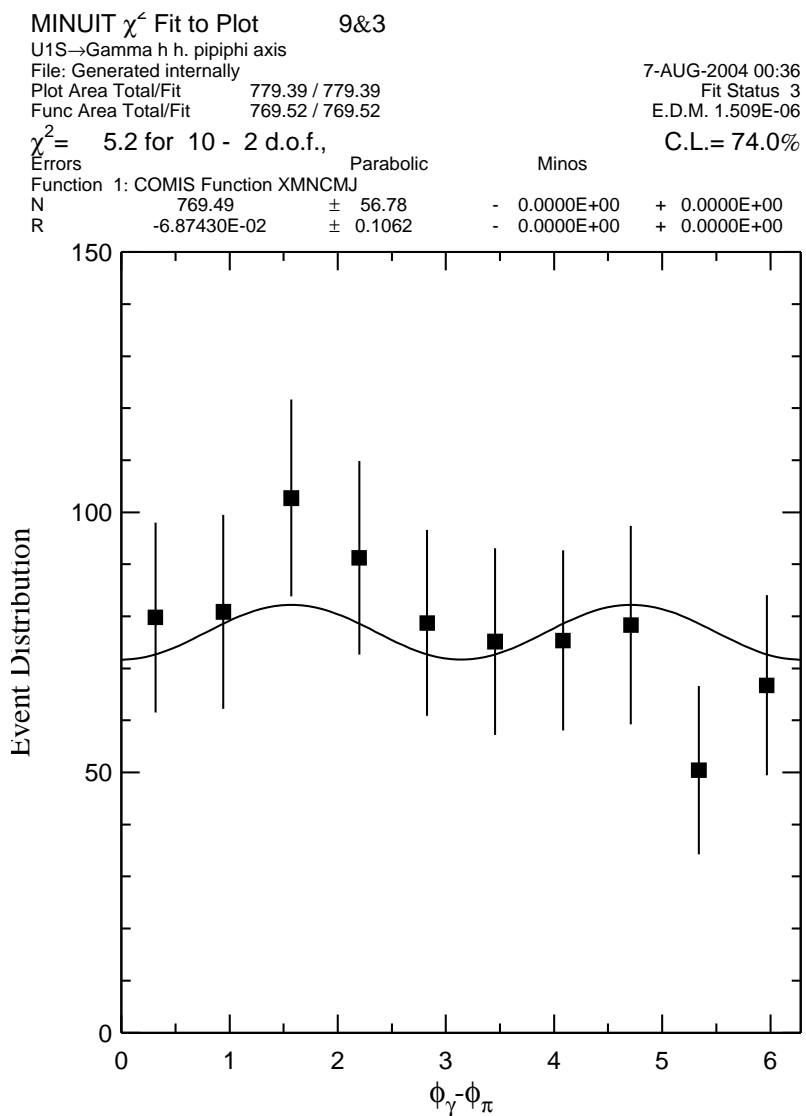


Figure 3: Continuum subtracted $\phi_\gamma - \phi_{\pi^+}$ distribution for events near the $f_2(1270)$ resonance with a fit to Equation 28 overlayed.

Example: Continuum Events.

Our previous examples tackled radiative decays of the $\Upsilon(1S)$. Now let us consider the continuum “radiative beam” process $e^+e^- \rightarrow \gamma\pi^+\pi^-$. The helicity formalism can be applied at the CM of the $\pi^+\pi^-$ vertex, where the initial state has $J^P = 1^-$. We have $1^- \rightarrow 0^-0^-$ at the $\pi^+\pi^-$ vertex and there is only one helicity amplitude we need to consider,

$$\mathcal{A}_{00}^1 = \sqrt{\frac{3}{4\pi}} D_{10}^{*1} A_{00} \quad (30)$$

which after a couple simple steps leads to,

$$\frac{dN}{d\cos\theta_{\pi^+}} = N \frac{3}{4} \sin^2\theta_{\pi^+}. \quad (31)$$

This result is also valid for the kaon case.

On the other hand, the photon’s angular distribution cannot be calculated using two-body helicity formalism. A good approximation is (see [38] Appendix B),

$$\frac{dP}{d\cos\theta_\gamma} \propto \frac{1 + \cos^2\theta_\gamma}{1 - \cos^2\theta_\gamma}, \quad (32)$$

which is not valid at low θ angles ($\theta \rightarrow 0$, $\theta \rightarrow \pi$) because of the effects on the approximation of the neglected electron mass.

Figure 4 shows these angular distributions in 4S “radiative beam” events. The agreement between theory and experiment is excellent. This is reassuring, because in the main analysis we rely on our angular distribution measurements to get the correct efficiency in data and to identify the J value and helicity amplitude distribution of each resonance.

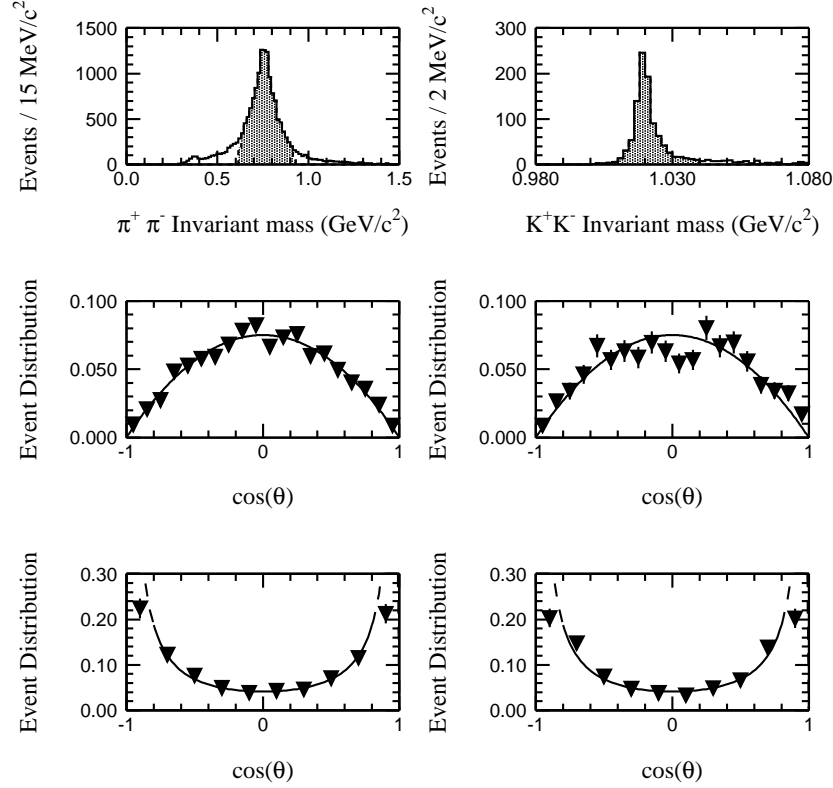


Figure 4: Helicity angle distribution for “radiative beam” continuum events $e^+e^- \rightarrow \gamma\rho$ and $e^+e^- \rightarrow \gamma\phi$ in the 4S data. Top left (right) plot shows in gray the events selected as $\rho \rightarrow \pi^+\pi^-$ ($\phi \rightarrow K^+K^-$). Middle left (right) plot shows the $\pi^+\pi^-$ (K^+K^-) helicity angle distribution for the selected events, and has the helicity formalism prediction, Equation 31, overlaid. Bottom left (right) plot shows the γ angular distribution for the photon accompanying the ρ (ϕ), and has the first order QED prediction, Equation 32, overlaid.

REFERENCES

- [1] A. Filippi, “Glueballs and Hybrids in the 1-GeV to 2-GeV Region: An Experimental Overview,” eConf **C0309101**, FRWP012 (2003).
- [2] H. Stöck, CLEO internal note CBX **02-35** (2002) (unpublished).
- [3] F.E. Close and A. Kirk, Eur. Phys. J. C **21**, 531-543 (2001).
- [4] C.A. Meyer, “Proceedings of the Workshop on Gluonic Excitations”, Newport News, Virginia 2003, AIP Conf. Proc. **698**, 554 (2004).
- [5] K.K. Seth, Nucl. Phys. B (Proc. Suppl.) **96** 205 (2001).
- [6] Bing-Song Zou, Nucl. Phys. **A644** (1999) 41c.
- [7] C.J. Morningstar and M.J. Peardon, Phys. Rev. D **60** 034509 (1999).
- [8] A. Vacarino and D. Weingarten, Phys. Rev. D **60** 114501 (1999).
- [9] C.E Carlson, T.H. Hanson, and C.Peterson, Phys. Rev. D **27** 1556 (1983).
- [10] N. Isgur and J. Paton, Phys. Rev. D **31** 2910 (1985).
- [11] S. Narison, Nucl. Phys. B **96** 244 (2001).
- [12] M. Melis, F. Murgia and J. Parisi, Phys. Rev. D **70**, 034021 (2004).
- [13] S. J. Brodsky, A. S. Goldhaber and J. Lee, Phys. Rev. Lett. **91**, 112001 (2003).
- [14] D.H. Perkins, “Introduction to High Energy Physics”, 4th Edition, Cambridge University Press, 2000, ISBN 0-521-62196-8.
- [15] D. V. Amelin *et al.* (VES Collaboration), hep-ex/9810013 (1998).
- [16] S. Eidelman *et al.* (Particle Data Group Collaboration), Phys. Lett. B **592**, 1 (2004).
- [17] J.Z. Bai *et al.*, (BES Collaboration), Phys. Rev. Lett. **76** 3502 (1996).
- [18] A. Anastassov *et al.*, (CLEO Collaboration), Phys. Rev. Lett. **82** 286 (1999).
- [19] G. Masek *et al.*, (CLEO Collaboration), Phys. Rev. D **65** 072002 (2002).
- [20] T. Coan, Nucl. Instrum. Meth. A **453**, 49 (2000).

- [21] Y. Kubota *et al.* (CLEO Collaboration), Nucl. Instrum. Meth. A **320**, 66 (1992).
- [22] M. Yurko *et al.* (CLEO Collaboration), Nucl. Phys. Proc. Suppl. **61B**, 212 (1998).
- [23] M. Artuso *et al.* (CLEO Collaboration), Nucl. Instrum. Meth. A **502**, 91 (2003).
- [24] B.K. Heltsley, H. Mahlke-Krueger, CLEO internal note CBX **03-29** (2003) (unpublished).
- [25] GEANT - Detector Description and Simulation Tool, CERN Program Library Long Writeup W5013.
- [26] P. Avery, CLEO internal note CBX **98-37** (1998) (unpublished).
- [27] H. Stöck, J. M Yelton, CLEO internal note CBX **03-17** (2003) (unpublished).
- [28] R. Galik, N. Powell, G. Viehhauser, CLEO internal note CBX **01-50** (2001) (unpublished).
- [29] R. M. Baltrusaitis *et al.* (Mark III Collaboration), Phys. Rev. D **35** 2077 (1987).
- [30] X. Y. Shen *et al.* (BES Collaboration), “ J/ψ Radiative Decays” eConf **C020620**, THAT07 (2002).
- [31] M. Krammer, Phys. Lett. B **74**, 361 (1978).
- [32] J. Z. Bai *et al.* (BES Collaboration), Phys. Rev. D **68**, 052003 (2003)
- [33] J. Z. Bai *et al.* (BES Collaboration), Phys. Rev. Lett. **91**, 022001 (2003).
- [34] C. H. Chang and H. R. Pang, hep-ph/0407188 (2004).
- [35] X. A. Liu, X. Q. Zeng, Y. B. Ding, X. Q. Li, H. Shen and P. N. Shen, hep-ph/0406118 (2004).
- [36] D. V. Bugg, Phys. Lett. B **598**, 8 (2004).
- [37] J. D. Richman, “An Experimenter’s Guide to the Helicity Formalism”, CALT-68-1148 (1995) (unpublished).
- [38] V. Fedeyev, I. Korolkov, D. Besson, R. Galik, H. Paar, CLEO internal note CBX **98-16** (1998) (unpublished).

BIOGRAPHICAL SKETCH

Luis Breva-Newell was born in Boulder, Colorado on December 11, 1975. When he was two years old his family moved to the beautiful Basque Country region of Spain. He graduated High School from GETXO III and attended the Universidad del Pais Basco for four years. He moved to Madrid where he obtained a 5-year degree in Physics from the Universidad Complutense de Madrid. He was accepted to attend graduate School at the University of Florida in 1999.